JOURNAL OF
APPLIED RESEARCH ON SCIENCE AND TECHNOLOGY
INSTITUTE OF RESEARCH AND DEVELOPMENT
RAJAMANGALA UNIVERSITY OF TECHNOLOGY THANYABURI

ISSN Online 2773-9473

Volume 24 Issue 2
May – August 2025

JARST RMUTT

Journal of Applied Research on Science and Technology (JARST)
E-ISSN : 2773-9473
Vol. 24 No. 2 May - August

The Journal of Applied Research on Science and Technology (JARST) aims to disseminate and share knowledge and ideas in the form of high-quality articles to academia, professionals, industrialists, and an important forum for exchanging knowledge between researchers, academics, faculty members and students both national and international, which will bring benefits in building academic cooperation and network that will lead to sustainable use of research. The articles that will be published in this journal must not be ever presented and published or in the evaluation processes in any other journals. Any piracy occurred will be only under the responsibility of the authors. The journal will not be responsible for such consequences.

Aims and Scope

The scope of the journal includes the following areas of research: General Engineering, General Materials Science, General Agricultural and Biological Sciences, General Computer Science, and General Mathematics with particular emphasis on issues that deepen in the basic and applied research. The JARST includes full length original, novel research articles and review articles. Accepted articles are immediately available online and are freely accessible without any restrictions or any other obligations to researchers and scholarly people globally.

Review Process

1. Evaluation by the Editor-in-Chief

The Editor-in-Chief will see whether the topic and theme of the article are appropriate and congruent with the stipulated objectives and format of the Journal. Plagiarism and benefits relating to theory and business contribution will also be investigated. The submitted paper may be returned to the author for preliminary revising or, if the aforesaid criteria are not met, rejected.

2. Evaluation by Review

All submitted manuscripts must be reviewed by at least two expert reviewers in the related fields. Reviewers will evaluate the quality of submitted article for publication via the double-blinded review system.

3. Evaluates the Reviews

The Editor-in-Chief make decision for article publication based on the external readers' evaluation. The said decision is either accepting the article for publication, rejecting it, or resending it back to the author for further elaborating revision.

Period of Issued Journal

The Journal of Applied Research on Science and Technology (JARST) will be 3 issues/year, as follows:

1st issue: January - April
2nd issue: May - August
3rd issue: September - December

Advisory Board

Contact

Institute of Research and Development, Rajamangala University of Technology Thanyaburi (RMUTT)
39 Moo 1, Klong 6, Khlong Luang Pathum Thani 12110 Thailand
Website: https://ph01.tci-thaijo.org/index.php/rmutt-journal/index
Phone: +66 2 5494492, +66 2 5494681
Fax: +66 2 5494680
Email: jarst@rmutt.ac.th

Editorial Note

The Journal of Applied Research on Science and Technology (JARST) is an academic journal prepared by Institute of Research and Development, Rajamangala University of Technology Thanyaburi (RMUTT). The JARST aims to disseminate and share knowledge and ideas in the form of high-quality articles related General Engineering, General Materials Science, General Agricultural and Biological Sciences, General Computer Science, and General Mathematics to researchers, academics, faculty members and students both national and international.

This journal published eight research articles. Each of the research articles presented interesting concepts such as, On the generalization neo balancing sequence and some applications, Evaluations of the mechanical and physical properties of galangal root-poly(butylene-succinate) (PBS)-based biocomposite, Laser-assisted FTO/WO_3/$BiVO_4$ photoanode fabrication for enhanced photoelectrocatalytic performance and durability for organic dye degradation, A predictive model for highly efficient helicopter maintenance in the Royal Thai Air Force using deep learning, Fabrication of uric acid chemical sensor based on tricobalt tetroxide crosslinked chitosan with gold nanoparticle modified glassy carbon electrode, Analysis of road settlement on soft soil using 3D finite element method: A case study of the Amata Smart City construction project, Chonburi phase 2, Electrospun PLA/PBS/MWCNT nanocomposite fibers for high-performance air filtration: A sustainable approach and Prototype inspection cart for detecting track geometry irregularities Therefore, this journal is a channel disseminating the knowledge areas of physical sciences and life sciences which related persons could apply it for further benefits.

Lastly, the editorial team would like to considerably thank you for supporting and pushing forward this journal to occur and well accomplish. We are hopeful of your good cooperation and continuing support in the future.

Editorial Team

Contents

Research Articles	Page
On the generalization neo balancing sequence and some applications *Natdanai Chailangka and Apisit Pakapongpun*	**257946**
Evaluations of the mechanical and physical properties of galangal root-poly(butylene-succinate) (PBS)-based biocomposite *Naiyawat Sukthang, Piyamart Jannok, Weerakul Meaklangsang, Plengpin Pienphumpong, Nartchanok Prangpru, Ruthairat Laiking, Sirikanlaya Temkrasem, Jittiwat Nithikarnjanatharn, Khongdet Phasinam and Jantana Suntudprom*	**257771**
Laser-assisted FTO/WO_3/$BiVO_4$ photoanode fabrication for enhanced photoelectrocatalytic performance and durability for organic dye degradation *Chatchai Ponchio and Watcharapong Nareejun*	**260565**
A predictive model for highly efficient helicopter maintenance in the Royal Thai Air force using deep learning *Somkait Hoonsakul, Prasong Praneetpolgrang and Payap Sirinam*	**260451**
Fabrication of uric acid chemical sensor based on tricobalt tetroxide crosslinked chitosan with gold nanoparticle modified glassy carbon electrode *Nuenghathai Chaiya, Suphaporn Chenkhuruthum, Ratchadaporn Puntharod, Anchana Preechaworapun, Pusit Pookmanee and Tanin Tangkuaram*	**260199**
Analysis of road settlement on soft soil using 3D finite element method: A case study of the Amata Smart City construction project, Chonburi phase 2 *Prachaya Thanakitthada, Attapole Malai and Kongpop Watcharasawe*	**260742**
Electrospun PLA/PBS/MWCNT nanocomposite fibers for high-performance air filtration: A sustainable approach *Manisara Phiriyawirut, Prin Wangtanapat, Apiwit Chanthanchumpunon and Ratchanon Phanchaweng*	**261054**
Prototype inspection cart for detecting track geometry irregularities *Apisit Muanmuang, Pipat Pramot, Terdkiat Limpeteeprakarn and Manusak Janthong*	**260837**

Received: September 5, 2024 | Revised: January 23, 2025 | Accepted: January 27, 2025

JOURNAL OF APPLIED RESEARCH ON SCIENCE AND TECHNOLOGY
JARST
INSTITUTE OF RESEARCH AND DEVELOPMENT
RAJAMANGALA UNIVERSITY OF TECHNOLOGY THANYABURI
ISSN ONLINE: 2773-9473
https://ph01.tci-thaijo.org/index.php/rmutt-journal

On the generalization neo balancing sequence and some applications

Natdanai Chailangka and Apisit Pakapongpun*
Department of Mathematics, Faculty of Science, Burapha University, Chonburi 20130, THAILAND
*Corresponding author: apisit.buu@gmail.com

ABSTRACT

We investigate the generalization of sequence neo balancing numbers and their recurrence relations by extending the catalyst of certain sequences in balancing numbers to any integer k in the sequence neo balancing numbers. We derive the Diophantine equation for sequence neo balancing numbers in terms of k, which corresponds to the Diophantine equation for neo balancing numbers. We derive the Diophantine equation for the sequence neo balancing numbers and solve it via Pell's equation and Brahmagupta's identity. We examine the square root term in the derived Diophantine equation for the sequence neo balancing numbers by treating it as the generalized Pell's equation. Simultaneously, we consider the well-known Pell's equation. We integrate the generalized Pell's equation for the sequence neo balancing numbers to the well-known Pell's equation by using the Brahmagupta's identity. We obtain two solutions for both the generalized Pell's equation for the sequence neo balancing numbers and the well-known Pell's equation. The obtained solutions are sometimes analogous for some values of k. Then we investigate more precisely each case and substitute the solutions into the derived Diophantine equation for the sequence neo balancing numbers. Therefore, there are values of k that make both solutions analogous implying the recurrence relation can give all terms in the sequence neo balancing numbers. Simultaneously, there are values of k that make both solutions different implying that we need two recurrence relations generated by the two solutions to complete the sequence neo balancing numbers. Moreover, we establish a few theorems to explain why some values of k generate similar sequence of neo balancing numbers.

Keywords: Balancing numbers, Neo balancing numbers, Sequence neo balancing numbers, Pell's equation, Brahmagupta's identity

INTRODUCTION

In the field of number theory, sequences play a fascinating role in unraveling hidden patterns and relationships among integers. The study of balancing numbers has emerged as a significant area of interest within number theory, offering valuable insights and applications to researchers. Over the past two decades, extensive investigations into balancing numbers have enriched the field, highlighting their mathematical elegance and intricate properties.

Balancing numbers, characterized by their unique relationship to sums of consecutive integers, have been explored in various contexts, including their connections to Pell's equations, recurrence relations, and integer sequences. This body of work has not only deepened the theoretical understanding of these numbers but has also uncovered potential applications in areas such as cryptography and algebraic structures [1-8].

The sustained scholarly focus on balancing numbers underscores their importance as a rich and fruitful subject of mathematical inquiry. In 1999, Panda and Behera [9] laid the foundation for an intriguing exploration with the introduction of the founding important results on the square roots of triangular numbers as balancing numbers. A positive integer n is called a balancing number if it satisfies the Diophantine equation [10]

$$1+2+3+\cdots+(n-1)=(n+1)+(n+2)+\cdots+(n+r) \quad (1.1)$$

for some positive integer r. Here r is called the balancer corresponding to the balancing number n. Then, Panda and Ray [4] discovered generalization balancing numbers to cobalancing numbers. A positive integer n is defined as a cobalancing number if n is a solution of Diophantine equation

$$1+2+3+\cdots+n=(n+1)+(n+2)+(n+3)+\cdots+(n+r) \quad (1.2)$$

for some positive integer r. Here r is called the cobalancer corresponding to the cobalancing number n. Later, Panda [11] found the many results on the sequence of balancing numbers, the sequence of the cobalancing numbers and also connected to Fibonacci numbers. These pioneering works have served as a catalyst for further investigation and have paved the way for new inquiries to neo balancing numbers.

DOI: 10.60101/jarst.2024.257946

JOURNAL OF APPLIED RESEARCH ON SCIENCE AND TECHNOLOGY

Chailangka and Pakapongpun [12] defined neo balancing numbers by the study of Diophantine equation

$$1+2+3+\cdots+(n-1) = (n-1)+n+(n+1)+\cdots+(n+r), \quad (1.3)$$

for each positive integer n which is called a neo balancing number and for some integer r which is called a neo balancer corresponding to the neo balancing number n.

MATERIALS AND METHODS

Pell's equation

The Diophantine equation of the form

$$x^2 - ny^2 = 1, \quad (1.4)$$

where n is a given positive nonsquare integer, seeks integer solutions sought for x and y [13].

Generalized Pell's equation

The Diophantine equation of the form

$$x^2 - ny^2 = k, \quad (1.5)$$

where n is a given positive nonsquare integer, k is a non zero integer and integer solutions are sought for x and y [13].

Additional solutions from the fundamental solution

If (x_1, y_1) is a fundamental solution, then the algebraic form is

$$x_k + y_k\sqrt{n} = (x_1 + y_1\sqrt{n})^k \quad (1.6)$$

and also yields the recurrence relations

$$x_{k+1} = x_1x_k + ny_1y_k \quad (1.7)$$

$$y_{k+1} = x_1y_k + y_1x_k, \quad (1.8)$$

where n is a given positive non-square integer and k is a positive integer [14].

Brahmagupta's identity

If the triples (x_1, y_1, k_1) and (x_2, y_2, k_2) are solutions of Diophantine equation

$$x^2 - ny^2 = k, \quad (1.9)$$

then we can compose the triples to generate new triples

$$(x_1x_2 + ny_1y_2, x_1y_2 + x_2y_1, k_1k_2) \text{ and}$$
$$(x_1x_2 - ny_1y_2, x_1y_2 - x_2y_1, k_1k_2),$$

where n is a given positive non-square integer, k is a non zero integer and integer solutions are sought for x and y [15].

RESULTS AND DISCUSSION

1. Sequence neo balancing numbers

In this section, we will introduce neo balancing numbers in the sequence a_m. Let $\{a_m\}_{m=1}^{\infty}$ be a sequence of real numbers. Then a_m is called a sequence neo balancing number if a_m satisfies the Diophantine equation

$$a_1 + a_2 + a_3 + \cdots + a_{m-1} = a_{m-1} + a_m + a_{m+1} + \cdots + a_{m+r} \quad (2.1)$$

for some integer r, simultaneous m_n is called a sequence neo balancing number's index and r_n is called the sequence neo balancer's index which corresponding to m_n. Then we will get sequences for neo balancing numbers by equation (2.1) in the following sections.

2. Generalized neo balancing numbers

In this section, we will generalize the idea of sequence for neo balancing numbers by equation (2.1). For any integer k in the sequence $a_m = 2m + k$, we derive the sequence neo balancing number $2m + k$ as a Diophantine equation (2.1). Currently, we substitute $a_m = 2m + k$ and obtain the equation

$$(2+k)+(4+k)+(6+k)+\cdots+(2m-2+k) = (2m-2+k)+(2m+k)+(2m+2+k) +\cdots+(2m+2r+k). \quad (2.2)$$

From equation (2.2), we derive to

$$2m = 2r+5-k+\sqrt{8r^2+24r+k^2+2k+17}, \quad (2.3)$$

for any integer k. Henceforth we will consider k. If k is odd, then $k^2+2k+17$ can be divided by 4 and we can derive equation (2.3) as the following.

$$m = r + \frac{5-k}{2} + \frac{1}{2}\sqrt{8r^2+24r+k^2+2k+17}.$$

Similarly, if k is even, then we can derive equation (2.3) as

$$m = \frac{2r-k}{2} + \frac{1}{2}(5+\sqrt{8r^2+24r+k^2+2k+17}).$$

In the present, we will consider $x^2 - 2y^2 = D$ which we can compose the solution to the fundamental of Pell's equation by Brahmagupta's identity, see [14-17]. Then we will obtain the expanded solutions to $x^2 - 2y^2 = D$. Since m is a neo balancing number,

$$y = \sqrt{8r^2+24r+k^2+2k+17}$$

must be an integer. Hence, we set

$$y = \sqrt{8r^2+24r+k^2+2k+17}$$

Then there exists $x = 4r+6$ such that

$$x^2 - 2y^2 = -2k^2 - 4k + 2. \quad (2.4)$$

Currently, we let $D = -2k^2 - 4k + 2$ and rewrite D as $D = 4 - 2(k+1)^2$, which implies that $(2, |k+1|)$ is a solution for the equation (2.4). Then the next process will be helped by the quite well-known Pell's equation and the fascinating Brahmagupta's identity. We consider Pell's equation

DOI: 10.60101/jarst.2024.257946

JOURNAL OF APPLIED RESEARCH ON SCIENCE AND TECHNOLOGY

$$x^2 - 2y^2 = 1, \quad (2.5)$$

with a fundamental solution $(3,2)$. Since the Pell's equation (2.5) is investigated for many years, it is easy to find the other solution by relations

$$\bar{x}_n = \frac{\alpha^n + \beta^n}{2}$$

$$\bar{y}_n = \frac{\alpha^n + \beta^n}{2\sqrt{2}},$$

where $\alpha = 3 + 2\sqrt{2}$ and $\beta = 3 - 2\sqrt{2}$. Therefore, $(2, |k+1|)$ is a solution for the equation (2.4) and $(\bar{x}_n, \bar{y}_n)$ is also a solution for the equation (2.5). Then we use Brahmagupta's identity to combine equation (2.4) and equation (2.5) and their solutions. Thus, we obtain the combined solution as relations

$$X_n = 2\bar{x}_n + 2|k+1|\bar{y}_n$$

$$Y_n = |k+1|\bar{x}_n + 2\bar{y}_n$$

and

$$X_n^* = 2\bar{x}_n - 2|k+1|\bar{y}_n$$

$$Y_n^* = |k+1|\bar{x}_n - 2\bar{y}_n.$$

Therefore, (X_n, Y_n) and (X_n^*, Y_n^*) are solutions to equation (2.4). Moreover, we find that the recurrence relation for both two sequences of X_n, Y_n and X_n^*, Y_n^* as given satisfy the recurrence

$$X_n = 6X_{n-1} - X_{n-2} \quad (2.6)$$

$$Y_n = 6Y_{n-1} - Y_{n-2} \quad (2.7)$$

and

$$X_n^* = 6X_{n-1}^* - X_{n-2}^* \quad (2.8)$$

$$Y_n^* = 6Y_{n-1}^* - Y_{n-2}^* \quad (2.9)$$

Since equation (2.6), (2.7), (2.8) and equation (2.9), we get

$$2X_n = \alpha^n(2+|k+1|\sqrt{2}) + \beta^n(2-|k+1|\sqrt{2})$$

$$2\sqrt{2}Y_n = \alpha^n(2+|k+1|\sqrt{2}) - \beta^n(2-|k+1|\sqrt{2})$$

and

$$2X_n^* = \alpha^n(|k+1|\sqrt{2}-2) - \beta^n(|k+1|\sqrt{2}+2)$$

$$2\sqrt{2}Y_n^* = \alpha^n(|k+1|\sqrt{2}-2) + \beta^n(|k+1|\sqrt{2}+2).$$

Therefore, we obtain two sequences both X_n, Y_n and X_n^*, Y_n^* which make the sets of solution of the equation (2.4) are sometimes analogous. Then we have to consider this critical property $X_n = |X_{n+n_0}^*|$ and $Y_n = |Y_{n+n_0}^*|$. Since $X_n = |X_{n+n_0}^*|$, we will obtain

$$\left(\beta^{n_0}(2+|k+1|\sqrt{2})\right)^2 = (2-|k+1|\sqrt{2})^2.$$

Then we have

$$\left(\beta^{n_0}(2+|k+1|\sqrt{2})\right) - (2-|k+1|\sqrt{2}) = 0$$

and

$$\left(\beta^{n_0}(2+|k+1|\sqrt{2})\right) + (2-|k+1|\sqrt{2}) = 0.$$

Since $\beta^{n_0} = (3-2\sqrt{2})^{n_0}$ can be calculated algebraically form $x_{n_0} + y_{n_0}\sqrt{2} = (3+2\sqrt{2})^{n_0}$ [9] when $x_0 = 1$, $y_0 = 0$, $x_1 = 3$, $y_1 = 2$ and the above discussion, we have important 4 cases as the following.

1. $|k+1| = \dfrac{x_{n_0} - 1}{y_{n_0}}$
2. $|k+1| = \dfrac{2y_{n_0}}{x_{n_0} + 1}$
3. $|k+1| = \dfrac{x_{n_0} + 1}{y_{n_0}}$
4. $|k+1| = \dfrac{2y_{n_0}}{x_{n_0} - 1}$.

Theorem 2.1 Let $A = \{-3, -2, -1, 0, 1\}$. For any integer $k \in A$, the recurrence relations for the sequence neo balancing number $a_m = 2m + k$ is

$$a_{m_n} = 6a_{m_{n-1}} - a_{m_{n-2}} - 8$$

and the recurrence relations for the sequence neo balancing number's index is $m_n = 6m_{n-1} - m_{n-2} + 2k - 4$, where $n \geq 3$.

Proof.

Consider 4 given cases. If we do not shift any index, then $n_0 = 0$. We obtain that

$$|k+1| = 0$$

by case 1 and 2. Hence, $k = -1$. Therefore, $X_n = |X_n^*|$ meanwhile X_n and X_n^* have same set of solution of equation (2.4) when $a_m = 2m - 1$. Similarly, $Y_n = |Y_n^*|$ meanwhile Y_n and Y_n^* have same set of solution of equation (2.4) when $a_m = 2m - 1$. Subsequently, if we shift an index 1 step for $X_n = |X_{n+n_0}^*|$, then $n_0 = 1$. Hence, we obtain that $|k+1| = 1$ by case 1 and case 2 meanwhile we obtain that $|k+1| = 2$ by case 3 and case 4. Then we have $k = 0, -2, -3$ and 1, respectively. Therefore, $X_n = |X_{n+1}^*|$ meanwhile X_n and X_{n+1}^* have same set of solution of equation (2.4) when $a_m = 2m, a_m = 2m-2, a_m = 2m-3$ and $a_m = 2m+1$. Since we have already discovered $2m = 2r + 5 - k + \sqrt{8r^2 + 24r + k^2 + 2k + 17}$, $y = \sqrt{8r^2 + 24r + k^2 + 2k + 17}$ and $x = 4r + 6$, we

DOI: 10.60101/jarst.2024.257946

JOURNAL OF APPLIED RESEARCH ON SCIENCE AND TECHNOLOGY

will combine them. Hence, we get the recurrence relation for sequence neo balancing number's index $m_n = 6m_{n-1} - m_{n-2} + 2k - 4$. Since $a_m = 2m + k$, we will get fascinating results on the generalized recurrence relation for the sequence neo balancing number as $a_{m_n} = 6a_{m_{n-1}} - a_{m_{n-2}} - 8$.

Theorem 2.2 Let $A = \{-3, -2, -1, 0, 1\}$. For any integer $k \in A^c$, the recurrence relations for the sequence neo balancing number $a_m = 2m + k$ are

$$a_{m_{2n-1}} = 6a_{m_{2n-3}} - a_{m_{2n-5}} - 8$$

and

$$a_{m_{2n}} = 6a_{m_{2n-2}} - a_{m_{2n-4}} - 8.$$

Moreover, the recurrence relations for the sequence neo balancing number's index are

$$m_{2n-1} = 6m_{2n-3} - m_{2n-5} + 2k - 4$$

and

$$m_{2n} = 6m_{2n-2} - m_{2n-4} + 2k - 4,$$

respectively, where $n \geq 3$.

Proof.

Since (x_{n_0}, y_{n_0}) satisfies the algebraic form recurrence relation

$$x_{k+1} = 3x_k + 4y_k$$

$$y_{k+1} = 3y_k + 2x_k,$$

we rewrite the 4 given cases as

1. $|k+1| = 1 + \dfrac{x_{n_0-1} + y_{n_0-1} - 1}{2x_{n_0-1} + 3y_{n_0-1}}$
2. $|k+1| = 1 + \dfrac{x_{n_0-1} + 2y_{n_0-1} - 1}{3x_{n_0-1} + 4y_{n_0-1} + 1}$
3. $|k+1| = 1 + \dfrac{x_{n_0-1} + y_{n_0-1} + 1}{2x_{n_0-1} + 3y_{n_0-1}}$
4. $|k+1| = 1 + \dfrac{x_{n_0-1} + 2y_{n_0-1} + 1}{3x_{n_0-1} + 4y_{n_0-1} - 1}$.

Obviously, $|k+1|$ of the 4 above cases are not integer for $n_0 > 1$. Therefore, X_n and $X^*_{n+n_0}$ do not have same set of solution to equation (2.4) where $n_0 > 1$. Similarly, we can obtain the important property as the above for $Y_n = |Y^*_{n+n_0}|$. Then we will obtain 2 sets of solutions to equation (2.4) which generated by (X_n, Y_n) and (X^*_n, Y^*_n).

Since we have already discovered $2m = 2r + 5 - k + \sqrt{8r^2 + 24r + k^2 + 2k + 17}$, $y = \sqrt{8r^2 + 24r + k^2 + 2k + 17}$ and $x = 4r + 6$, we will combine them. Hence, we get the recurrence relation for sequence neo balancing number's index $m_{2n-1} = 6m_{2n-3} - m_{2n-5} + 2k - 4$ and $m_{2n} = 6m_{2n-2} - m_{2n-4} + 2k - 4$.

Since $a_m = 2m + k$, we will get fascinating results on the generalized recurrence relation for the sequence neo balancing number as $a_{m_{2n-1}} = 6a_{m_{2n-3}} - a_{m_{2n-5}} - 8$ and $a_{m_{2n}} = 6a_{m_{2n-2}} - a_{m_{2n-4}} - 8$.

Theorem 2.3 Let $f : \square \to \square$ be a function that $f(k) = 4 - 2(k+1)^2$. If there are k_1 and k_2 such that $k_1 \neq k_2$, then the sequences $a_m = 2m + k_1$ and $a_m = 2m + k_2$ have the same sequence neo balancing number if and only if $f(k_1) = f(k_2)$.

Proof.

Since we have defined $D = 2 - (2k^2 + 4k)$, we can rewrite it to a parabola equation

$$D - 4 = -2(k+1)^2.$$

Then we will obtain the solution (k_1, D) and (k_2, D) where $k_1 \neq k_2$ which imply the same equation as equation (2.4). Simultaneously, we will get the same sequence neo balancing number by k_1 and k_2 if $f(k_1) = f(k_2)$.

3. Sequence neo balancing numbers in some sequences

In this section, we will demonstrate sequence neo balancing numbers in some sequences.

Example 3.1 The sequence neo balancing numbers in sequence $a_m = 2m - 1$.

By theorem 2.1, we let $k = -1$. Then the recurrence relations for the sequence neo balancing number $a_m = 2m - 1$ are $m_n = 6m_{n-1} - m_{n-2} - 6$ and $a_{m_n} = 6a_{m_{n-1}} - a_{m_{n-2}} - 8$. Then 2, 5, 22, 121, 698 and 4061 are first six examples of the sequence neo balancing number's indices meanwhile $-1, 0, 7, 48, 287$ and 1680 are first six examples of the sequence neo balancer's indices, where $a_m = 2m - 1$. We can demonstrate by putting a_m to the equation (2.1) as the following.

If $m = 22$ and $r = 7$, then we obtain

$$\begin{aligned} a_1 + a_2 + a_3 + \cdots + a_{22-1} &= a_{22-1} + a_{22} + a_{23} + \cdots + a_{22+7} \\ 1 + 3 + 5 + \cdots + 41 &= 41 + 43 + 45 + \cdots + 57 \\ 441 &= 441. \end{aligned}$$

DOI: 10.60101/jarst.2024.257946

JOURNAL OF APPLIED RESEARCH ON SCIENCE AND TECHNOLOGY

Hence, 3, 9, 43, 241, 1396 and 8121 are the first six example of sequence neo balancing numbers, where $a_m = 2m-1$.

Remark 3.2 If we substitute $k=-1$, then the another k in theorem 2.3 which generate same sequence do not exist cause $k=-1$ is a vertex of the parabola $D-4=-2(k+1)^2$.

Example 3.3 The sequence neo balancing numbers in sequence $a_m = 2m-2$ and $a_m = 2m$.

By theorem 2.1 and theorem 2.3, we can choose $k=-2$ or $k=0$, so let $k=0$. Then the recurrence relations for the sequence neo balancing number $a_m = 2m$ are $m_n = 6m_{n-1} - m_{n-2} - 4$ and $a_{m_n} = 6a_{m_{n-1}} - a_{m_{n-2}} - 8$. Then 2, 7, 36, 205, 1190 and 6931 are first six examples of the sequence neo balancing number's indices(neo balancing numbers) meanwhile $-1, 1, 13, 83, 491$ and 2869 (neo balancer) are first six examples of the sequence neo balancer's indices, where $a_m = 2m$. We can demonstrate by putting $a_m = 2m$ to the equation (2.1) as the following. If $m=36$ and $r=13$, then we obtain

$$\begin{aligned} a_1 + a_2 + \cdots + a_{36-1} &= a_{36-1} + a_{36} + \cdots + a_{36+13} \\ 2+4+\cdots+70 &= 70+72+\cdots+98 \\ 1260 &= 1260. \end{aligned}$$

Hence, 4, 14, 72, 410, 2380 and 13862 are first six example of sequence neo balancing numbers (The twice of neo balancing numbers), where $a_m = 2m$.

Remark 3.4 The sequences $a_m = 2m-2$ and $a_m = 2m$ on sequence neo balancing numbers are twice of neo balancing numbers.

Example 3.5 The sequence neo balancing numbers in sequences $a_m = 2m+1$ and $a_m = 2m-3$.

By theorem 2.1 and theorem 2.3, we can choose $k=1$ or $k=-3$, so let $k=1$. Then the recurrence relations for the sequence neo balancing number $a_m = 2m+1$ are $m_n = 6m_{n-1} - m_{n-2} - 2$ and $a_{m_n} = 6a_{m_{n-1}} - a_{m_{n-2}} - 8$. Then 2, 9, 50, 289, 1682 and 9801 are first six examples of the sequence neo balancing number's indices and $-1, 2, 19, 118, 695$ and 4058 are first six examples of the sequence neo balancer's indices, where $a_m = 2m+1$. We can demonstrate by putting $a_m = 2m+1$ to the equation (2.1) as the following. If $m=50$ and $r=19$, then we obtain

$$\begin{aligned} a_1 + a_2 + \cdots + a_{50-1} &= a_{50-1} + a_{50} + \cdots + a_{50+19} \\ 3+5+\cdots+99 &= 99+101+\cdots+139 \\ 2499 &= 2499. \end{aligned}$$

Hence, 5, 19, 101, 579, 3365 and 19603 are first six example of sequence neo balancing numbers, where $a_m = 2m+1$.

Example 3.6 The sequence neo balancing numbers in sequences $a_m = 2m+3$ and $a_m = 2m-5$.

By theorem 2.2 and theorem 2.3, we can choose $k=3$ or $k=-5$, so let $k=3$. Then the recurrence relations for the sequence neo balancing number $a_m = 2m+3$ are $m_{2n-1} = 6m_{2n-3} - m_{2n-5} + 2$ and $a_{m_{2n-1}} = 6a_{m_{2n-3}} - a_{m_{2n-5}} - 8$ and another one sequence $m_{2n} = 6m_{2n-2} - m_{2n-4} + 2$ and $a_{m_{2n}} = 6a_{m_{2n-2}} - a_{m_{2n-4}} - 8$ where $n \geq 3$. Then 2, 6, 13, 37, 78, 218, 457, 1273, 2666 and 7422 are first ten examples of sequence neo balancing number's indices and $-1, 1, 4, 14, 31, 89, 188, 526, 1103$ and 3073 are first ten examples of sequence neo balancer's indices, where $a_m = 2m+3$. We can demonstrate by putting $a_m = 2m+3$ to the equation (2.1) as the following. If $m=37$, then we obtain $r=14$ and

$$\begin{aligned} a_1 + a_2 + \cdots + a_{37-1} &= a_{37-1} + a_{37} + \cdots + a_{37+14} \\ 5+7+\cdots+75 &= 75+77+\cdots+105 \\ 1440 &= 1440. \end{aligned}$$

Hence, 7, 15, 29, 77, 159, 439, 917, 2549, 5335 and 14847 are first ten example of sequence neo balancing numbers, where $a_m = 2m+3$. Similarly, we let $k=-5$. Then 1, 2, 6, 10, 17, 41, 82, 222, 461 and 1277 are first ten examples of sequence neo balancing number's indices simultaneously -3, -1, 7, 15, 29, 77, 159, 439, 917 and 2549 are first ten example of sequence neo balancing numbers, where $a_m = 2m-5$.

Discussion

In this study, we explored sequence neo balancing numbers and extended the concept from sequence balancing numbers, as published by Panda [4]. The study of sequence balancing numbers involves specific sequences, such as $a_m = 2m-1$ in [4], but we established the sequence $a_m = 2m+k$ for sequence neo balancing numbers where k is any integer. Additionally, we derived their recurrence relations and found that our findings reveal the

DOI: 10.60101/jarst.2024.257946

significant role of combining the generalized Pell's equation and Brahmagupta's identity in deriving solutions. Specifically, we successfully obtained two sequences that demonstrate analogous behavior under specific conditions. An interesting result emerged from analyzing the indices, showing that certain sequences share similar solutions under particular constraints. This similarity highlights the structured nature of sequence neo balancing numbers and opens up possibilities for further algebraic exploration. Furthermore, we established that for any integer k, the sequence of neo balancing numbers is always accompanied by equivalent sequences, affirming the robustness of the generalization. These findings provide a foundation for future investigations into more complex relationships among generalized sequences.

Further work could explore connections between these sequences and other classical number theory problems or identify practical applications in computational mathematics and cryptography.

CONCLUSIONS

We have investigated the generalization of sequence of neo balancing numbers and their recurrence relations by extending the catalyst that the certain sequence $a_m = 2m \pm 1$ in sequence balancing number to any integer k in sequence neo balancing number. We have solved the equation by composing equations (2.4) and Pell's equation via Brahmagupta's identity. Hence, we have obtained two sequence solutions (X_n, Y_n) and (X_n^*, Y_n^*). Subsequently, we have known that the 2 given solutions are sometimes analogous. Then we have delved into each index. We have found that there exist $k = -3, -2, -1, 0, 1$ which can force (X_n, Y_n) similar to (X_n^*, Y_n^*). Then the sequence $a_m = 2m + k$ which is generated by (X_n, Y_n) and (X_n^*, Y_n^*) are analogous. Alternatively, if $k \neq -3, -2, -1, 0, 1$, there are 2 sequences $a_m = 2m + k$ for sequence neo balancing number which is generated by (X_n, Y_n) and (X_n^*, Y_n^*) such that each sequence individually satisfy the recurrence relations. Furthermore, for all integer $k \neq -1$, the sequence $a_m = 2m + k$ for sequence neo balancing number always has another equivalent sequence.

ACKNOWLEDGEMENT

This work is supported by Faculty of Science, Burapha University, Thailand.

REFERENCES

1. Patra A, Panda GK. Positive integer solutions of some diophantine equations involving Lucas-balancing numbers. The Fibonacci Quarterly. 2020;58(1):3-17.
2. Kuloğlu B, Özkan E, Shannon A. p-Analogue of biperiodic Pell and Pell–Lucas polynomials. Notes on Number Theory and Discrete Mathematics. 2023;29(2):336-47.
3. Soykan Y. A study on generalized balancing numbers. Asian Journal of Advanced Research and Reports. 2021;15(5):78-100.
4. Panda GK, Ray PK. Cobalancing numbers and cobalancers. International Journal of Mathematics and Mathematical Sciences. 2005;2005(8):1189-2000.
5. Bhoi PK, Rout SS, Panda GK. On perfect powers that are sum of two balancing numbers. Period Math Hung. 2024;88(1):93-101.
6. Kuloğlu B, Özkan E, Shannon AG. Incomplete generalized Vieta-Pell and Vieta-Pell-Lucas polynomials. Notes on Number Theory and Discrete Mathematics. 2021;27(4):245-56.
7. Ozkan EN, Akkus H. On K-Chebsyhev Sequence. WSEAS Transactions on Mathematics. 2023;22.
8. Özkan E, Uysal M, Godase AD. Hyperbolic k-Jacobsthal and k-Jacobsthal-Lucas quaternions. Indian Journal of Pure and Applied Mathematics. 2022;53(4):956-67.
9. Behera A, Panda GK. On the square roots of triangular numbers. Fibonacci Quart. 1999;37:98-105.
10. Heath TL. Diophantus of Alexandria: A study in the history of Greek algebra. University Press; 1910.
11. Panda GK. Sequence balancing and cobalancing numbers. Fibonacci Quart. 2007;45(3):265-71.
12. Chailangka N, Pakapongpun A. Neo balancing numbers. International Journal of Mathematics and Computer Science. 2021;16(4):1653-64.
13. Andrica D, Andreescu T. Number theory: structures, examples, and problems. Birkhäuser Boston: 2009.
14. Rosen KH. Elementary number theory. London: Pearson Education; 2011.
15. Dutta AK. Mathematics in ancient India. Resonance. 2003;8(11):10-24.
16. Jacobson MJ, Williams HC. Solving the Pell equation. New York: Springer; 2009.
17. Uysal M, Özkan E. Balancing and Lucas-Balancing hybrid numbers and some identities. Journal of Information and Optimization Sciences. 2024;45(5):1293-304.

DOI: 10.60101/jarst.2024.257946

Received: August 6, 2024 | Revised: February 11, 2025 | Accepted: February 13, 2025

JOURNAL OF APPLIED RESEARCH ON SCIENCE AND TECHNOLOGY
JARST
INSTITUTE OF RESEARCH AND DEVELOPMENT
RAJAMANGALA UNIVERSITY OF TECHNOLOGY THANYABURI
ISSN ONLINE: 2773-9473
https://ph01.tci-thaijo.org/index.php/rmutt-journal

Evaluations of the mechanical and physical properties of galangal root-poly(butylene-succinate) (PBS)-based biocomposite

Naiyawat Sukthang[1], Piyamart Jannok[1], Weerakul Meaklangsang[1], Plengpin Pienphumpong[1], Nartchanok Prangpru[1], Ruthairat Laiking[2], Sirikanlaya Temkrasem[2], Jittiwat Nithikarnjanatharn[3], Khongdet Phasinam[4], and Jantana Suntudprom[1*]

[1]Department of Food and Postharvest Innovation Engineering, Faculty of Engineering and Technology, Rajamangala University of Technology Isan, Nakhon Ratchasima Province, 30000, THAILAND
[2]Department of Administration, Faculty of Engineering and Technology, Rajamangala University of Technology Isan, Nakhon Ratchasima province, 30000, THAILAND
[3]Department of Industrial Engineering, Faculty of Engineering and Technology, Rajamangala University of Technology Isan, Nakhon Ratchasima Province, 30000, THAILAND
[4]Department of Industrial Engineering, Faculty of Food and Agricultural Technology, Pibulsongkram Rajabhat University, Phitsanulok Province, 65000, THAILAND
[*]Corresponding author: xanta_na@yahoo.com

ABSTRACT

Various agricultural waste materials, such as cassava stems, pineapple leaves, banana peels, and corn pulp, were developed into natural biodegradable packaging, adding value to the agricultural waste. Hence, this research aimed to develop the biocomposites and inspect their mechanical and physical properties. Fresh galangal root waste was washed and dried at 80°C for 12 hours and then ground to achieve a particle size of 250 microns (GR250) and 400 microns (GR400). Then, they were mixed with PBS at the ratio of PBS: GR250 at 80:20 wt.%. Later, the mixtures were passed through the extruder, and the plastic strands were obtained. Later, these plastic strands were shredded into small pellets called biocomposite pellets. These pellets were formed by heat at 150°C for 5 minutes under a pressure of 10 MPa to obtain the biocomposite specimens. Then, they were assessed the mechanical properties (tensile strength, impact strength, and flexural strength). Also, the physical properties (water absorption, density, morphology, and percentage of natural degradation) were performed. The results could imply that adding GR250 and GR400 into PBS-based biocomposite could cause reductions in structural integrity and elasticity. PBS/GR biocomposites would assert less impact force. The results could reflect that PBS/GR250 and PBS/GR400 biocomposites had more ability to resist bending stresses than neat PBS. PBS/GR400 biocomposites tended to degrade faster, as supported by microstructure observation and lower density compared to PBS/GR250. It could be concluded that the galangal root waste could be added value by developing into a based-biocomposite. Galangal root waste can produce biocomposite food containers that can resist bending stresses. Biocomposite food containers have a natural biodegradable property and environmentally friendly aspects.

Keywords: Biocomposite, Value-added, Galangal root, PBS, Agricultural waste

INTRODUCTION

Plastic has outstanding properties, such as being cheap, lightweight, strong, and durable. These properties make plastic popular, and its usage continuously increases in various aspects. The production of plastic has a low production cost. In addition, modern technology can produce plastic with various properties according to needs. In terms of the environment, the increasing use of plastic has led to increased plastic waste. According to the Ministry of Natural Resources and Environment's report, there were up to 2.76 million tons of plastic waste [1]. Because plastic has properties that are difficult to decompose and deteriorate, plastic waste remains in the environment for a long time. This plastic waste causes a significant burden in management and disposal. This inevitably results in environmental problems.

Plastic could also contaminate food and be harmful to human health. Plastic creates toxic smoke in the air and carbon dioxide gas when burnt which causes global boiling. Many international organizations, such as the Food and Agriculture Organization of the United Nations, have launched a campaign to reduce the amount of food damage and ultimately reduce the amount of waste employing reduction of the overall environmental impact [2].

DOI: 10.60101/jarst.2024.257771

JOURNAL OF APPLIED RESEARCH ON SCIENCE AND TECHNOLOGY

Biopolymers, made from natural and environmentally friendly materials, have been developed for packaging applications, particularly in the pharmaceutical sector, aiming to sustainably reduce environmental pollution [3]. There were also many research had reported the studies of utilization of food production waste by mixing it with natural fiber. For example, the development of packaging was created from mango leaves [4]. A mixture of chitosan with olive pomace from the olive oil production process to produce packaging and film [5-6]. In addition, there was a large number of research on producing films and packaging made from various wasters, for instance, fruit peels [7] or pomegranate peels [8], potato waste with gallic acid [9], chitosan with polyphenols extracted from apple peels [10], and the use of chitosan mixed with apricot seed oil [11] or mango peel [12].

In addition, there were also research reports on the development of food additives, dietary supplements, new products such as pasta, milk, butter, crackers, cookies, etc., or the development of antioxidants in the form of powder or foam, or natural extracts developed from vegetable and fruit processing waste [13].

PBS is a biodegradable polymer made from bio-based biodegradable plastics. PBS is one of the most promising alternatives due to its good mechanical, thermal, and barrier properties, making it suitable for use in various applications. [14]. Additionally, during decomposition, PBS converts its product into water and carbon dioxide gas, releasing fewer toxic substances into the environment. For this reason, PBS is becoming another alternative plastic. Pure PBS is expanding in packaging and single-use products (disposal items) such as agricultural films, engineering materials, and medical materials [15]. However, the research on the value-adding of the galangal root waste was still limited. Research on how to increase the value of agricultural waste would be meritorious to the extent of its application.

The previous study developed corn waste from the corn milk production process into a biocomposite mixed with PBS at 80:20 (wt.%) by studying 2 levels of corn residue particle size (CK250 and CK400). The results showed that PBS/CK400 specimens showed better tensile force and had higher %elongation at break than PBS/CK250. However, PBS/CK250 had better flexural strength than PBS/CK400. The biocomposite contained a smaller size of corn residue powder and exhibited a higher density than PBS/CK400. The results of monitoring the natural degradation in soil burial tests showed that PBS/CK400 tended to have a faster degradation rate (R^2=0.8677) than PBS/CK250 due to its larger particle size [16].

Study investigated the effects of PBS and cassava pulp (CP250 and CP400 micron) with 5 different ratios (PBS100/CP0, PBS90/CP10, PBS80/CP20, PBS70/CP30, and PBS60/CP40) on the properties of biocomposites. The study found that the melt flow index of biocomposites significantly decreased with the increase in the CP content, as observed in both CP particle sizes. It was also observed that using CP400 for PBS80/CP20 resulted in a higher melt flow index than CP250. The PBS/CP biocomposites were shown to improve Young's modulus and hardness. However, tensile strength, elongation at break, and impact strength of the PBS/CP biocomposites decreased with increased CP. The addition of CP250 provided good particle dispersion and compatibility in the biocomposite matrix. This study suggested avoiding adding CP levels greater than 40% to maintain the structure's integrity. This study concluded that the biocomposite developed by PBS/CP could be useful in commodity packaging, outdoor plant pots, and injection molding as eco-friendly and biodegradable materials [17].

Nakhon Ratchasima province is an important area that produces fresh galangal supplies for the Northeastern markets [18]. Fresh galangals, both young and mature galangals, are generally used for many dishes. At the end of fresh-cut galangal production, many galangal roots are abundant on the farm. Usually, the farmer often leaves them in the agricultural field for compost, landfill, or burning.

Due to the environmental pollution resulting from plastic usage, especially single-use plastic packaging, this research attempted to add value to the abundant galangal root. Hence, this study aimed to develop a biocomposite composed of galangal root and PBS. It was hoped that this research would add value to agricultural waste. Moreover, this could result in the widespread adoption of various types of single-use food packaging that are environmentally friendly and made from renewable resources. Ultimately, this may promote the development of BCG (businesses that focus on sustainability and environmental responsibility).

MATERIALS AND METHODS

(a) Preparation of galangal root powder

The preparation of galangal root powder began with washing with tap water for 15 minutes to remove all impurities. Afterward, the galangal roots were cut into shorter pieces and dried in a hot air oven (FD115, Binder, Germany) at 80°C for 12 hrs with constant turning and mixing. At the end of drying, the final moisture of the dried galangal root was 17% (dry basis). The dried galangal root fragments were ground with a fine grinder at a 1 mm sieve size. After that, they are sieved with a stainless-steel sieve (W.S. Tyler, USA) to obtain galangal root powder with a size of 250 (GR250) and 400 (GR400) microns (Figure 1 (a), (b)). The galangal root powder was stored in a zip-lock bag and in a desiccator until used.

(b) PBS and preparation of PBS/GR biocomposite specimen

DOI: 10.60101/jarst.2024.257771

JOURNAL OF APPLIED RESEARCH ON SCIENCE AND TECHNOLOGY

PBS bioplastic pellet (PBS, grade: B3C03) was purchased from Teamplas R&D Co., Ltd. (Chachoengsao province, Thailand). The melting temperature and the density were about 170-200°C and 1.50 g/cm³ [17], respectively (Figure 1 (c)).

Figure 1 (a) GR250, (b) GR400, and (c) PBS pellets.

The PBS pellets were dried in a hot air oven to remove moisture before being used at 60°C for 3 hrs. After that, they were mixed with galangal root powder, which was labeled as PBS/GR250 and PBS/GR400. The mixing ratio between PBS and galangal root was 80:20 (wt.%). This ratio was chosen based on the previous study. Studies revealed that the optimal ratio between PBS and agricultural fiber was 20%. This is because lower or higher percentages of agricultural fiber than 20% reduced mechanical strength [19-21].

After that, the mixture was melted until homogeneous using an internal mixer to obtain the biocomposite in the form of strands. After the biocomposite strands obtained from the melt were allowed to cool down, they were passed through a shredder to obtain the biocomposite pellets. The biocomposite specimens were obtained by extrusion molding of biocomposite pellets with a hot extrusion machine at 150°C under a pressure of 10 MPa for 5 minutes.

Therefore, three different sizes of specimens needed to be prepared according to the standard methods for mechanical inspections. The specimens for tensile strength testing were produced according to ASTM D638 [22] in the form of type 2 dumbbells with a thickness of 3.2 mm, a narrow section width of 6 mm, a narrow section length of 33 mm, and a total length of 115 mm The specimens for impact resistance evaluations had dimensions of width x length x thickness of 13 mm x 63.5 mm x 3.2 mm by ASTM D256 [23]. The specimens for flexural strength assessments were prepared according to ASTM D790 [24] with a width x length x thickness of 12.7 mm x 127 mm x 3.2 mm. The specimens were stored in a desiccator until the tests were performed.

(c) Mechanical property evaluation

The PBS/GR250 and PBS/GR400 biocomposite specimens were tested for mechanical properties, including tensile, impact, and flexural strength. Experiments were conducted with 5 replicates. The tensile strength was performed using a universal testing machine (LLOYD, model 30k Plus, UK) with a 10 kN load cell and a 50 mm/minute crosshead speed. The specimens were held vertically in the Y-axis during the test and clamped at both ends. The tensile strength, stress, and % elongation at break were assessed. The tensile strength is the force that can be applied to a material before it yields (stretches irreparably) or breaks. The tensile stress is stress developed by a material bearing a tensile load [22].

For the Izod impact test of the specimens, a pendulum impact tester (INSTRON, model CEAST 9050, USA) was used according to ASTM D256. The specimens were clamped at one end and fractured after being hit by a pendulum with an impact energy of 2.7 Joule.

For the flexural strength test, during testing, the specimens were clamped at both ends in a flat position with a support span-to-depth ratio of 16:1. The tests were performed on a universal testing machine (LLOYD, model 30k Plus, UK), using the three-point bending fixture at a crosshead speed of 5 mm/minutes. The flexural strength (MPa), flexural stress, and Flexural Modulus (GPa) were measured.

(d) Physical property assessment

Physical property evaluations for biocomposites include water absorption, density, morphology, and weight loss percentage during burial tests. Experiments were conducted with 5 replicates.

According to ISO 535 (2014) [25], the water absorption test was conducted by weighing a 12 mm x 63 mm x 3 mm specimen before and after immersing it in distilled water for 60 minutes. The water absorption was calculated using Equation (1)

$$\text{Water absorption} = \frac{W_f - W_i}{W_i} \text{x}100 \qquad (1)$$

where

W_i = weight of the specimen before immersion, g
W_f = weight of the specimen after immersion, g

The density was calculated from the relationship between weight and volume. The weight of the specimen was measured directly using a three-point precision electrical balance (AND brand, model FX-300i, Japan). The volume of the specimen was determined via the dimensions of the specimen using the digital vernier caliper, and then the volume was calculated. The density of the specimen was calculated using Equation (2).

$$\rho = \frac{m}{v} \qquad (2)$$

DOI: 10.60101/jarst.2024.257771

where ρ = density, g/cm^3
m = mass, g
v = volume, cm^3

The natural degradation of the biocomposite specimen was determined by a burial test. The burial test was conducted at the field of the Department of Agricultural Machinery Engineering, Faculty of Engineering and Technology, Rajamangala University of Technology Isan, Nakhon Ratchasima, Mueang Nakhon Ratchasima District, Nakhon Ratchasima Province, at latitude 14°59'06.9"N and longitude 102°07'11.0"E. The soil was a clay loam type. The six holes with dimensions of width 25 cm x length 15 cm x depth 15 cm [26] were constructed. All specimens were weighed and recorded as initial values to monitor the natural degradation. After that, five specimens were buried in each hole. Burial periods were 0, 7, 21, and 121 days. After excavation, the specimens were washed with tap water to remove dirt and dried in a hot air oven (FD115, Binder, Germany) at 60°C for 24 hrs. to remove moisture. The specimens were then weighed. The natural degradation was expressed as a percentage of weight loss and calculated using Equation (3).

$$\text{Weight loss, \%} = \left[\frac{(W_i - W_f)}{W_i}\right] \text{x100} \quad (3)$$

where
W_i = weight of the specimen before burial test, g
W_f = the weight of the specimen after burial test, g

The morphological investigation for the microstructure of the biocomposite was conducted on the cross-section area and the surface after the tensile test using a scanning electron microscope and energy dispersive x-ray spectrometer (SEM-EDS) (Quanta 250, FEI Company, Hillsboro, Oregon, USA) without prior specimen preparation. Morphological observations of each sample were performed at 300x and 1000x magnifications.

RESULTS AND DISCUSSION

Galangal root was the waste from the fresh-cut galangal process. This study turned this waste into fiber-reinforced biopolymer composites. Additionally, they measured the mechanical and physical properties. The results are revealed below.

(a) Mechanical properties of PBS/GR biocomposites

Table 1 displays the tensile strength, stress, and %elongation at break. PBS/GR250 presented the higher tensile strength, tensile stress, and %elongation at break at 22.19 MPa, 8.87 MPa, and 1.72%, respectively. Besides, it was observed that PBS/GR400 illustrated the lower tensile strength, tensile stress, and %elongation at break at 21.06 MPa, 7.66 MPa, and 1.16%, respectively. Furthermore, studies reported tensile strength, tensile stress, and %elongation at break of neat PBS at 32.73 MPa [20], 29.28 MPa [17], and 17.50% [20], respectively. It was seen that the tensile strength, tensile stress, and %elongation at break of both PBS/GR250 and PBS/GR400 samples were lower than pure PBS. This could reflect that adding GR250 and GR400 into PBS-based biocomposite could cause reductions in structural integrity and elasticity, similar to the previous observation [17]. The present study could suggest that pure PBS was stronger and more flexible than the PBS/GR biocomposites. The reduction of elongation of the PBS/GR biocomposites might be affected by the decrease in the deformability of the rigid interface between the fiber and the matrix [27]. However, another study found an opposite trend. This study revealed that adding 20% surface modification of jute fiber with 80% PBS greatly increased tensile strength and tensile modulus [19].

Table 1 Tensile test results.

Parameters	PBS/GR 250	PBS/GR 400	Neat PBS
Tensile strength (MPa)	22.19 ±1.19	21.06 ±1.16	32.73 [20]
Tensile stress (MPa)	8.87 ±0.99	7.66 ±1.62	29.28 [17]
Elongation at break (%)	1.72 ±0.50	1.16 ±0.23	17.50 [20]

Table 2 Impact test results.

Parameters	PBS/GR 250	PBS/GR 400	Neat PBS
Absolute energy (%)	1.73 ±0.27	1.66 ±0.32	-
Impact strength (kJ/m²)	1.55 ±0.26	1.45 ±0.28	6.20 [20]
Energy (J)	0.04 ±0.01	0.04 ±0.01	-

Generally, the impact test indicates the material's toughness and displays it via absolute energy, impact strength, and the absorbed energy during sudden loading. The impact strength of PBS/GR biocomposites was evaluated, and the results are shown in Table 2. This study observed that PBS/GR250 showed absolute energy, impact strength, and energy at 1.73%, 1.55 kJ/m^2, and 0.04 J, respectively. Meanwhile, absolute energy,

DOI: 10.60101/jarst.2024.257771

impact strength, and energy of PBS/GR400 were at 1.66%, 1.45 kJ/m^2, and 0.04 J, respectively. The lower impact strength compared to neat PBS observed by the present study was in line with the previous report [28]. This could be due to the fiber matrix interface playing a major role between matrices; consequently, a poor matrix interface could lead to weaker impact resistance.

It was reported that the impact strength of neat PBS was at 6.20 kJ/m^2 [20]. It could be implied that adding galangal powder of 250 and 400 microns into PBS-based biocomposite decreases the toughness drastically. Pure PBS could resist more impact force due to PBS having flexibility, but PBS mixed with natural fiber would not resist the impact force [29]. It may be influenced by the arrangement of the physical bonding structure between the fiber particles of the filler material and the matrix while the two materials were melted together [30-31].

The flexural test indicates the bending property of the material under three-point loading conditions. The flexural properties of PBS/GR biocomposites were measured, and the results are displayed in (Table 3). This study observed that the flexural strength, flexural stress, and Flexural Modulus of PBS/GR250 were 14 MPa, 13.93 MPa, and 3,239.16 MPa, respectively. The flexural strength, flexural stress, and Flexural Modulus of PBS/GR400 were 13 MPa, 11.03 MPa, and 2,807.02 MPa, respectively.

Table 3 Flexural strength test results.

Parameters	PBS/GR 250	PBS/GR 400	Neat PBS
Flexural strength (MPa)	14 ±1.00	13 ±0.80	45 [21]
Flexural Stress (MPa)	13.93 ±3.06	11.30 ±2.81	-
Flexural Modulus (MPa)	3,239.16 ±398.13	2,807.02 ±506.93	1,250 [32]

Table 4 Water absorption and density test results.

Parameters	PBS/GR 250	PBS/GR 400
Water absorption	0.00	0.00
Density (g/cm^3)	1.16 ±0.01	1.05 ±0.02

The flexural strength of neat PBS was reported at 45 MPa [21]. Comparing the flexural strength between PBS/GR and the neat PBS, it is seen that adding galangal powder into PBS-based biocomposite could cause a reduction of flexural strength more than 3 times. The Flexural Modulus of the pure PBS was reported at 916 MPa [21] and 1,250 MPa [32]. The present study observed a massive increase in the Flexural Modulus of PBS/GR250 and PBS/GR400, similar to the reports [19, 21]. These two studies reported that PBS biocomposites reinforced with surface-modified jute fiber, PBS-bagasse, PBS-coconut shell, PBS-curaua, and PBS-sisal increased their Flexural modulus drastically.

The large increase in the Flexural Modulus could be due to the rough surface of the galangal particle promoting the adhesion with the PBS matrix, improving the Flexural Modulus [21]. Compared to the neat PBS, the present study observed that PBS/GR biocomposites presented a higher property of the Flexural Modulus at 2.6 and 2.2 times for PBS/GR250 and PBS/GR400 biocomposites, respectively. These results could suggest that they might have more stability, longevity, and load-bearing capacity than neat PBS.

Tensile, impact and flexural tests of the PBS/GR250 biocomposites presented slightly higher than PBS/GR400 biocomposites. This could be due to the similarity of surface interference between PBS and galangal fiber.

(b) Physical properties of PBS/GR biocomposites

The water absorption of PBS/GR biocomposite was assessed, and the results are shown in Table 4. According to ISO 535, when measuring the water absorption at a specific time (60 min.), it was observed that the water absorption of PBS/GR250 and PBS/GR400 were shown at zero. These results suggest that PBS/GR did not have the water absorption characteristics after 1 hr. A study of the water absorption percentage of the PBS80/curaua20 biocomposite presented the continued increasing trends of the water absorption percentage after 8 hrs [33]. This study observed that the water absorption percentages were at 0.8 wt.% after the first hour and increased to 1.5 wt.% after 8 hrs. The study reported that the neat PBS presented the lowest water absorption of 3.25% after two days of immersion in distilled water at room temperature [30]. They observed that the water absorption of pure PBS became stable after eight days and remained at 3.53% until day 14.

The present study revealed that zero water absorption percentage after 1 hr could be affected by the water molecules having difficulty accessing the PBS/GR fiber in the matrix domains [34], which is related to the fiber distribution and properties. The crucial factor that affected the water absorption was the formation of voids during the melting process, resulting in structural inhomogeneity between copolymer and PBS [35]. However, many factors, such as porosity, lumen size, fiber-matrix adhesion [36], fiber distribution, fiber length, fiber shape, and fiber content [33], were able to influence the water absorption behavior of the biocomposites.

DOI: 10.60101/jarst.2024.257771

The density of the PBS/GR biocomposite was also determined, and the results are shown in Table 4. It was observed that PBS/GR250 and PBS/GR400 presented densities of 1.16 and 1.05 g/cm^3. It could be noted that PBS/GR250 presented smaller particles and tended to have higher density than PBS/GR400. Generally, smaller particles have a larger total surface area than larger particles of the same material. The smaller particles could also pack more tightly due to increased surface interactions and the potential for better interparticle contact. Therefore, PBS/GR250 presented higher density compared to PBS/GR400. However, natural fiber is less dense (1.2-1.6 g/cm^3) than other materials [37].

The PBS/GR biocomposites were observed in their natural decomposition by soil. The results of weight loss are illustrated in Table 5. Figure 2 demonstrates the microstructure of both biocomposites at 0 days and 121 days.

The PBS/GR biocomposites were observed in their natural decomposition by soil burial. The results of weight loss are illustrated in Table 5. Figure 2 demonstrates the microstructure of both biocomposites at 0 days and 121 days.

Table 5 Percentage of weight loss during burial test.

Burial day	PBS/GR 250	PBS/GR 400
0	0	0
7	0	0
21	0.289 ±0.09	0.498 ±0.06
121	7.480 ±0.50	15.600 ±0.23

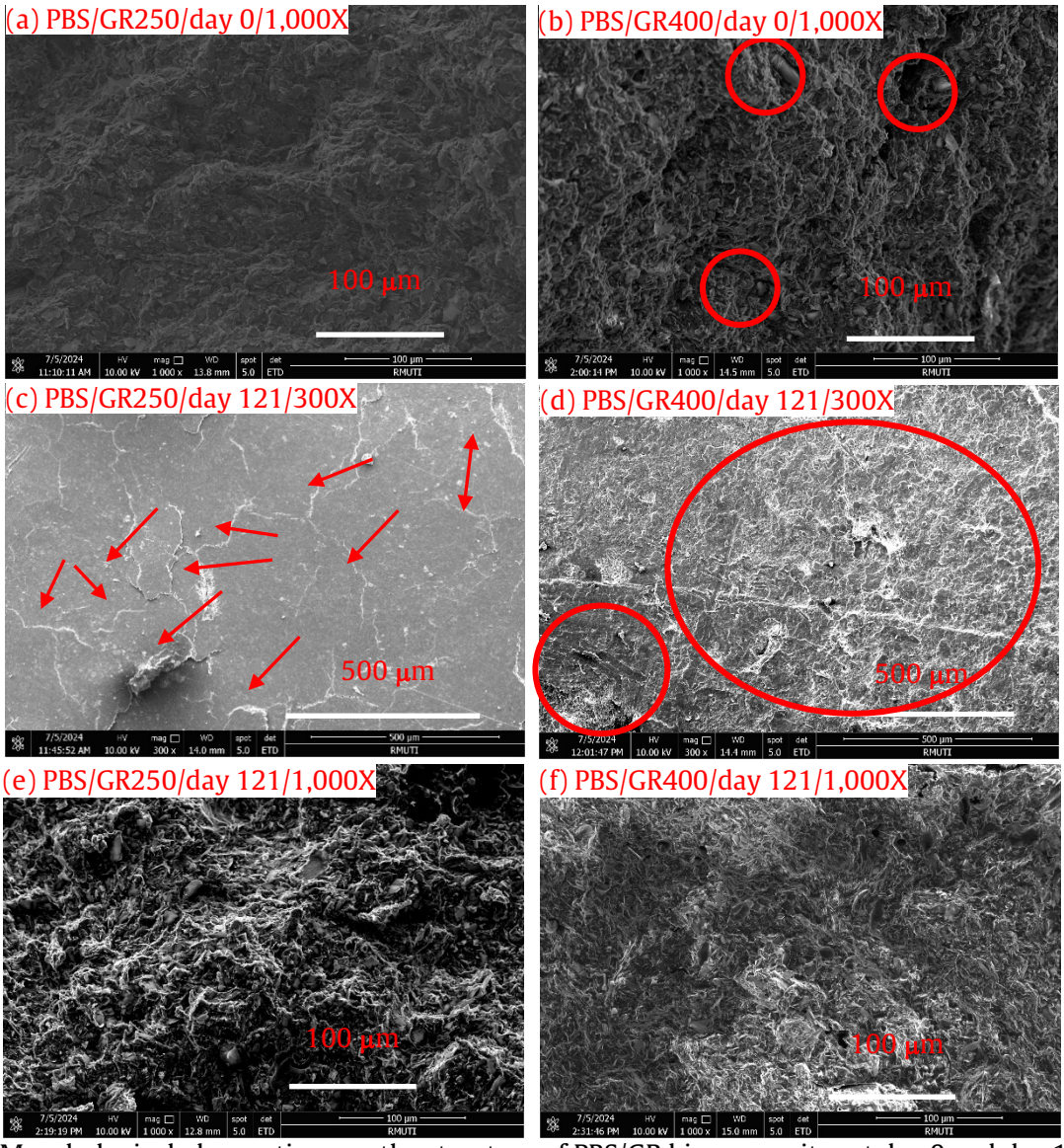

Figure 2 Morphological observations on the structure of PBS/GR biocomposites at day 0 and day 121 during burial test at 300X and 1000X magnifications (a, b, e, f display cross-section area; c, d display surface area). The red arrows in (c) point out cracks. The red circles in (d) indicate many cracks and broken surfaces.

DOI: 10.60101/jarst.2024.257771

The results of monitoring the natural degradation by burial test were conducted on days 0, 7, 21, and 121. It was found that the percentage of weight loss of PBS/GR400 increased by double compared to PBS/GR250 after burial for 121 days. Figure 2 (b) displays the coarse particles (red circles) of galangal root powder compared to PBS/GR250 (Figure 2 (a)).

Considering the weight loss percentage of PBS/GR biocomposites, it could imply that PBS/GR400 tended to degrade well compared to PBS/GR250. This was consistent with the morphological observation in Figure 2 (d). PBS/GR400 on day 121 presented the structure as degraded and promoted a huge number of cracks (Figure 2 (d), (f)). PBS/GR250 also observed many cracks on the surface, but they were less than those observed by PBS/GR400 (Figure 2 (c)).

These could initiate the collapse of the structure as supported by a loosened structure (Figure 2 (c), (d)). The finding of lower density at 1.05 g/cm^3 of PBS/GR400 could also support the morphological observation after 121 days of burial test. Lowering density could relate to loosening surface interactions and lower interparticle contact, resulting in faster degradation in PBS/GR400.

CONCLUSIONS

This research used the leftover galangal roots from the fresh-cut process of galangal to be mixed with PBS biopolymer. The objective was to develop a biocomposite composed of galangal root and PBS. The benefits of the present study would be adding value to agricultural waste, reducing waste, and protecting the environment by further developing this waste. PBS/GR250 and PBS/GR400 biocomposites could resist the flexural forces. All biocomposite samples did not show the percentage of water absorption, and all samples present low density. PBS/GR400 presented twice higher weight loss percentages than PBS/GR250. This implied that PBS/GR400 tended to have a faster natural degradation rate. The results of this study could be further developed into single-use food containers. The production sectors for food packaging technology are already available for a wide range of industrial productions. It would be possible to do this in a mass-production manner, and it could be more cost-effective.

ACKNOWLEDGEMENT

The authors would like to thank Faculty of Engineering and Technology Rajamangala University of Technology Isan for providing funding to support this research study according to capital contract no. NR2567INC036 on the fiscal year 2024.

REFERENCES

1. Visakha Phuchinda. Monitoring and evaluation project to promote the reduction of single-use plastics. Complete report [Internet]. Department of Environmental Quality Promotion, Ministry of Natural Resources and Environment; 2023 [cited 2024 Jun 24]. Availability from: http://164.115.46.29/media/details?media_group_code=10&media_type_id=30&media_id=4903.
2. FAO. The State of Food and Agriculture 2019. Moving forward on food loss and waste reduction [Internet]. Food and Agriculture Organization of the United Nations; 2019 [cited 2023 Dec 12]. Availability from: https://www.fao.org/3/ca6030en/ca6030en.pdf.
3. Baranwal J, Barse B, Fais A, Delogu GL, Kumar A. Biopolymer: a sustainable material for food and medical applications. Polymers. 2022;14:983.
4. Rambabu K, Bharath G, Banat F, Show PL, Cocoletzi HH. Mango leaf extract incorporated chitosan antioxidant film for active food paGRaging. Int J Biol Macromol. 2019;126:1234-43.
5. de Moraes Crizel T, de Oliveira Rios A, Alves VD, Bandarra N, Moldão-Martins M, Flôres SH. Active food paGRaging prepared with chitosan and olive pomace. Food Hydrocolloids. 2018;74:139-50.
6. Moudache M, Colon M, Nerín C, Zaidi F. Phenolic content and antioxidant activity of olive by-products and antioxidant film containing olive leaf extract. Food Chem. 2016;212:521-27.
7. Hanani ZAN, Husna ABA, Syahida SN, Nor-Khaizura MAB, Jamilah B. Effect of different fruit peels on the functional properties of gelatin/polyethylene bilayer films for active paGRaging. Food PaGRaging and Shelf Life. 2018;18:201-11.
8. Hanani ZAN, Yee FC, Nor-Khaizura MAR. Effect of pomegranate (*Punica granatum* L.) peel powder on the antioxidant and antimicrobial properties of fish gelatin films as active paGRaging. Food Hydrocolloids. 2019;89:253-59.
9. Zhao Y, Saldaña MDA. Use of potato by-products and gallic acid for development of bioactive film paGRaging by subcritical water technology. The Journal of Supercritical Fluids. 2019;143:97-106.
10. Riaz A, Lei S, Akhtar HMS, Wan P, Chen D, Jabbar S, et al. Preparation and characterization of chitosan-based antimicrobial active food paGRaging film incorporated with apple peel polyphenols. Int J of Bio Macromolecules. 2018;114: 547-55.
11. Priyadarshi R, Sauraj Kumar B, Deeba F, Kulshreshtha A, Negi YS. Chitosan films incorporated with Apricot

(*Prunus armeniaca*) kernel essential oil as active food packaging material. Food Hydrocolloids. 2018;85: 158-66.

12. Nor Adilah A, Jamilah B, Noranizan MA, Nur Hanani ZA. Utilization of mango peel extracts on the biodegradable films for active packaging. Food Packag Shelf Life. 2018;16:1-7.
13. Dilucia F, Lacivita V, Conte A, Nobile MAD. Sustainable use of fruit and vegetable by-products to enhance food packaging performance. Foods. 2020;9:857.
14. Peñas MI, Pérez-Camergo RA, Hernández R, Müller AJ. A Review on current strategies for the modulation of thermomechanical, barrier, and biodegradation properties of poly (butylene succinate) (PBS) and its random copolymers. Polymers. 2022;14:1025.
15. Office of Agricultural Economics, 2015. Polybutylene succinate (PBS) [Internet]. PACKAGING INDUSTRIAL INTELLIGENCE UNIT; [cited 2024 Nov 10]. Availability from: https://packaging.oie.go.th/new/admin_control_new/html-demo/file_technology/9480617235.pdf.
16. Jantana S, Jannok P, Nithikarnjanatharn J. Mechanical and Physical Properties of Poly (lactic acid)-Based Biocomposite Composed of Food Production Residue. In: World Integrated Chemical and Material Engineering Technology Conference 2023; Bangkok, Thailand. WICMETC; 2023.
17. Nithikarnjanatharn J, Samsalee N. Effect of cassava pulp on Physical, Mechanical, and biodegradable properties of Poly(Butylene-Succinate)-Based biocomposites. Alexandria Engineering Journal. 2022;61:10171-81.
18. Kha lueang : galangal [Internet]. Thailand: Department of Agricultural Extension. 2024 [cited 2024 Nov 10]. Availability from: http://www.agriman.doae.go.th/herbal/herbdoae005/kha%20lueang.pdf.
19. Liu L, Yu J, Cheng L, Qu W. Mechanical properties of poly(butylene succinate) (PBS) biocomposites reinforced with surface modified jute fiber. Composites: Part A. 2009;40:669-74.
20. Prasoetsopha N, Thainoi P, Jinnavat R, Charerntanom W, Hasook A, Singsang W. Morphological and Mechanical Properties of Natural Rubber Compound/Poly(butylene succinate) Blend. IOP Conf Ser Mater Sci Eng. 2020;840:012013.
21. Mochane MJ, Magagula SI, Sefadi SJ, Mokhena TC. A review on green composites based on natural fiber-reinforced polybutylene succinate (PBS). Polymers. 2021;13:21-38.
22. ASTM International (ASTM D638). Standard test method for tensile properties of plastics, in annual book of ASTM standards. West Conshohocken: ASTM International; 2022.
23. ASTM International (ASTM D256). Standard test methods for determining the Izod pendulum impact resistance of plastics, in annual book of ASTM standards, West Conshohocken: ASTM International; 2018.
24. ASTM International (ASTM D790. Standard test methods for flexural properties of unreinforced and reinforced plastics and electrical insulating materials, in annual book of ASTM standards. West Conshohocken: ASTM International; 2017.
25. ISO, Paper and board-Determination of water absorptiveness-Cobb method. 4th ed. International standard. 2023.
26. Suntudprom J, Phiaphumipong P, Jannok P, Meeklangsaen W, Sukthang N, Prangpru N, et al. Adding value to waste from corn cob for producing biocomposites. In the 14th Academic Conference of Engineering and Architecture; 2023 Aug 25; Kalasin, Thailand: Kalasin University; p. 258-68.
27. Vorawongsagul S, Pratumpong P, Pechyen C. Preparation and foaming behavior of poly (lactic acid)/poly (butylene succinate)/cellulose fiber composite for hot cups packaging application. Food Packag Shelf Life. 2021;27:100608.
28. Zhao L, Huang H, Han Q, Yu Q, Lin P, Huang S, et al. A novel approach to fabricate fully biodegradable poly(butylene succinate) biocomposites using a paper-manufacturing and compression molding method. Composites Part A: Applied Science and Manufacturing. 2020;139:106117.
29. Sirichalarmkul A, Kaewpirom S. Enhanced biodegradation and processability of biodegradable paGRage from poly(lactic acid)/poly(butylene succinate)/rice-husk green composites. J Appl Polym Sci. 2021;138(27):50652.
30. Ferdináand M, Várdai R, Móczó J, Pukánszky B. Poly (lactic acid) reinforced with synthetic polymer fibers: interactions, structure, and properties. Compos Part A-Appl S. 2023;164:107318.
31. Ruzuqi R. Impact strength analysis of polymer composite materials (PCM) fiber reinforced in the fiberboat application. Material Science Research India. 2020;17(2):170-8.

DOI: 10.60101/jarst.2024.257771

JOURNAL OF APPLIED RESEARCH ON SCIENCE AND TECHNOLOGY

32. Badrinath R, Senthilvelan T. Comparative investigation on mechanical properties of banana and sisal reinforced polymer-based composites. Procedia material science. 2014;5:2263-72.

33. Frollini E, Bartolucci N, Sisti L., Celli A. Biocomposites based on poly(butylene succinate) and curaua: Mechanical and morphological properties. Polymer Testing. 2015;45:168-73.

34. Frollini E. Bartolucci N. Sisti L. Celli A. Poly (Butylene Succinate) reinforced with different lignocellulosic fibers. Ind Crops Prod. 2013;45: 160-9.

35. Saffian HA, Yamaguchi M, Ariffin H, Abdan K, Kassim NK, Lee SH, et al. Thermal, physical and mechanical properties of poly(butylene succinate) /kenaf core fibers composites reinforced with esterified lignin. Polymers. 2021;13:2359.

36. Mariatti M, Jannah M, Abu Bakar A, Khalil HA. Properties of banana and pandanus woven fabric reinforced unsaturated polyester composites. J Compos Mater. 2008;42:931-41.

37. Girijappa YGT, Rangappa M S, Parameswaranpillai J, Siengchin S. Natural fibers as sustainable and renewable resource for development of eco-friendly composites: A comprehensive review. Frontiers in Materials. 2019;6:226.

DOI: 10.60101/jarst.2024.257771

Received: January 28, 2024 | Revised: March 10, 2025 | Accepted: March 12, 2025

Laser-assisted FTO/WO_3/$BiVO_4$ photoanode fabrication for enhanced photoelectrocatalytic performance and durability for organic dye degradation

Watcharapong Nareejun[1], Chatchai Ponchio[*1, 2]

[1]Department of Chemistry, Faculty of Science and Technology, Rajamangala University of Technology Thanyaburi, Pathum Thani 12120, THAILAND

[2]Advanced Photochemical and Electrochemical Materials (APEM) Research Unit, Faculty of Science and Technology, Rajamangala University of Technology Thanyaburi, Pathum Thani 12110, THAILAND

[*]Corresponding author: chatchai@rmutt.ac.th

ABSTRACT

A significant challenge in the photoelectrocatalytic method for water oxidation and organic decomposition processes is the fabrication of scalable, durable, and efficient photoanodes. Several limitations, such as insufficient adhesion, uneven semiconductor coatings, and low durability, often lead to the unsatisfactory performance of the conventional FTO/WO_3/$BiVO_4$ photoanode. This study improves the surface properties of fluorine-doped tin oxide (FTO) substrates using a laser treatment process prior to the automated dip-coating of WO_3 and $BiVO_4$ semiconductor layers. The FTO substrate surface is textured and modified using laser induction as part of the fabrication process. Thereafter, WO_3 and $BiVO_4$ semiconductor layers are deposited in sequence. The laser treatment can promote surface homogeneity, semiconductor adhesion, and the active surface area of the fabricated FTO/WO_3/$BiVO_4$. The morphology, elemental composition, and electrochemical properties are analyzed using SEM, EDS, and EIS techniques. In that context, the laser-treated FTO/WO_3/$BiVO_4$ photoanode development significantly outperformed those without treatment. The FTO/WO_3/$BiVO_4$ photoanode that was treated with a laser had a lower energy band gap of 1.8 eV, a higher capacitance of 4.91×10^{-6} F, and a higher photocurrent density of 5.5 mA/cm² compared to an electrode that was not treated with a laser at a bias potential of 1.0 V. The durability assessments demonstrated that the organic dye removal efficacy persisted after 1,000 hours. This study demonstrates that laser-treated FTO/WO_3/$BiVO_4$ photoanodes can overcome conventional fabrication method limitations. This successfully provides a scalable and effective alternative for various applications, including wastewater treatment and renewable energy. It is recommended that subsequent studies should focus on the evaluation of the applicability of this laser-assisted method to various kinds of environmental applications and photoelectrodes.

Keywords: Photoelectrocatalytic process, WO_3/$BiVO_4$, Laser treatment, Organic dye degradation

INTRODUCTION

Increasing interest in efficient and sustainable alternative energy production and environmental management is contributing to extensive photoelectrocatalytic process research [1-3]. The FTO/WO_3/$BiVO_4$ photoanode is now recognized as an attractive alternative for water oxidation and organic dye degradation owing to its advantageous optical and electrical characteristics [4-6]. Conventional methods for fabricating these electrodes frequently yield limited efficiency, unsatisfactory durability, and insufficient reproducibility, principally due to difficulties in achieving homogenous semiconductor coatings and effective charge transfer at the electrode interface [7]. In order to improve the structural and functional features of photoelectrodes, recent breakthroughs have brought to light the significance of modifying the substrate. It has been demonstrated that roughening treatments, such as the use of a laser, can enhance surface adhesion, increase the degree of active surface area, and facilitate the absorption of light [8-10]. Furthermore, the long-term durability and scalability of these methods for practical applications have not yet been appropriately assessed in the context of FTO/WO_3/$BiVO_4$ systems. This study addresses those weaknesses through implementing a laser-assisted method for modifying FTO substrates before semiconductor immobilization through an automated dip-coating procedure. The suggested technology integrates laser-induced surface roughness with efficient material deposition to create a homogeneous, porous structure that improves light absorption, charge transfer, and overall photoelectrocatalytic efficacy. The study assesses the durability and reproducibility of the laser-treated electrodes, offering insights into their appropriateness for large-scale wastewater treatment and energy applications. This investigation

DOI: 10.60101/jarst.2024.260565

provides an alternative process for enhancing the performance of FTO/WO_3/$BiVO_4$ photoanodes. The methodology integrates efficient application with material design, resulting in the progression of sustainable technology.

MATERIALS AND METHODS

3.1 Preparation of WO_3 and $BiVO_4$ precursor solutions

A 0.1 M WO_3 precursor solution was prepared by dissolving tungstic acid (99%, H_2WO_4, Aldrich Chemistry) in an ammonium hydroxide (30%, NH_4OH, Panreac) solution. The solution was refluxed at 60°C for one hour with constant agitation. To maintain a consistent solution volume, incrementally introduce NH_4OH while refluxing, continuously stirring the solution for one hour. The resultant solution, after one hour of stirring, will initially appear milky white and subsequently transition to a clear solution, without forming a suspension after settling for one night. A 0.05 M $BiVO_4$ solution was prepared by dissolving 0.1 M bismuth nitrate (≥98.0%, $Bi(NO_3)_3{\cdot}5H_2O$, Sigma-Aldrich) powder in acetic acid (99.8%, CH_3COOH, ACI Labscan) and stirring for 20 minutes. Concurrently, 0.1 M vanadyl acetyl acetonate (98.0%, $C_{10}H_{14}O_5V$, Sigma-Aldrich) powder was solubilized in an acetylacetone (99.5%, $CH_3COCH_2COCH_3$, Panreac) solution and agitated for 20 minutes. The two solutions were subsequently combined and agitated for 10 minutes, followed by ultrasonication for 120 minutes to achieve homogeneity, yielding a blue-green solution of 0.05 M $BiVO_4$.

3.2 Fabrication of FTO/WO_3/$BiVO_4$ photoanode

Figure 1 illustrates the deposition process, emphasizing each step in the fabrication of FTO/WO_3/$BiVO_4$ electrodes. These electrodes have been developed for improved photoelectrocatalytic efficiency for water oxidation and the organic dyes degradation process.

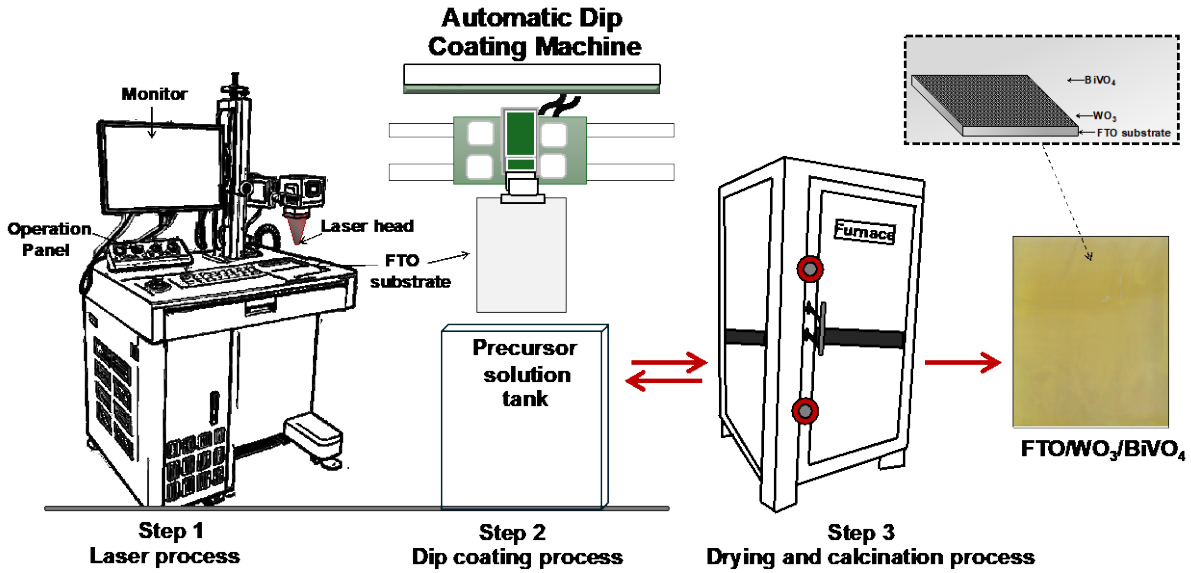

Figure 1 The FTO/WO_3/$BiVO_4$ photoanode fabrication process using an automatic dip coating machine through the FTO substrate treatment using the laser process.

3.2.1 Substrate preparation and laser treatment

Fluorine-doped tin oxide (FTO) conductive glass substrates (21 x 32 cm) were cleaned to remove all contamination and provide suitable surface preparation. The cleaning procedure included a sequential wash using detergent, ethanol, and distilled water, with each step employing 15 minutes. The cleaned and dried FTO substrate surfaces were modified using laser treatments to create a surface with a rough texture that was favorable for the adhesion of precursor solutions. A 30-watt fiber laser (RAYCUS-30) with a wavelength of 1,064 nm was employed at a distance of 30 cm above the FTO surface to attain the requisite roughness while maintaining the substrate's electrical characteristics.

3.2.2 WO_3 Thin Film Deposition

The laser-treated FTO substrates were immersed in a 0.1 M WO_3 precursor solution using an automated dip-coating technique. Consistent dipping and pulling speeds were set at 2.0 cm/s to ensure a uniform coating. The coated substrates were subjected to drying at 150°C for 5 minutes and subsequently calcined at 500°C for 30 minutes. This approach produced FTO/WO_3 electrodes with a distinct semiconductor thin layer.

3.2.3 $BiVO_4$ thin film deposition

The FTO/WO_3 electrodes were subsequently coated with a 0.05 M $BiVO_4$ precursor solution employing the same automated dip-coating method. The electrodes were dipped at a velocity of 2.0 cm/s for 15 seconds and subsequently pulled at a lowered speed of 1.5 cm/s to ensure a consistent layer. The electrodes were heated at 150°C for 5 minutes, followed by calcination at 550°C for 1 hour. This procedure provided FTO/WO_3/$BiVO_4$ electrodes exhibiting improved structural and semiconductor characteristics.

DOI: 10.60101/jarst.2024.260565

JOURNAL OF APPLIED RESEARCH ON SCIENCE AND TECHNOLOGY

3.3 FTO/WO_3/$BiVO_4$ photoanode characterization and photoelectrocatalytic activity study

This study examined the impact of laser-treated and untreated FTO substrates on the photoelectrocatalytic performance of FTO/WO_3/$BiVO_4$ electrodes. We evaluated the impact of laser treatment on the developed FTO/WO_3/$BiVO_4$ photoanode through its characteristics and photoelectrocatalytic properties. The elemental composition and morphology of the fabricated electrodes were investigated using energy-dispersive X-ray spectroscopy (EDS; OXFORD, INCA-350) and scanning electron microscopy (SEM; JEOL, JSM-5410LV). The Shimadzu UV-2401PC spectrophotometer was employed to determine the spectrum of light that an electrode could absorb, with air serving as the baseline. The photoelectrocatalytic cell was provided with three electrodes: the working electrode was FTO/WO3/BiVO4, the counter electrode was platinum (Pt), and the reference electrode was Ag/AgCl (sat. KCl). For water oxidation experiments, the three electrodes were connected to a potentiostat (Princeton Applied Research, Inc., VersaSTAT3). The electrolyte solution was prepared using 0.1 M Na_2SO_4, which exhibited a conductivity of less than 5 µS/cm. A VersaSTAT3 potentiostat was employed to conduct electrochemical impedance spectroscopy (EIS) across a frequency spectrum of 100,000 to 0.1 Hz. The electrochemical cell is provided with a stainless steel cathode (21 x 32 cm), an FTO/WO_3/$BiVO_4$ anode (21 x 32 cm), and a controlled applied potential of 2.0 V. The research employed a 14.4-watt light-emitting diode (LED) as the visible light source for photoelectrocatalytic investigations at an intensity of 2,000 LUX. The cathode electrode was placed 4 cm from the anode electrode. In order to investigate the degradation of photoelectrocatalytic organic pigments, a 0.5 M NaCl solution was combined with 5 ppm of Orange Red. The reaction occurred in the presence of visible light from a 14.4-Watt LED source ($\lambda > 420$ nm) that was 26.47 mW/cm² bright and evenly dispersed the light. Over 1,000 hours of testing were conducted to determine the longevity of the dye, which was measured at 483 nm every 10 minutes for a maximum of an hour using a Shimadzu UV-2401PC spectrophotometer.

RESULTS AND DISCUSSION

4.1 Morphology and elemental composition

Figure 2 illustrates the morphological examination of FTO and FTO/WO_3/$BiVO_4$ electrodes, both with and without laser treatment, as examined using SEM.

Laser-treated FTO substrates display significantly smaller particles owing to the optimum laser head distance of 30 cm, which enhances surface roughness without noticeably impacting electrical conductivity (Figure 2a-b). The rough, extremely porous surfaces of the laser-treated electrodes were characterized, increasing the active surface area of the coated WO_3 and $BiVO_4$ semiconductors on the FTO substrate, which is essential for oxidation reaction performance [11]. On the other hand, electrodes that have not been treated have fewer pores and a rougher surface, which makes them less catalytic (Figure 2c–d). The inset of the figure shows the photographs of each electrode to demonstrate the physical characteristics of the prepared electrodes. The FTO/WO_3/$BiVO_4$ electrodes show a distinct yellow color, which is consistent with the yellow color of WO_3 and $BiVO_4$, which confirming the existence of the two semiconductors. Figure 3 illustrates cross-sectional SEM images of bare FTO and FTO/WO_3/$BiVO_4$. The FTO layer thickness was probably 350 nm, while the WO_3 and $BiVO_4$ layers consolidated into an overall layer of approximately 400 nm subsequent calcination. These results demonstrate the effects of heterojunction formation on the structure.

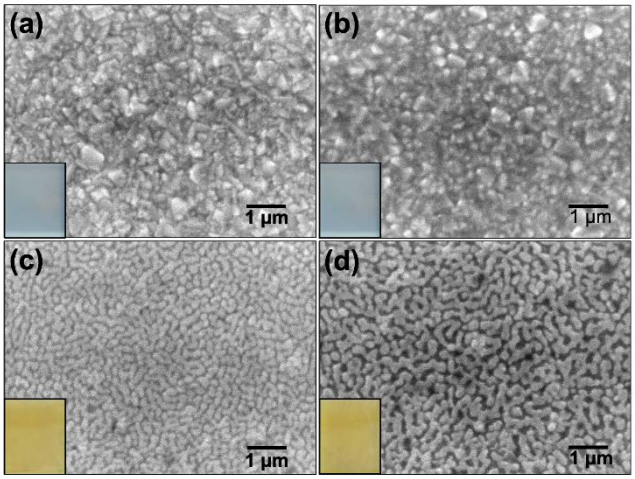

Figure 2 Morphology of FTO electrodes; (a) untreated, (b) with laser-treatment, and (c) FTO/WO_3/$BiVO_4$ electrodes; untreated, (d) with laser-treatment; inset of image of each electrode.

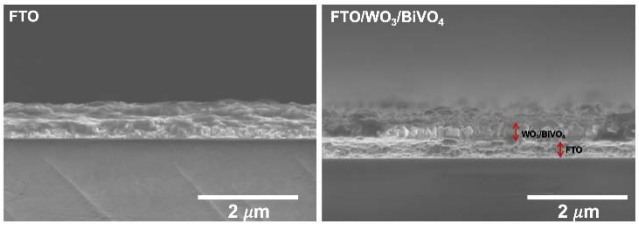

Figure 3 FE-SEM image at the cross-sectional view of the FTO and FTO/ WO_3/ $BiVO_4$ (with laser-treatment)

The structure of bare FTO is compact and smooth, whereas the FTO/WO_3/$BiVO_4$ hybrid is well-defined and has numerous layers, resulting in a denser and rougher surface appearance.

The absorption of light and the separation of charges are enhanced when WO_3 and $BiVO_4$ layers are effectively combined, thereby reducing the recombination

DOI: 10.60101/jarst.2024.260565

loss. The coarser, more porous structure facilitates the movement of charges and provides a greater surface area for catalytic processes. This directly results in improved photoelectrocatalytic (PEC) performance. Additionally, the product's durability and stability are guaranteed by the robust interfacial bonding between layers. The laser-assisted fabrication method enhances the heterojunction characteristic, as evidenced by the shape and magnitude of these features. This clarifies the observed increases in photocurrent density and the efficiency of organic dye degradation.

Table 1 Elemental composition analysis results using the EDX technique on FTO and FTO/WO_3/$BiVO_4$ electrodes effect with laser-treatment and untreated on the FTO substrate.

Element	% Atomic			
	FTO		FTO/WO_3/$BiVO_4$	
	untreated	with laser- treatment	untreated	with laser- treatment
Si	1.76	2.84	1.32	1.30
Sn	31.58	30.50	26.57	27.14
W	-	-	2.50	1.99
Bi	-	-	0.99	1.33
V	-	-	1.09	0.97
O	66.67	66.67	67.53	67.27

Table 1 shows the % elemental composition of FTO and FTO/WO_3/$BiVO_4$ electrodes with laser treatment and untreated electrodes. The laser treatment caused the FTO substrates to have higher Si content (2.84%) compared to untreated substrates (1.76%) indicating a higher surface roughness. On the other hand, the Sn content in laser- treated FTO (30.50%) was lower than that in untreated FTO (31.58%), which may suggest atomic redistribution. The laser treated FTO/WO_3/$BiVO_4$ electrodes had a higher Bi content of 1.33%, while the untreated samples had 0.99%. This indicates an improved $BiVO_4$ adhesion due to increased surface roughness. The tungsten content was slightly decreased in laser treated electrodes (1.99%) compared to untreated electrodes (2.50%). This indicates successful material incorporation on the new surface. Moreover, V content was slightly reduced in laser treated electrodes (0.97%) when compared to untreated electrodes (1.09%). With respect to the other samples, the oxygen content was consistent across all samples (~67%). This suggests that laser treatment did not significantly affect the oxidation state of the electrodes. These results imply that the laser treatment improves the uniformity of the WO_3 and $BiVO_4$ layer adherence and consequently the performance of the photoelectrodes.

X-ray diffraction (XRD) analysis, illustrated in Figure 4, verifies the phase composition of FTO/WO_3/$BiVO_4$ electrodes, encompassing both untreated and laser-treated variants. The diffraction peaks at 26.92°, 34.1°, 38.8°, and 52.0° are indicative of the tetragonal phase of SnO_2 in the FTO substrate. The WO_3 monoclinic phase is characterized by peaks at 23.6°, 24.44°, and 34.1°, whereas the $BiVO_4$ monoclinic phase is validated by diffraction peaks at 18.8°, 28.9°, and 30.6°. Laser-treated samples had sharper and more pronounced $BiVO_4$ peaks, signifying enhanced crystallinity and phase uniformity. This improvement is essential for eliminating defects and facilitating efficient charge transfer, hence decreasing recombination losses and optimizing photoelectrocatalytic efficacy.

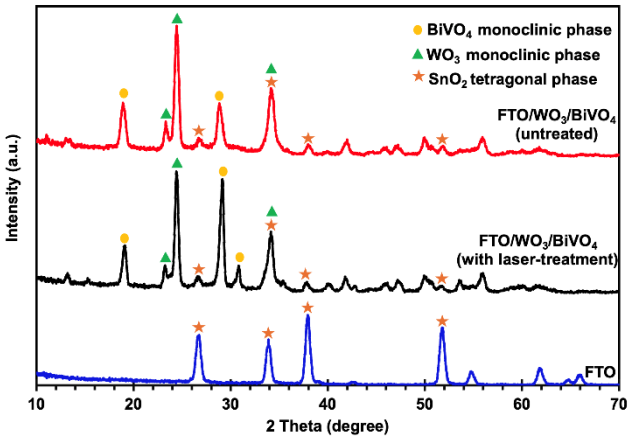

Figure 4 The X-ray diffraction patterns of FTO substrate and FTO/WO_3/$BiVO_4$ electrodes, consequently treated with laser processing and untreated.

4.2 Optical characteristics

Figure 5 shows the optical properties of the FTO/WO_3/$BiVO_4$ electrodes, with a focus on the effect of laser treatment on the FTO substrate. The laser-treated electrodes absorbed more visible light (Figure 5A). Because of the laser-induced surface roughness, the WO_3 and $BiVO_4$ layers adhere more strongly, resulting in a uniform coating [12]. Figure 5B shows the relationship between absorbance coefficient and energy band gap (E_g). The E_g of laser-treated electrodes was 1.8 eV less than that of untreated samples. The reduced energy gap improves visible light absorption in photoelectrocatalytic applications. The optimum light harvesting on the

DOI: 10.60101/jarst.2024.260565

JOURNAL OF APPLIED RESEARCH ON SCIENCE AND TECHNOLOGY

electrode surface is accomplished through a uniform semiconductor coating on laser-treated substrates, which minimizes light reflection and eradicates interlayer gaps. The findings indicate that laser treatment enhances the optical properties of FTO/WO_3/$BiVO_4$ electrodes, demonstrating their potential for improving photoelectrocatalytic efficiency.

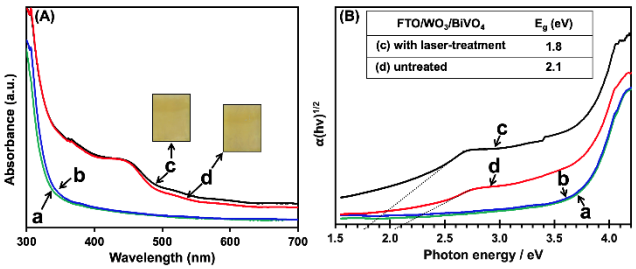

Figure 5 (A) Absorbance spectra (B) the correlation between the absorption coefficient and energy band with effects laser treatment; (a) FTO (with laser-treatment), (b) FTO (untreated), (c) FTO/WO_3/$BiVO_4$ (with laser-treatment), and (d) FTO/WO_3/$BiVO_4$ (untreated).

In addition, the laser-treated electrodes demonstrate increased visible light absorption (Figure 5A) attributed to light scattering from surface roughness and higher semiconductor adherence, leading to a more uniform coating that reduces reflection and interlayer gaps. The lowering of the band gap from 2.1 eV (untreated) to 1.8 eV (laser-treated) (Figure 4B) is ascribed to structural and electronic alterations caused by laser irradiation. Band gap tuning can be accomplished through doping or alloying; however, structural alterations and defect states can also reduce the band gap, thereby improving visible light absorption and photoelectrocatalytic performance. These findings confirm that laser treatment enhances semiconductor interfacial contact and charge transport, offering it as an attractive option for enhancing PEC performance.

4.3 Photoelectrocatalytic activity

Figure 6 shows the photoelectrocatalytic effectiveness of FTO/WO_3/$BiVO_4$ electrodes in a 0.1 M Na_2SO_4 solution at a potential of 1.0 V under visible light. Laser-treated FTO/WO_3/$BiVO_4$ electrodes showed enhanced photoelectrocatalytic performance, generating a current density of 5.5 mA/cm^2, in contrast to untreated electrodes, which provided 3.2 mA/cm^2. Laser-induced roughness on the FTO base made it easier for the WO_3 and $BiVO_4$ layers to bond together, increased the contact surface area, and let more solution through [13]. This modification made the oxidation reaction much more effective, demonstrating the advantageous effects of laser treatment before using the automatic dip-coating method to immobilize semiconductors.

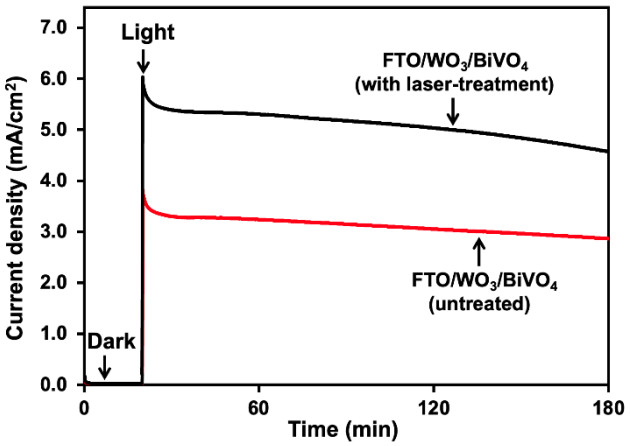

Figure 6 Amperograms display the comparative results of the oxidation reaction current values in the aqueous solution of FTO/WO_3/$BiVO_4$ electrodes, highlighting the impact of laser treatment on the FTO substrate.

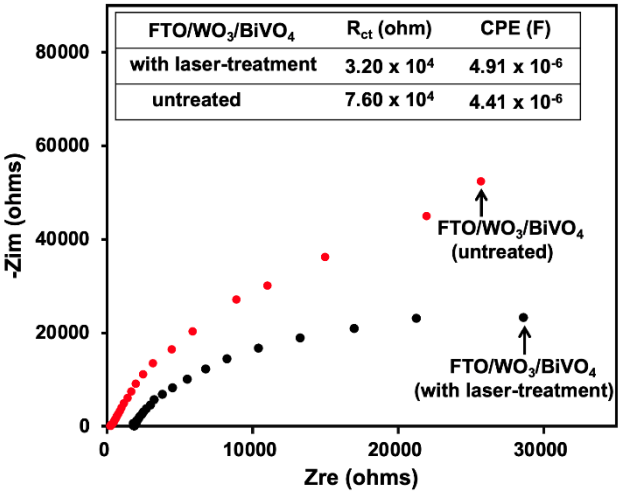

Figure 7 Nyquist plots of FTO/WO_3/$BiVO_4$ electrodes: comparison of with laser-treatment and untreated FTO substrates with inset of charge transfer resistance (R_{ct}) and constant phase element (CPE).

4.4 Electrochemical resistance and capacitance properties

Figure 7 demonstrates the electron transport characteristics between the electrode surface and the electrolyte, as a result of the electrochemical impedance spectroscopy (EIS) investigation of FTO/WO_3/$BiVO_4$ electrodes. The electron transfer efficiency in water oxidation reactions is improved by laser-treated FTO/WO_3/$BiVO_4$ electrodes, which have the smallest semicircle radius in the Nyquist plot. This represents a low charge transfer resistance (R_{ct}) and negligible electron transfer resistance. These results are consistent with the current density values depicted in Figure 6. Furthermore, the inset table illustrates that laser-treated electrodes have a higher constant phase element (CPE) value (4.91 x 10^{-6} F), which suggesting that the surface is more porous and rugged. This increases the surface area of the

DOI: 10.60101/jarst.2024.260565

electrode and its ability to maintain charge, as demonstrated in Figure 2 by SEM. The results show that laser treatment proceeds prior to the immobilization of WO_3 and $BiVO_4$, resulting in the development of thin coatings with improved electron transfer efficiency during water oxidation at the interfacial electrode/electrolyte.

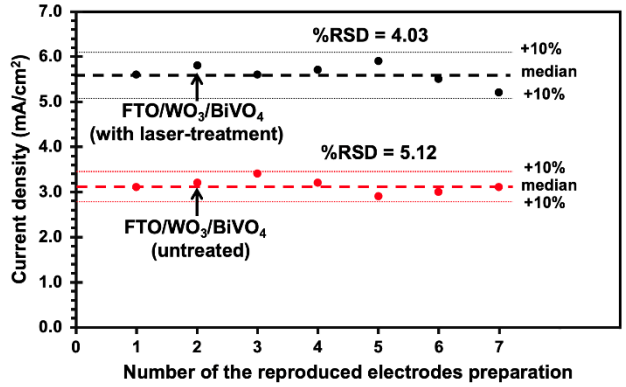

Figure 8 Comparison of photocurrent from water oxidation: reproducibility of FTO/WO_3/$BiVO_4$ electrodes with laser- treatment and untreated.

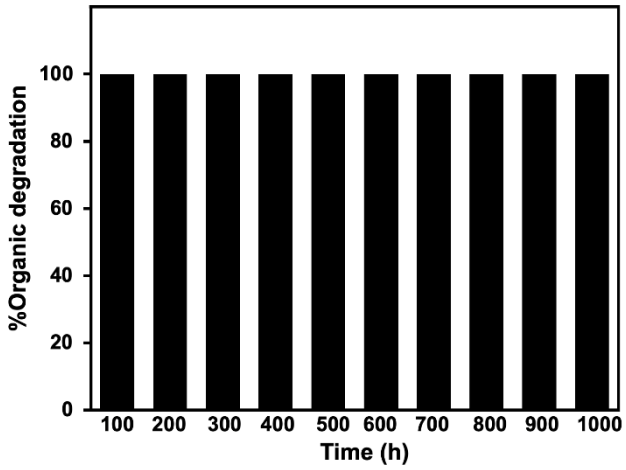

Figure 9 Durability of laser-treated FTO/WO_3/$BiVO_4$ photoanode for orange red dye removal via photoelectrocatalytic process.

4.5 The reproducibility performance

Figure 8 demonstrates the repeatability investigation of FTO/WO_3/$BiVO_4$ photoanode fabrication, emphasizing the impact of laser treatment on the FTO substrate prior to automated dipping in WO_3 and $BiVO_4$ solutions. Seven electrodes were produced under comparable settings to test consistency. The investigation found that laser-treated FTO/WO_3/$BiVO_4$ electrodes had higher photocurrent density than untreated electrodes, with a %RSD of less than 5%, indicating high reproducibility. Laser-induced porosity and homogeneous areas reduce variability, improving electrode production uniformity. The uniform features of the electrodes are provided by the improved adhesion of the coating solution, resulting in a homogeneous surface structure [14]. The findings indicate that the uniformity of the electrode production process is significantly improved by the laser treatment of FTO substrates before semiconductor immobilization.

4.6 The durability performance

Figure 9 demonstrates the durability of the FTO/WO_3/$BiVO_4$ photoanode, fabricated by laser treatment of the FTO substrate before semiconductor immobilization. The electrodes were utilized to decompose organic dye by applying the bias potential and subjecting them to visible light for 1,000 hours. The laser-treated electrodes maintained 100% removal efficiency throughout testing, demonstrating no performance loss. Laser-treated FTO/WO_3/$BiVO_4$ electrodes degrade organic dyes by photoelectrocatalytic reactions, resulting in a longer operational lifetime [15]. Figure 10 illustrates the schematic representation of the fabrication of the laser-treated FTO/WO_3/$BiVO_4$ photoanode, highlighting enhancements in surface roughness, charge storage capacity, and photoelectrocatalytic performance. Laser-treated FTO/WO_3/$BiVO_4$ photoanodes enable scalable wastewater treatment and sustainable energy applications, according to this study. The findings support further research on laser-assisted fabrication of improved photoelectrocatalytic materials.

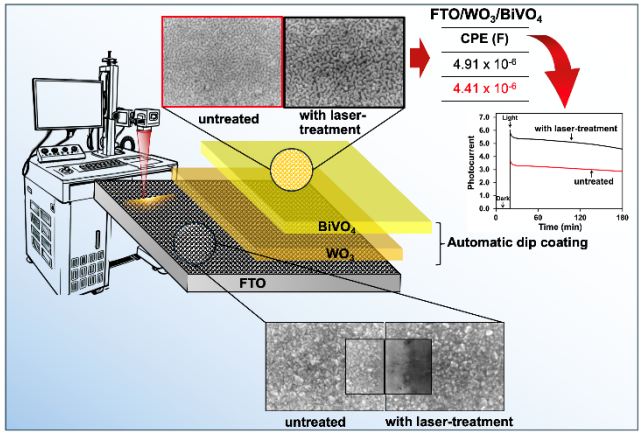

Figure 10 Schematic diagram of laser-treated FTO/WO_3/$BiVO_4$ photoanode fabrication.

This study describes an alternative way for increasing the efficiency and durability of FTO/WO_3/$BiVO_4$ photoanodes used in photoelectrocatalytic applications such as water oxidation and organic dye degradation. Several experimental assessments show that applying laser treatment to FTO substrates prior to semiconductor deposition improves electrode properties significantly. The laser-treated electrodes have a rough surface that enhances the adherence and homogeneity of WO_3 and $BiVO_4$ layers, improving their structural and functional properties. The fabrication process affects the performance of photoanode photoelectrocatalytic (PEC) technology. The laser-assisted FTO/WO_3/$BiVO_4$ photoanode exceeded alternative techniques, attaining a photocurrent density of 5,500 µA/cm² at 1.00 V vs. Ag/AgCl, and 100% degradation

DOI: 10.60101/jarst.2024.260565

of methylene blue (MB) within 40 minutes (Table 2). Laser-induced surface structures promote charge separation, enhance light absorption, and maintain electrochemical stability. In contrast, the normal dip coating exhibited a decreased current density (250 μA/cm²) and needed 180 minutes to remove 94% of the MB, signifying ineffective charge redistribution. The spin coating technique exhibited slight photocurrents (1,500-2,243 μA/cm²) and degradation rates (61% for coumarin, 98% for MB) under all conditions. These improvements demonstrate that the characteristics of electrolytes and contaminants substantially affect the effectiveness of PEC. The hydrothermal approach ($FTO/CdS/TiO_2$) had the lowest current density (84.25 μA/cm²) and the moderate degradation of methylene blue (82% in 180 minutes), indicating insufficient charge transport. Laser-assisted $FTO/WO_3/BiVO_4$ fabrication improves conventional methods in photoelectrochemical efficiency, durability, and organic dye degradation.

Table 2 Comparison of current densities and organic degradation efficiency for photoanodes by different fabrication methods.

Materials	Fabrication method	Electrolyte solution / Light source	Current density	Pollutants / Electrolyte / Degradation efficiency	References
$FTO/WO_3/BiVO_4$	Laser treatment combined Automatic dipping machine	0.1M Na_2SO_4 / 14.4-Watt light-emitting diode (LED)	5,500 μA/cm^{-2} at 1.00 V vs Ag/AgCl	5 ppm MB / 0.5M NaCl / 100% for 40 min	This work
$FTO/WO_3/BiVO_4$	Dip coating	0.1M Na_2SO_4 / 20-watt visible light irradiation	250 μA/cm^{-2} at 1.00 V vs Ag/AgCl	5 ppm MB / 0.1M Na_2SO_4 / 94% for 180 min	[16]
$FTO/WO_3/BiVO_4$	Spin coating	0.5M NaCl / 320-watt light source	1,500 μA/cm^{-2} at 1.23 V vs RHE	coumarin / 0.5M NaCl / 61% for 90 min	[17]
$FTO/WO_3/BiVO_4$	Spin coating	0.1M Na_2SO_4 / 300-watt light source	2,243 μA/cm^{-2} at 1.28 V vs RHE	10 ppm MB / 0.1M Na_2SO_4 / 98% for 180 min	[18]
$FTO/CdS/TiO_2$	Hydrothermal	0.1M NaCl / 300-Watt Xe arc lamp irradiation	84.25 μA/cm^{-2} at 1.0 V vs Ag/AgCl	5 ppm MB / 0.1M NaCl / 82% for 180 min	[19]

CONCLUSIONS

This research demonstrates that laser-treated $FTO/WO_3/BiVO_4$ photoanodes exhibit outstanding performance in degrading organic dyes compared to conventional production techniques. The laser method increased the roughness of the substrate, enhancing semiconductor adhesion and promoting structural uniformity. The developed $FTO/WO_3/BiVO_4$ photoanode exhibited a narrower energy band gap (1.8 eV), increased photocurrent density (5.5 mA/cm² at 1.0 V in 0.1 M Na_2SO_4), and reduced charge transfer resistance. Robustness studies demonstrated complete dye removal efficacy for 1,000 hours without performance loss, highlighting the durability and scalability of the modified electrodes for practical applications. These findings emphasize the promise of laser-treated $FTO/WO_3/BiVO_4$ photoanodes for wastewater treatment and renewable energy production applications. Future research may concentrate on refining laser settings for other materials and broadening applications to various photoelectrocatalytic processes.

ACKNOWLEDGEMENT

This research received funding from the Research and Researchers for Industries (RRI) project and Eagle Dream Co., Ltd. (N41A650408).

REFERENCES

1. Zeng Q, Lyu L, Gao Y, Chang S, Hu C. A self-sustaining monolithic photoelectrocatalytic/photovoltaic system based on a $WO_3/BiVO_4$ photoanode and Si PVC for efficiently producing clean energy from refractory organics degradation. Appl Catal B: Environ. 2018;238:309-17.
2. Liu J, Zhang S, Wang W, Zhang H. Photoelectrocatalytic principles for meaningfully studying photocatalyst properties and photocatalysis processes: From

DOI: 10.60101/jarst.2024.260565

fundamental theory to environmental applications. J Energy Chem. 2023;86:84-117.

3. Potipat J, Somnuek C, Mekprayoon S. Water pollution influencing contamination of Vibrio bacteria in the coastal aquaculture area of Chanthaburi and Trat Provinces. J Appl Res Sci Tech [internet]. 2024;23(3):255295. Available from: https://doi.org/10.60101/jarst.2023.255295.

4. Kangkun N, Ponchio C. Photoelectrodeposition of $BiVO_4$ layer on FTO/WO_3 photoanodes for highly efficient photoelectrocatalytic chemical oxygen demand sensor applications. Appl Surf Sci. 2020;526:146686.

5. Wei P, Wen Y, Lin K, Li X. 2D/3D WO_3/$BiVO_4$ heterostructures for efficient photoelectrocatalytic water splitting. Int J Hydrog Energy. 2021;46(54): 27506-15.

6. Uttayanil T, Ponchio C. WO_3/Bi_2WO_6 photoanode enhancement for photoelectrocatalytic water oxidation; scan rate effect optimization in the cyclic voltammetry deposition method. J Appl Res Sci Tech [internet]. 2023;23(1):253891. Available from: https://doi.org/10.60101/jarst.2023.253891.

7. Nareejun W, Ponchio C. Novel photoelectrocatalytic/ solar cell improvement for organic dye degradation based on simple dip coating WO_3/$BiVO_4$ photoanode electrode. Sol Energy Mater Sol Cells. 2020;212: 110556.

8. Du X, Ning X. Heteroepitaxial growth of PMN-PT thin films on $SrTiO_3$ buffered III-V semiconductor GaAs by pulsed laser deposition. J Cryst Growth. 2025;653:128070.

9. Lamichhane S, Tomar M, Chowdhuri A, Sharma S. Role of laser energy variation on energy storage capacity of bilayer BFO/WO_3 thin film structure. Mater Sci Semicond Process. 2025;188:109218.

10. Hacini A, Ali AH, Harkat L, Nayan N, Adnan NN, Azali MM, et al. Effect of laser fluence on the ITO/ Mo-Ag/ITO multilayer thin film for a-Si(n)/c-Si(p)/ a-Si(p)/Al heterojunction solar cells. Sol Energy. 2024;284:113042.

11. Rodríguez-Rosales K, Cruz-Gómez J, Santos Cruz J, Guillén-Cervantes A, de Moure-Flores F, Villagrán-Muniz M. Plasma emission spectroscopy for studying Bi_2S_3 produced by pulsed laser deposition and effects of substrate temperature on structural, morphological, and optical properties of thin films. Mater Sci Eng B 2025;312:117867.

12. Majumder M, Batista-Pessoa W, Bottin N, Constantinescu C, Koudia M, Petroni E, et al. Optically inducing and probing the local crystallization of ultra-thin GeSbTe films by single-pulse laser irradiations. Surf Interfaces. 2025;56:105664.

13. Divya J, Shivaramu NJ, Swart HC. Structural and optical characteristics of α-Bi_2O_3/ $Bi_2O(3\text{-}x)$:HO^{3+} thin films deposited by pulsed laser deposition for improved green and near-infrared emissions and photocatalytic activity. Heliyon. 2024;10(1): e23200.

14. Mishra G, Tiwari A. Pulsed laser deposition of Nd-doped $BaSnO_3$ thin films on c-plane sapphire substrate for transparent sensors. Mater Sci Eng B. 2024;310:117768.

15. Velmurugan R, Aishwarya M, Balamurugan K, Nivedha K, Subramanian B. Influencing In situ tuned nanostructures of pulsed laser ablated Co_3O_4 & WO_3 thin film electrodes for binder free flexible operando hybrid supercapacitor devices. Electrochim Acta. 2022;419:140371.

16. Nareejun W, Ponchio C. Novel photoelectrocatalytic/ solar cell improvement for organic dye degradation based on simple dip coating WO_3/$BiVO_4$ photoanode electrode. Sol Energy Mater Sol Cells. 2020;212:110556.

17. Zeng Q, Lyu L, Gao Y, Chang S, Hu C. A self-sustaining monolithic photoelectrocatalytic/ photovoltaic system based on a WO_3/$BiVO_4$ photoanode and Si PVC for efficiently producing clean energy from refractory organics degradation. Appl Catal B: Environ. 2018;238:309-17.

18. Zeng Q, Lyu L, Gao Y, Chang S, Hu C. A self-sustaining monolithic photoelectrocatalytic/ photovoltaic system based on a WO_3/$BiVO_4$ photoanode and Si PVC for efficiently producing clean energy from refractory organics degradation. Appl Catal B: Environ. 2018;238: 309-17.

19. Wu Y-H, Wu T, Lin Y-W. Photoelectrocatalytic degradation of methylene blue on cadmium sulfide-sensitized titanium dioxide film. Mater. Res. Bull. 2019;118:110500.

Received: January 28, 2025 | Revised: February 12, 2025 | Accepted: February 14, 2025

JOURNAL OF APPLIED RESEARCH ON SCIENCE AND TECHNOLOGY
JARST
INSTITUTE OF RESEARCH AND DEVELOPMENT
RAJAMANGALA UNIVERSITY OF TECHNOLOGY THANYABURI
ISSN ONLINE: 2773-9473
https://ph01.tci-thaijo.org/index.php/rmutt-journal

A predictive model for highly efficient helicopter maintenance in the Royal Thai Air Force using deep learning

Somkait Hoonsakul*, Prasong Praneetpolgrang and Payap Sirinam

Graduate School, Navaminda Kasatriyadhiraj Royal Thai Air Force, Saraburi 18180, THAILAND
*Corresponding author: Som.hoonsakul@gmail.com

ABSTRACT

The Royal Thai Air Force has helicopters in service to support tactical transport missions. Over time, helicopters deteriorate, making maintenance essential to maintain mission capabilities. Regular and timely maintenance helps to maintain operational readiness and safety, reduces the risks associated with unexpected failures, and ensures the continuous availability of critical resources. In this research, the ultimate goal is to use the results of this research as a guideline for improving the Royal Thai Air Force's helicopter maintenance plans to be good and efficient, where efficient maintenance planning can significantly reduce costs and enhance safety. This research provides valuable insights for academia and aviation industry professionals. The researcher has proposed a model to predict helicopter maintenance in the Royal Thai Air Force to improve maintenance efficiency and increase the accuracy of spare parts calculations. Using a helicopter maintenance dataset from January 2017 to September 2020, a total of 3,819 datasets covering a variety of maintenance scenarios and operating conditions, the researchers applied deep learning (DL) techniques to make predictions. The algorithms used in this research include fully connected neural networks (FCNN), long-term short-term memory (LSTM), and convolutional neural networks (CNN). FCNN is suitable for general numerical data that are not related in sequence or space, making it effective for linear or simple numerical datasets. On the other hand, LSTM is ideal for analyzing time-sequence data because it can capture past trends to predict future outcomes. CNN excels in handling spatially correlated data, especially those related to helicopter maintenance patterns that require analyzing multiple related factors. The results show that FCNN achieves an accuracy and precision of 1.00, while both LSTM and CNN achieve an accuracy and precision of 0.94. The results of this study clearly highlight the potential of DL-based models to improve prediction accuracy. However, the study's limitations may lie in the accuracy of deep learning model in predicting the Royal Thai Air Force's helicopter maintenance. The future direction could be to develop more accurate predictive maintenance guidelines for the Royal Thai Air Force's helicopters. The specific research gap this study, by improving deep learning algorithms and collecting more diverse data from the Royal Thai Air Force's helicopters maintenance, resulting in increased accuracy. To use the results of this research as a guideline for improving The Royal Thai Air Force's helicopter maintenance plans to be good and efficient. This will indirectly result in reducing the helicopter maintenance budget of the Royal Thai Air Force and increasing the reliability of the operations of the Royal Thai Air Force.

Keywords: Predictive maintenance, Helicopter, Deep learning

INTRODUCTION

Application of deep learning techniques for helicopter maintenance [1-2] of the Royal Thai Air Force. Helicopters are essential aircraft for tactical transport and public rescue missions. Due to the long service lifetime of helicopters in the Royal Thai Air Force, maintenance is crucial to maintain operational capability.

Research indicates that maintenance personnel are the most important factor, they must have comprehensive knowledge, experience, and certification. However, most experienced technicians are nearing retirement age. In addition, helicopters are composed of many parts with varying service life, while the Royal Thai Air Force operates under a limited maintenance budget.

Currently, the government lacks comprehensive support for the aircraft maintenance industry, including production, operation, and improvement. This gap extends to capital management, infrastructure, and competitiveness development. The use of artificial intelligence as a management and decision-support tool is a practical solution.

This research explores the use of deep learning to predict helicopter maintenance needs [3-4] using datasets from spare parts requests, flight records,

DOI: 10.60101/jarst.2024.260451

maintenance schedules, instrument calibration history, and expert technician level to develop the accurate predictive models. Policy development should focus on aligning Thailand's aircraft maintenance standards with international standards (ICAO, EASA, and FAA); while developing specific regulations and enhancing personnel capabilities. This approach aims to make Thailand a regional maintenance hub, enhance national security, and reduce dependence on foreign technologies through sustainable development.

MATERIALS AND METHODS

This research presents a literature review on the application of deep learning techniques in predictive maintenance, covering models such as FCNN, LSTM, and CNNs, as well as case studies in various industries such as aviation and manufacturing.

Deep learning is a part of machine learning, which is an algorithm used for learning that can enable machines to make decisions like humans. Machine learning is the application of statistical knowledge to analyze data and create models to predict the results from the data.

The starting point of deep learning is the artificial neural network, which is an algorithm invented by imitating the functionals of the human brain. The human brain has complex functions and can analyze a large number of things efficiently. Artificial neural networks simulate the functioning of neurons, each of which has connections to send information to each other for decision-making. The highlight of the human brain is that each neuron can be connected thoroughly and has a clear distribution of data analysis for each cell [5].

Artificial neural networks are designed to work similarly to the human brain. Behind the scenes of an artificial neural network, some subunits work similar to human neurons called nodes. Each node can be combined into several layers called layers. Each node has a working process divided according to the function of each layer, such as Input Layer, Hidden Layer, and Output Layer, as shown in Figure 1.

From Figure 1, the operation of Nodes is based on both Linear Regression and can be represented as in Equation (1). Each Node has small components called Weight, which is comparable to the Intercept value from Linear Regression. It is used to determine the weight of each variable used in the analysis and Bias, which is comparable to the Coefficient in Linear Regression, which compares Node to the work of Linear Regression. In the training process, training will be done to find parameter values that are appropriate to the data used for used prediction. Then the obtained parameters are used to build a model for use in predicting results by training. The Neural Network must be trained in rounds. In one round, it must be trained with every data used for coach in 1 round, it must be trained with all data used for training, which is called the number of rounds in training called Epoch.

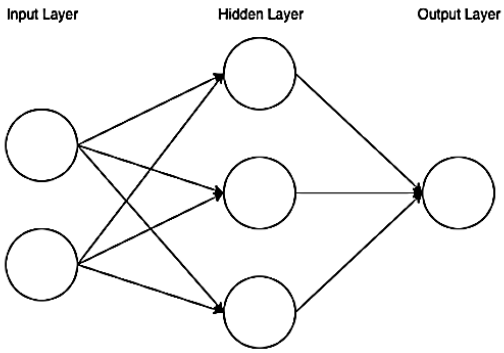

Figure 1 The structure of an artificial neural network has a sub-computing part called a Node and the arrangement of each Node in layers called Layer.

$$Neural\ Network\ (m,n) = activation\ (W_{mn} i_n + b_m) \quad (1)$$

Where

Neural Network (m,n) = Represents the results of the neural network topology model.
Activation = Represents the function used to convert the values obtained from the calculation of the weights of the neural network structure.
Mn^i = Represents the weights of nodes in the neural network structure.
N = Represents the input value of the artificial neural network structure.
B_m = Represents the bias of the neural network structure.

There are many types of artificial neural networks, which can be divided by the training process. Examples of popular types of artificial neural network structures include feedforward neural network, which feeds data from the front to the back, such as perception, etc., and backpropagation neural networks, which feed data and learn by feeding the results in reverse. Deep learning is one of the algorithms that is developed from artificial neural networks, which imitates the learning of the human nervous system. It is developed by laying down a structure in the form of stacking many layers, both in the form of stacking in the form of the same type in every layer and in the form of stacking in each layer, which works differently. It is caused by applying the capabilities of each structure used together to increase the efficiency of analysis [6].

Deep learning is currently providing better analysis and prediction efficiency than the use of traditional machine learning algorithms. Both in terms of the amount of data that has increased dramatically and the more efficient computer processors, deep learning can use a large number of variables in analysis to increase the efficiency of analysis. In addition to

DOI: 10.60101/jarst.2024.260451

JOURNAL OF APPLIED RESEARCH ON SCIENCE AND TECHNOLOGY

increasing the number of layers, deep learning has adjusted the learning ability of the algorithm by taking learning as Backpropagation is improved by separating the learning algorithm into 2 functions: Loss Function and Optimize Function. The Loss Function is used to calculate the error value obtained by comparing the results from the model and the results from training. Then, the resulting Loss value is used with the Optimize Function, which is a function for adjusting the parameters used in learning the created model. There are various Loss Functions and Optimize Functions available for use today. Currently, deep learning has invented various algorithms and structures to respond to the needs of various forms of analysis. The currently popular algorithms are as follows:

Fully Connected Neural Networks (FCNN) or Dense Neural Networks (DNN), Long Short-Term Memory (LSTM) Convolutional Neural Networks (CNNs), etc. The increasing popularity of deep learning is due to the higher analysis efficiency and the rapid development of hardware technology, both high-performance processors and the application of a Graphic Processing Unit (GPU) in deep learning, which can process faster than the Central Processing Unit (CPU) because the GPU processes in the form of Matrix Parallels, while the CPU processes in the form of Serial. [7] Fully Connected Neural Network (FCNN) or Dense Neural Network is the simplest implementation of deep learning algorithms. It is an extension of the neural network by adding several layers, resulting in more variables for feature extraction. To increase the efficiency in analysis and prediction [8], the operation of the structure is similar to the artificial neural network, as shown in Figure 2.

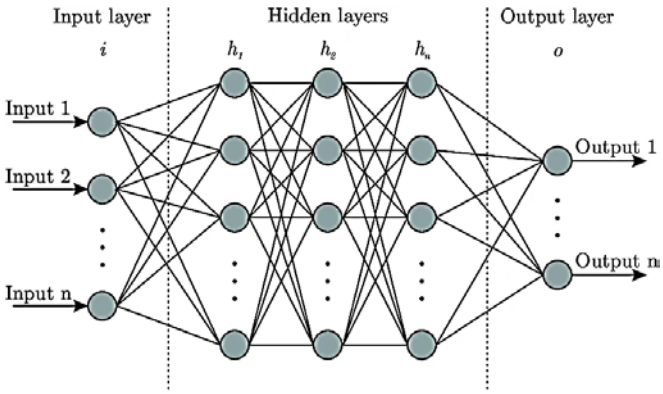

Figure 2 Example structure of the Fully Connected Neural Network (FCNN) algorithm.

Fully Connected Neural Network (FCNN) or Dense Neural Network has the most similar function and structure to artificial neural networks, but has added more layers for analyzing data features. The larger number allows for a more detailed analysis of features and training using the principle of Backpropagation in training.

Fully Connected Neural Network (FCNN) or Dense Neural Network has been used to analyze data in a structured form. In analyzing FCNN or DNN data, the analysis is performed without destroying the original data, allowing for accurate and highly efficient analysis.

Fully Connected Neural Network (FCNN) [9-11] is one of the most important technologies in the world of AI, especially in Deep Learning. The highlight of FCNN is the completed connection between neurons in each layer. That is, neurons in one layer can be completely connected to all neurons in the next layer. This connection allows FCNN to process a wide range of data, covering everything from basic and easy-to-understand data to complex data that requires multidimensional analysis. FCNN works from the input layer, which is the first layer that receives raw data into the system, such as numerical data, statistics, or data related to equipment maintenance. This data is then passed to the hidden layers, which are the core of FCNN. These layers transform the data into a format that the system can easily process. There may be many hidden layers, and each layer contains many processing units.

The more layers or processing units there are, the more complex the system can learn and capture. However, adding hidden layers or the number of processing units in each layer must be done carefully. If the system is too complex, it may lead to overfitting, which means that the system learns too well from the sample data and cannot be used to learn new data effectively. Once the data has passed through all the hidden layers, this data is then forwarded to the Output Layer, which is the final layer of the system. This layer is responsible for combining all the results from the previous layers and converting the results into a format that meets the desired goals, such as data classification or outcome prediction. For example, in the helicopter maintenance analysis, FCNN is used to classify the status of equipment into three categories: equipment that cannot be repaired, equipment that can be repaired but is not worth it, and equipment that can be repaired but is worth investing in. What makes FCNN outstanding and interesting is its flexibility. The system can design hidden layers that are appropriate for each type of data. For example, for data that does not have a clear pattern or structure, FCNN can help find patterns or relationships in the data that may not be obvious at first. This makes FCNN an important tool in analyzing numerical data, such as sales forecasts, financial risk assessments, or analysis of various factors in the industry [12-15].

Long Short-Term Memory (LSTM) is an algorithm that is developed from RNN by solving the problem of Gradient Vanishing by designing a new Cell that can store the state of the computation [16]. In the Cell of LSTM, there is a sub-computation unit called a Gate, which consists of an input Gate, Forget Gate,

DOI: 10.60101/jarst.2024.260451

JOURNAL OF APPLIED RESEARCH ON SCIENCE AND TECHNOLOGY

Memory Cell State Gate, and Output Gate as shown in Figure 3.

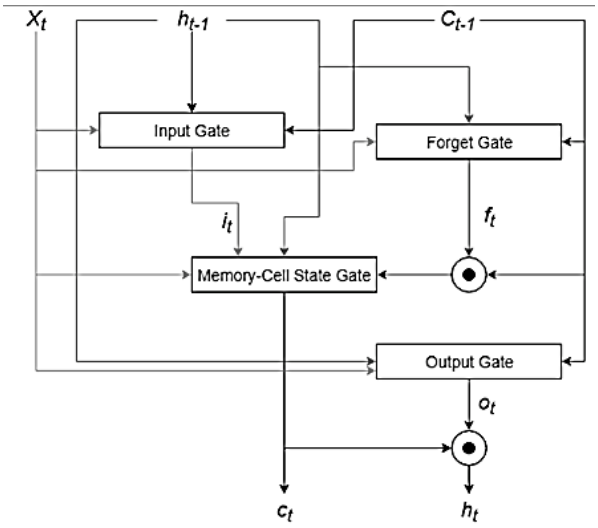

Figure 3 Example of working in a cell of the LSTM neural network algorithm.

Input Gate is a sub-unit to determine the data to be analyzed in Cell by receiving data to write values into each Cell as in Equation (2) [17].

$$i_t = \sigma\left(W_{xi}x_t + W_{hi}h_{t-1} + W_{ci}c_{t-1} + b_i\right) \quad (2)$$

Where

i_t = represents the result obtained from the Input Gate.
σ = represents the Sigmoid function.
W_{xi} = represents the weight value for calculating the Input in the Input Gate.
x_t = represents the input value that is entered for calculation.
W_{hi} = represents the weight value for calculating the Hidden State in the Input Gate.
h_{t-1} = represents the Hidden State value obtained from the calculation in the previous time unit.
W_{ci} = represents the weight value for calculating the Memory Cell State in the Input Gate.
c_{t-1} = represents the Memory Cell State value obtained from the calculation in the previous time unit.
b_i = represents the Bias value used in the calculation of the Input Gate.

Forget Gate is a subunit used to determine the data to be analyzed in Cell by determining whether the data should be recorded or forgotten, it can be defined as Equation (3) [17].

$$f_t = \sigma\left(W_{xf}x_t + W_{hf}h_{t-1} + W_{cf}c_{t-1} + b_f\right) \quad (3)$$

where

f_t = represents the result obtained from Forgot Gate.
σ = represents the Sigmoid function.
W_{xf} = represents the weight value for calculating the Input in Forgot Gate.
x_t = represents the input value that is entered for calculation.
W_{hf} = represents the weight value for calculating the Hidden State in Forgot Gate.
h_{t-1} = represents the Hidden State value obtained from the calculation in the previous time unit.
W_{cf} = represents the weight value for calculating the Memory Cell State in Forgot Gate.
c_{t-1} = represents the Memory Cell State value obtained from the calculation in the previous time unit.
b_f = represents the Bias value used in the calculation in Forgot Gate.

Memory Cell State Gate is a sub-unit to define the data that is entered for analysis in the Cell and calculating the state value to be used in the next calculation, with equation (4) [17].

$$c_t = f_t \cdot c_{t-1} + i_t \cdot tanh\left(W_{xc}x_t + W_{hc}h_{t-1} + b_c\right) \quad (4)$$

where

C_t = represents the Memory Cell State in the time interval.
f_t = represents the result obtained from Forget Gate.
c_{t-1} = represents the Memory Cell State from the previous time interval.
i_t = represents the result obtained from the Input Gate.
$tanh$ = represents the Hyperbolic tangent function.
W_{xc} = represents the weight for calculating the Input from the Memory Cell State Gate.
x_t = represents the Input value that is entered into the calculation.
W_{hc} = represents the weight for calculating the Hidden State in Memory Cell State Gate.
h_{t-1} = represents the Hidden State obtained from the calculation in the previous time interval.
b_c = represents the Bias value used in the calculation in Forgot Gate.

The Output Gate is a sub-unit for calculating the Output of the Cell, which has two results: Output and Hidden State for use in the next calculation, with equations as Equations (5) and (6) respectively [17].

$$o_t = \sigma\left(W_{xo}x_t + W_{ho}h_{t-1} + W_{co}c_{t-1} + b_o\right) \quad (5)$$

$$h_t = o_t \cdot \tanh(c_t) \quad (6)$$

DOI: 10.60101/jarst.2024.260451

where

o_t = represents the result obtained from the Output Gate.
σ = represents the Sigmoid function.
W_{xo} = represents the weight value for calculating the Input in the Output Gate.
x_t = represents the input value that is entered into the calculation.
W_{ho} = represents the weight value for calculating the Hidden State in the Output Gate.
h_{t-1} = represents the Hidden State value obtained from the calculation in the previous time unit.
W_{co} = represents the weight value for calculating the Memory Cell State in the Output Gate.
c_{t-1} = represents the Memory Cell State value obtained from the calculation in the previous time unit.
b_o = represents the Bias value used in the calculation of the Output Gate.
h_t = represents the Hidden State value from the calculation.

Convolutional Neural Networks (CNNs) [18-20] are an innovation that plays a major role in the world of artificial intelligence, especially deep learning, which is currently very popular. CNNs are designed to support the analysis of spatial data such as images, videos, audio, or data with physical structures, especially in tasks that require detecting patterns or relationships in the data that humans may not be able to see. The structure of CNNs makes them versatile tools that can systematically explore and transform raw data into insights. The process begins with a convolutional layer, which is the heart of CNNs. Small filters in this layer act like microscopes that scan the original data piece by piece, whether it is an image region, a specific outline, or a shape. Each filter has a specific role. Some filters look for image regions, some detect color intensity; or even small characteristics that are the basis of further analysis. Once the data has been scanned and has important features, it is passed to the dimensionality reduction layer, which compresses the data while preserving the important features of the data. This process allows the system to process faster and reduce unnecessary complexity. A popular example of dimensionality reduction is Max Pooling, which selects only the largest values in each subset of data. As with filtering the essence of the data, the data that passes through this layer is reduced in dimensionality; but still has clarity in important aspects.

Once the data has been processed and reduced in dimensionality, it enters a fully connected layer, which is like the center of all the data in the system. This layer is responsible for collecting the results from the previous steps and analyzing them to get the final answer, whether it is image classification, outcome prediction, or complex decision-making. This layer is responsible for connecting the scattered data to the big picture, allowing the system to make accurate decisions.

The highlight of CNNs is the ability to extract features hidden in the data efficiently without having to rely on manual feature design as in the past. This makes CNNs very flexible and can be used for specific tasks that require specific accuracy, such as diagnosing diseases from X-rays, interpreting languages from images, and detecting objects in videos, or for general tasks that require intelligent systems that can learn by themselves.

The great thing about CNNs is their ability to learn and understand data at a level that is more complex than humans can do in a short period, bringing our world closer to innovations such as self-driving cars, intelligent robots, or accurate and deep language translation systems.

In an era where data is becoming increasingly complex, CNNs are an ally in translating that complexity into simple, actionable answers. Here's why CNNs are a key part of driving the rapid advancement of AI.

Convolutional Neural Networks (CNNs) are deep learning algorithms that work similarly to human eye scanning by dividing the features into groups for analysis and using the newly obtained features to predict the results. CNNs are outstanding in Feature Extraction from data sets, focusing on finding features from data sets in the form of groups of data [21].

The CNN algorithm is divided into 2 parts: Feature Extraction and Classification. Feature Extraction is a work to select features for use in predicting the results in the Classification step, which is the next step for Feature Extraction of CNNs. It is the use of Filters to select Features by defining the size of the Filter used for data selection. This Filter is in the form of a Matrix, working by placing it on the data set to define the area used for analysis and processing, as shown in Figure 4.

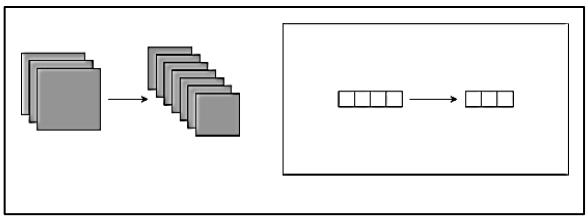

Figure 4 Example of working of CNNs algorithm.

From Figure 1, the CNN algorithm uses filters to create new feature sets. Once we have new features, we can reduce the size of the features and still maintain the identity of the original data without distortion. There are 2 algorithms to choose from: Max Pooling and Average Pooling. Max Pooling is creating another filter to use in data analysis. Then, the highest value

DOI: 10.60101/jarst.2024.260451

in the filter is extracted for use, as shown in Figure 4. Average Pooling creates a filter similar to Max Pooling, but it extracts the average of the values of the filter, as shown in Figures 5 and 6.

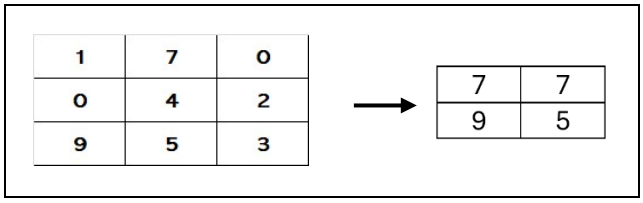

Figure 5 Data obtained from the Filter is passed through a 2x2 Max Pooling.

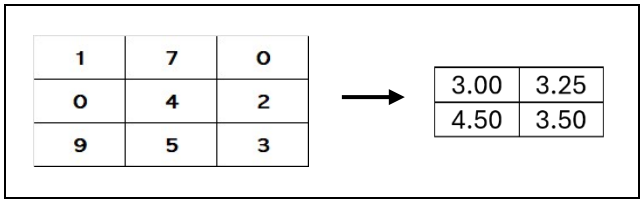

Figure 6 Data obtained from the filter is passed through a 2x2 Average Pooling.

This research uses three models to cover all data characteristics, where FCNN is suitable for basic data, LSTM is suitable for temporal data, and CNNs are suitable for spatial data. All of these make the development of the helicopter maintenance prediction model the most comprehensive and accurate. This research aims to develop and test deep learning models in various algorithms to predict helicopter maintenance of the Royal Thai Air Force. The research process consists of steps as shown in Figure 7.

From Figure 7, the research process starts with data collection. Then, the data is processed into a form suitable for model use, starting with the selection of important features [22-23] to create the necessary data framework for input into the model. Then, models are selected for testing, model construction, and training, model suitability is checked, and the performance of the prediction model is measured to obtain the most accurate and suitable model. For data collection, researchers collect various types of data, such as helicopter maintenance history, spare parts list, flight data, maintenance plans, history and calibration list of maintenance tools and equipment, and information about maintenance technicians who can repair helicopters. This data is made into a dataset for training a deep-learning model to help predict future helicopter maintenance trends. The details of each feature are shown in Table 1. Consider and analyze the prediction model. The researchers conducted further research on three more datasets. The remaining 80% is used to verify the diagnosis results. If the results are not good, a new fiber will be created. The new algorithm will optimize the internal structure of the prediction model before doing it again until the best prediction model is obtained. The remaining 20% of the data will be used to test and compare the three models.

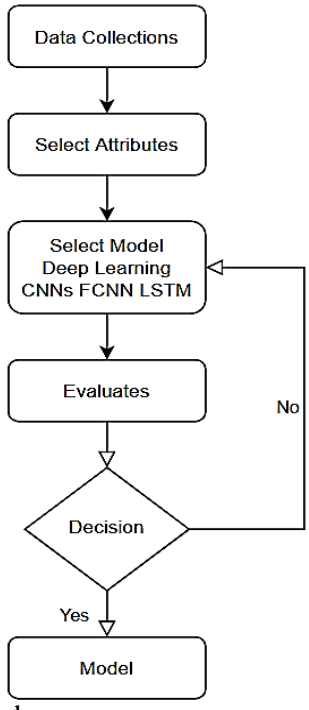

Figure 7 Research process.

Table 1 List of attributes and data attributes.

No.	Attribute	Data Property	Description
1	Car_Number	Discrete	Number of Aircraft/Helicopters.
2	Working_Status	Discrete	Maintenance status.
3	Skill_Level	Discrete	Technically skill level.
4	Years_Left	Discrete	The number of remaining years before a part or device expires.
5	Manual_Available	Discrete	Is there a manual for use?
6	Tool_Name	Discrete	Name of the tool used in the maintenance process.
7	Tool_Size	Discrete	Size of tools used.
8	Calibrated	Discrete	Instrument calibration status.
9	Operational	Discrete	Operational status of parts or equipment.

DOI: 10.60101/jarst.2024.260451

No.	Attribute	Data Property	Description
10	Part_Name	Discrete	The name of the part in use or under Maintenance.
11	Installation_Date	Discrete	Date of installation of the part.
12	Hours_Used	Discrete	Number of hours the part or equipment has been used.
13	Minutes_Used	Discrete	Number of usage times.
14	Expiration_Date	Discrete	The expiration date of the part or device.
15	Date_Now	Discrete	Current date.
16	leDay	Discrete	Forecast data
17	Management	Discrete	Situation management
18	statusMaintenance	Discrete	Maintenance situation

Data Collection The researchers collected data on helicopter maintenance history, spare parts list, helicopter flight data, helicopter maintenance plan, instrument calibration history, maintenance equipment calibration list, and helicopter mechanics who can perform helicopter maintenance. This data was used as the baseline data for creating a dataset used to train a deep learning prediction model, which enables the prediction of future helicopter maintenance trends. The details of each feature are shown in Table 1.

To measure the performance of the model in predicting helicopter maintenance with three outcomes (0, not repairable; 1, repairable but poor performance; 2, repairable and good performance), the researchers used a Confusion Matrix [24], which shows the number of correct and incorrect predictions in each category. The calculation Equations (7)-(10) are as follows:

$$\text{Accuracy} = \frac{(TP+TN)}{(TP+FP+TN+FN)} \quad (7)$$

$$\text{Precision} = \frac{TP}{(TP+FP)} \quad (8)$$

$$\text{Recall} = \frac{TP}{(TP+FN)} \quad (9)$$

$$\text{F1-Score} = \frac{(TP+TN)}{(TP+FP+TN+FN)} \quad (10)$$

Where TP = The predicted data is correct and the actual result is correct.
TN = The predicted data is incorrect and the actual result is incorrect.
FP = The predicted data is correct but the actual result is wrong.
FN = The predicted data is incorrect but the actual result is correct.

The selection of evaluation metrics in Accuracy, Precision, Recall, and F1-Score in this research is important because the nature of maintenance prediction problems involves imbalanced data and the consequences affect the success or failure of decision-making. For example, if the forecasting system fails to identify helicopters that need urgent maintenance, it may lead to safety risks. Therefore, it is necessary to consider metrics that not only measure general accuracy but also focus on the ability to handle unequally distributed data in the data set (Class Imbalance).

Precision and Recall are important metrics in this context because Precision measures the accuracy of the prediction in the group that the system indicates as "maintenance required", which reduces false positives that may lead to unnecessary maintenance. On the other hand, Recall helps assess the system's ability to find cases that are "really maintenance required", which is crucial to avoid false negatives. Neglecting a helicopter that needs maintenance may lead to system failure or mission risk. Using both Precision and Recall ensures that the system can fully meet these requirements.

The F1-Score is used to balance Precision and Recall, especially in cases of imbalanced data, for example, if the prediction is correct in a large group (e.g. maintenance-free helicopters) but fails in a small group (maintenance helicopters). Accuracy may look good, but it does not reflect the true performance of the system. The F1-Score provides a combined measure of Precision and Recall, without focusing on one or the other, allowing for a comprehensive evaluation of the system that is most suitable for the research goal of predicting maintenance accurately and efficiently.

RESULTS AND DISCUSSION

In this study, the researchers trained all the models for 50 iterations, dividing the prediction output into three types of inputs to examine the difference between the features added to the three prediction models to see how these features affect the accuracy of the prediction models. In the first case, the model input is determined based on SEM, with the input features being Working Status, Operational, leDay, and Management as shown Figure 8.

From the Heat Map Diagram, we can see the relationship between different variables. Related to equipment maintenance in the Air Maintenance Practice Dataset, for example, in the picture there is an interesting point: Skill Level and Years Left are negatively

DOI: 10.60101/jarst.2024.260451

JOURNAL OF APPLIED RESEARCH ON SCIENCE AND TECHNOLOGY

related (-0.96). This means that people with higher skills tend to have shorter careers. Moreover, the relationship between the number of hours used (Hours Used) and the length of time before maintenance (IeDay) have a value of 0.62, indicating that if the equipment is used more, it will be time for maintenance sooner. This information can help us predict and plan maintenance more accurately. Another interesting point is Management has a relationship with the duration of equipment use (IeDay), a correlation value of 0.62, this means that good management can help control and extend the life of your equipment. Meanwhile, Management and Status Maintenance have a negative correlation (-0.36), indicating that good management may help reduce the frequency of maintenance. This information can be used to improve planning and increase the efficiency of maintenance systems. Helps reduce costs and increase equipment availability for use.

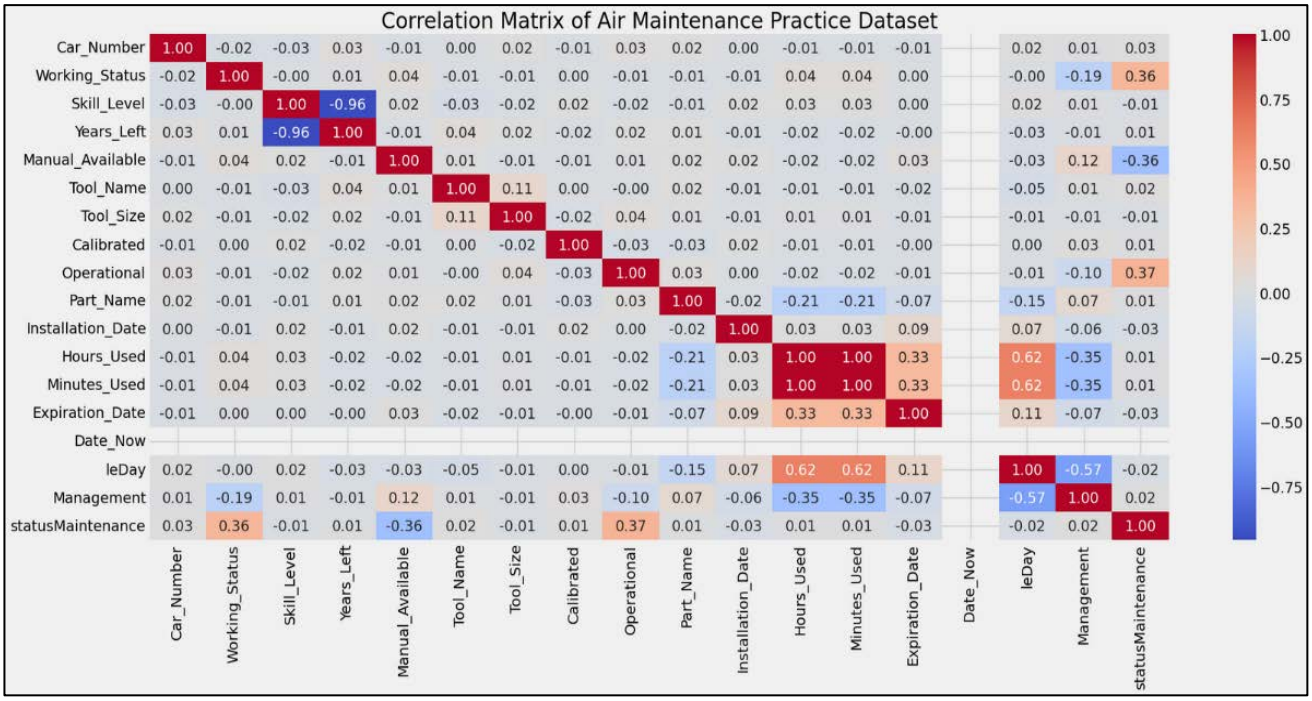

Figure 8 Heat Map diagram shows the relationship of each attribute.

Table 2 Hyperparameters, or values that are set before training the model without being learned by the model itself.

Algorithm	Learning Rate	Batch Size	Number of Layers	Epochs
FCNN	0.001	32	Dense 64, relu Dense 32, relu Dense 1, sigmoid	50
CNNs	0.001	32	LSTM 64, Droput (0.2) Dense 32, relu Dense 1, sigmoid	50
LSTM	0.001	32	Conv2D (32, (1,1)), relu MaxPooling1D (2), Flatten Dense 1, sigmoid	50

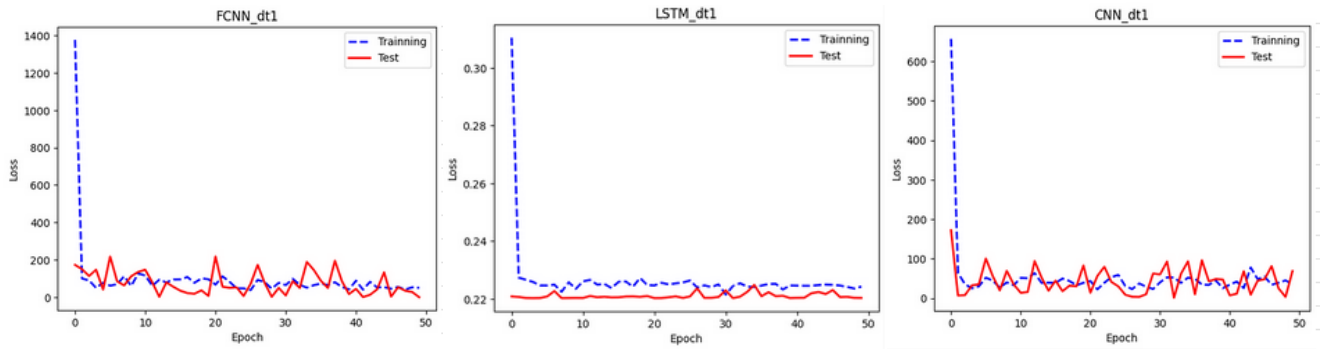

Figure 9 Loss of SEM-based feature-based models Case 1.

DOI: 10.60101/jarst.2024.260451

JOURNAL OF APPLIED RESEARCH ON SCIENCE AND TECHNOLOGY

This research has set Hyperparameters, or values that are set before training the model without being learned by the model itself. Details are as shown in Table 2.

The loss test results are shown in Figure 9 From Figure 10, it can be seen that the loss value result is not very good. In each model, the test results fluctuate, indicating that the model still needs a large amount of training data, and the internal structure of the model still needs to be less complex. The experimental results are shown in Table 3.

From Table 3, it can be seen that all the models have the value of 1, indicating that the model is overfitting, or the model has learned too much and cannot be used in practice. This experimental result indicates that if we introduce features based on SEM, it will result in overfitting of the model.

Table 3 In case 1 results of the predictive model by specifying the input of the reference model according to SEM.

Algorithm	Time	Loss	Accuracy	Precision	Recall	F1-Score
FCNN	18	3.2284	1	1	1	1
CNNs	26	1.113	1	1	1	1
LSTM	19	0.0818	1	1	1	1

The heatmap [25] shown here helps us to understand the relationship between data in the equipment maintenance dataset more easily. The correlation value in the heatmap tells us how much two variables are related. If the value is close to 1, there is a clear positive correlation between the two variables, i.e. when the value of one variable increases, the other variable tends to increase. On the contrary, if the value is close to -1, there is a negative correlation between the two variables, i.e. when the value of one variable increases, the other variable tends to decrease. If the value is close to 0, there is no clear correlation between the two variables.

From the heatmap, we can see that some variables have a significant impact on the maintenance (Status Maintenance). For example, Working Status and Operational have a positive correlation, meaning that the working status and usage of the equipment are important factors in determining the need for maintenance. In addition, the variable Minutes Used, which represents the time the equipment is used, is also highly relevant, meaning that equipment that is used more often requires more maintenance. At the same time, some variables, such as Skill Level and Management, have a negative correlation, meaning that when employees are more skilled or better managed, the need for maintenance may be reduced.

In addition, some variables do not have a clear impact on maintenance, such as Tool Name and Part Name, which have correlation values close to zero, so it can be considered that these variables may not be necessary in the forecasting model.In case 2, the features are input including Operational, leDay, Management, Working_Status, Car_Number, Tool_Name, Management, Years_Left, Calibrated, Part_Name, Hours_Used, and Minutes_Used, which are combined features from SIM and Heat Map with values greater than 0, with the following Loss values as shown in Figure 10.

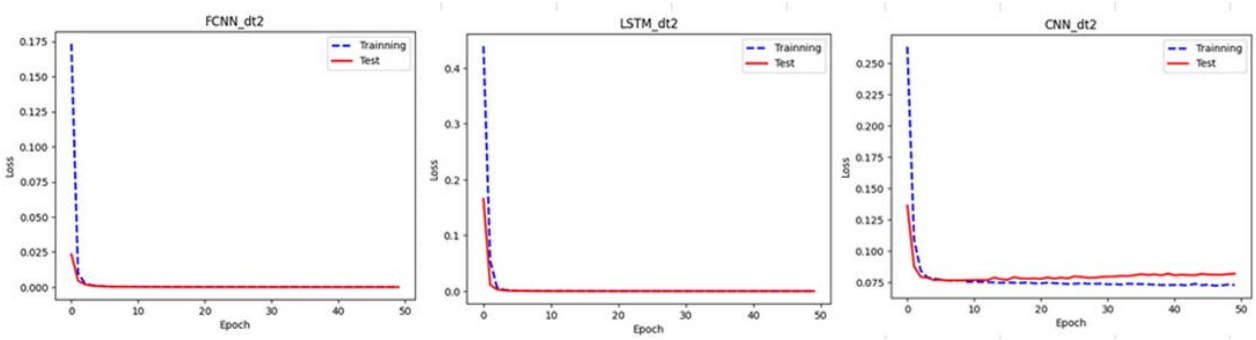

Figure 10 Loss of SEM-based feature-based models.

From Figure 11, it can be seen that all prediction models have Test Loss values that are very close to the Training values.

In the FCNN model, the Loss values start to be close to each other from the beginning of training and remain constant throughout, while LSTM has lower values at the beginning and starts to be close to each other in 5-10 training rounds and remains constant throughout. This characteristic shows that the prediction model does not need a very high number of training rounds. Meanwhile, CNNs in the beginning are similar to LSTM; but will start to overfit more when training reaches 10 rounds or more. This characteristic shows that the prediction model is suitable for training no more than 10 rounds. If it exceeds this, the model will not work. The details of the experimental results are shown in Table 4.

DOI: 10.60101/jarst.2024.260451

JOURNAL OF APPLIED RESEARCH ON SCIENCE AND TECHNOLOGY

Table 4 In case 1 results of the predictive model by specifying the input of the reference model according to SEM.

Algorithm	Time	Loss	Accuracy	Precision	Recall	F1-Score
FCNN	23	0.0424	1	1	1	1
CNNs	26	0.2203	0.94	0.94	0.97	1
LSTM	18	68.9337	0.94	0.94	0.97	1

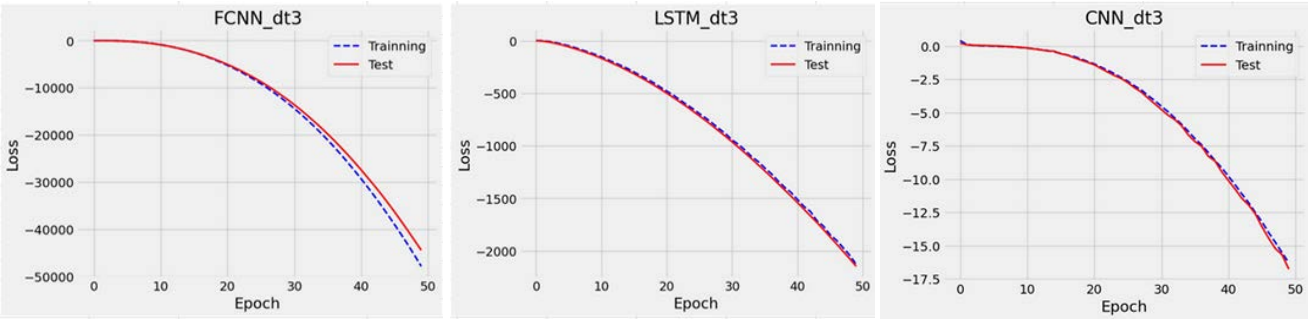

Figure 11 Loss of SEM-based feature-based models.

Table 5 In case 1 results of the predictive model by specifying the input of the reference model according to SEM.

Algorithm	Time	Loss	Accuracy	Precision	Recall	F1-Score
FCNN	20	-75058.70	1	1	1	1
CNNs	36	-3183.13	0.94	0.94	0.97	1
LSTM	40	-2135.13	0.94	0.94	0.97	1

Case 3 will insert all the feature values, which will consist of Car_Number, Working_Status, Skill_Level, Years_Left, Manual_Available, Tool_Name, Tool_Size, Calibrated, Operational, Part_Name, Installation_Dete, Hours_Used, Minutes_Used, Expiration_Date, Date_Now, leDey and Management, with the model loss values as shown in Figure 11.

From Figure 11, it can be seen that all models have the Loss value of Underfitting or the negative Loss value, which indicates that the prediction model receives too much Input value, but the internal structure is too complex, resulting in a negative Loss value and the model cannot be used. The details of the experimental results are shown in Table 5.

From Table 5, it can be seen that the Loss value of all models is very high. Although the test results of Accuracy, Precision, Recall, and F1-Score show that this model works, in reality, this model cannot work with such a variety of data. If all the features are needed, the internal structure of the prediction model should be developed to be more complex, which will result in better training Loss value.

From Table 3-5 of this experiment, the researcher has divided the data set into 3 parts: Data set 1, 60%, is used for training. Data set 2, 20%, is used for data tuning. And the third set of data, another 20%, is used for testing. From picture 10-12, the results of Training will be blue lines and the results of Testing will be red lines. For data tuning, it is a model tuning process where the three models above have been fine-tuned on the data set used for 20% tuning. The researcher selects the model with the best value from the results of data tuning to test and compare with the data set to divide the test again. Therefore, the values have shown in the graphs in Figure 10-12 are the results of a comparison between the training data sets and those used for testing. In the case where the red curve and the blue line run further apart according to the number of training rounds, it means that the model is underfitting or the model is not predicting accurately. This must be fixed by increasing the training cycle or adjusting the architecture of the new model. In the case of the red graph lines running parallel to each other and keep running closer to each other. When increasing the rounds of training, it means that the model has good prediction performance, and in the case where the red and blue line graphs intersect and run away from each other or run parallel but keep getting negative values according to the number of training cycles, it means that the model is overfitting or the model can only remember the training results when new data is encountered, the model is unable to predict or makes incorrect predictions. This will require adjusting the architecture of the new model to solve the problems.

Link Dataset :
https://drive.google.com/drive/folders/1q5SpnN-WycJEuzs53DdvbXM7IoeVzseS?usp=sharing.

CONCLUSIONS

The analysis of the experimental results in each case can clearly show the advantages and

DOI: 10.60101/jarst.2024.260451

disadvantages of the used models and indicate the suitability of the data features used in each situation. In this study, the researcher used Anaconda and Google Colab to run the Python program. The advantage of using FCNN, LSTM, and CNNs in selecting such models for comparison in this study. FCNN has the ability to analyze the relationship among features. Especially good at classifying damage and predicting worn out spare parts. LSTM is suitable for serial data, it has the ability to predict the lifespan of spare parts and detect trends in failure and CNNs is capable of analyzing patterns in spatial data and automatically extracting features. These three models are therefore suitable to be used in this study. In the first case, using only four features, namely Working Status, Operational, leDay, and Management, which are from the SEM model, all FCNN, CNNs, and LSTM models show the highest Accuracy and Precision values of 1.0, which are excellent results in numerical terms. However, considering the high and fluctuating Loss values throughout the training, it is clear that these models have the problem of Overfitting. The models can perfectly remember the training data, but they cannot properly adapt to new, never-seen data. This problem comes from the fact that the input data is too limited. Therefore, the models cannot sufficiently learn the complexity of the data in real situations. In the second case, which increases the variety of data features, such as Operational, Tool Name, and Hours Used, the models perform better. The training Loss values are significantly reduced and are more stable than in the first case, especially in the FCNN and LSTM models, which show Accuracy values close to 0.94 throughout the training process. While CNNs, despite their good initial performance, However, the trend of overfitting begins when the training exceeds the 10^{th} iteration. The experimental results in this case show that increasing the number and variety of data features helps the model to better understand the relationship between variables. However, the problem of overfitting CNNs can be solved by reducing the number of training iterations or reducing the complexity of the model structure. In the last case, when all data features are combined, all models show very high, sometimes negative, loss values, indicating an overfitting problem where the model cannot learn enough about the complexity of the data. Although the CNN and LSTM models still maintain an accuracy of 0.94, the very high loss values make the results unreliable. This problem is caused by the fact that the data contains too many features, making the model unable to process the relationships efficiently. In addition, the internal structure of the model may not be suitable for the increasing complexity of the data. Adding features without deeply analyzing whether each feature is important for forecasting may hurt the model's ability. When comparing the three cases, it can be seen that Case 2 is the most balanced, both in terms of the number of features and model performance. The low and constant loss value reflects the model's ability to learn the data efficiently. While cases 1 and 3 suffer from overfitting and underfitting, respectively, this analysis shows that the diversity and appropriateness of the input data are key to the model's success. Moreover, optimizing the model structure to suit the data characteristics, such as reducing the number of training iterations or using regularization techniques, can help the model adapt and perform better in different scenarios with optimal performance.

Future suggestions

Future research: the most effective method for future research should be focused on developing hybrid models that combine the advantages of FCNN, LSTM, and CNNs to improve the ability to analyze data with different characteristics. The scope of the dataset used in the research should be expanded, such as integrating temporal data in real work processes and variables directly related to the environment, to increase the accuracy and depth of the results. In addition, developing deep learning techniques that can be adapted to the characteristics of data in each field, such as preventive maintenance in various industries, will improve efficiency and reliability. Testing and improving the model on different machines or equipment will help to understand the suitability of the model in different contexts more deeply.

REFERENCES

1. Carvalho TP, Soares FA, Vita R, Francisco RdP, Basto JP, Alcalá SG. A systematic literature review of machine learning methods applied to predictive maintenance. Computers & Industrial Engineering. 2019;137;106024.
2. Somkait Hoonsakul, Palanan Pajayakrit, Somsuk Khaemkham, Yutth Kaiyawann. Causal factors influencing the maintenance efficiency of Thai Air Force helicopters. Kasetsart Engineering Journal. 2016;29(98):43-54.
3. Nittiya Khosantia, Chanissara Kaewsawan, Phatre Friestad. Strategic guidelines for developing Thailand's aircraft maintenance industry. Journal of MCU Peace Studies. 2021;9(4):1397-1406.
4. Suchet Reaboot. Enhancing fraud detection in financial systems using machine learning and network analysis techniques [thesis]. Bangkok: Dhurakij Pundit University, College of Innovative Technology and Engineering; 2022.
5. Hecht-Nielsen R. Theory of the backpropagation neural network. Neural networks for perception: Elsevier; 1992. p. 65-93.

DOI: 10.60101/jarst.2024.260451

6. LeCun Y, Bengio Y, Hinton G. Deep learning. nature. 2015;521(7553):436-44.
7. Dean J, Corrado G, Monga R, Chen K, Devin M, Mao M, et al. Large scale distributed deep networks. Advances in neural information processing systems. 2012;25.
8. Han S, Liu X, Mao H, Pu J, Pedram A, Horowitz MA, et al. EIE: Efficient inference engine on compressed deep neural network. ACM SIGARCH Computer Architecture News. 2016;44(3):243-54.
9. Akhtar MZ, Kreiner C, Schmid M, Zippelius A, Tetzlaff U, Elger G, editors. Fully Connected Neural Network (FCNN) Based Validation Framework for FEA Post Processing to Improve SAC Solder Reliability Analysis. 2024 IEEE 10th Electronics System-Integration Technology Conference (ESTC); 2024: IEEE.
10. Song Y, Wang D, Xiong X, Cheng X, Huang L, Zhang Y. The Prediction and Dynamic Correction of Drifting Trajectory for Unmanned Maritime Equipment Based on Fully Connected Neural Network (FCNN) Embedding Model. Journal of Marine Science and Engineering. 2024;12(12): 2262.
11. De Filippi FM, Ginesi M, Sappa G. A fully connected neural network (FCNN) model to simulate karst spring flowrates in the Umbria region (Central Italy). Water. 2024;16(18):2580.
12. Han S, Pool J, Tran J, Dally W. Learning both weights and connections for efficient neural network. Adv Neur In. 2015;28.
13. Qian Z, Hayes TL, Kafle K, Kanan C. Do we need fully connected output layers in convolutional networks? arXiv preprint arXiv:200413587. 2020.
14. Sze V, Chen YH, Yang TJ, Emer JS. Efficient processing of deep neural networks: A tutorial and survey. Proc IEEE. 2017;105(12):2295-329.
15. Huang Gao, Liu Z, Pleiss G, Maaten Laurens van der, Weinberger KQ. Convolutional Networks with Dense Connectivity. IEEE Transactions on Pattern Analysis and Machine Intelligence. 2019;44(12):8704-16. doi: 10.1109/TPAMI.2019.2918284.
16. Hochreiter S. Long Short-term Memory. Neural Computation MIT-Press. 1997.
17. linPremjith B, Soman K, Kumar MA. A deep learning approach for Malayalam morphological analysis at character level. Procedia Comput Sci. 2018; 132:47-54.
18. Upreti A. Convolutional neural network (cnn). a comprehensive overview. 2022.
19. Purwono P, Ma'arif A, Rahmaniar W, Fathurrahman HIK, Frisky AZK, ul Haq QM. Understanding of convolutional neural network (cnn): A review. International Journal of Robotics and Control Systems. 2022;2(4):739-48.
20. Wu Z. Application of CNN Classic Model in Modern Image Processing. Journal of Advances in Engineering and Technology. 2024;1(3):1-6.
21. Kalchbrenner N, Grefenstette E, Blunsom P. A convolutional neural network for modelling sentences. arXiv preprint arXiv:1404.2188. 2014.
22. Khunsuk T, Thongkam J. Feature selection method for improving customer reviews classification. RMUTI J Sci Technol [Internet]. 2019 Oct 7 [cited 2025 Jan 19];13(1):129-43. available from: https://ph01.tci-thaijo.org/index.php/rmutijo/article/view/188091.
23. Khiewwan K, Weeraphan P, Tantisontisom K, Ongate J. Application of Data Mining Techniques for Classification of Traffic Affecting Environments. J. Renew. Energy Smart Grid Technol [internet]. 2020 Jun. 28 [cited 2025 Jan. 19];15(1). available from: https://ph01.tci-thaijo.org/index.php/RAST/article/ view/240698.
24. Krstinić D, Braović M, Šerić L, Božić-Štulić D. Multi-label classifier performance evaluation with confusion matrix. Computer Science & Information Technology. 2020;1:1-14.
25. Jain A. Unveiling the power of heatmaps in data visualization [Internet]. Medium. 2023 [cited 2024 Dec 24]. Available from: https://medium.com/@abhishekjainindore24/unveiling-the-power-of-heatmaps-in-data-visualization8b370efca935.

DOI: 10.60101/jarst.2024.260451

Received: January 6, 2025 | Revised: March 17, 2025 | Accepted: March 25, 2025

JOURNAL OF APPLIED RESEARCH ON SCIENCE AND TECHNOLOGY
JARST
INSTITUTE OF RESEARCH AND DEVELOPMENT
RAJAMANGALA UNIVERSITY OF TECHNOLOGY THANYABURI
ISSN ONLINE: 2773-9473
https://ph01.tci-thaijo.org/index.php/rmutt-journal

Fabrication of uric acid chemical sensor based on tricobalt tetroxide crosslinked chitosan with gold nanoparticle modified glassy carbon electrode

Nuenghathai Chaiya[1], Suphaporn Chenkhuruthum[1], Ratchadaporn Puntharod[2], Anchana Preechaworapun[3], Pusit Pookmanee[2] and Tanin Tangkuarum[2*]

[1]Applied Chemistry Program, Faculty of Science, Maejo University, Chiang Mai, THAILAND

[2]Chemistry Program, Faculty of Science, Maejo University, Chiang Mai, THAILAND

[3]Department of Chemistry, Faculty of Science and Technology, Pibulsongkram Rajabhat University, Phitsanulok, THAILAND

[*]Corresponding author: tanin.tang@gmail.com

ABSTRACT

Sensor technology has advanced significantly in recent years and has become an essential tool in various fields, including medicine, food analysis, and environmental monitoring. Uric acid (UA) is a biomarker for several diseases, such as gout and kidney stones. This research develops an electrochemical sensor for the determination of UA based on tricobalt tetroxide (Co_3O_4) and gold nanoparticles (AuNPs) in the crosslinked chitosan polymer (CHIT) and modified on the glassy carbon electrode (GCE) (Co_3O_4-CHIT/AuNPs/GCE). X-ray diffractometer (XRD) and scanning electron microscope (SEM) were used to characterize the synthesized Co_3O_4, which was crystallized in a cubic phase with a flower-like structure, while AuNPs were successfully synthesized and confirmed by UV-Vis spectroscopy. The Co_3O_4-CHIT/AuNPs/GCE was tested in 0.15 mM of UA using cyclic voltammetry (CV) and gave an oxidation peak at +0.61 V. The Co_3O_4-CHIT/AuNPs deposited on GCE exhibited the ability to oxidize the UA and obtained a higher current compared to the bare, Co_3O_4-CHIT, and AuNPs modified electrodes for 1.79, 2.03, and 1.47 times, respectively. The analytical specification of this sensor was studied by amperometric technique in phosphate buffer pH 7.0 at suitable parameters of applied voltage, AuNPs, and Co_3O_4-CHIT for + 0.65 V, 20 µL, and 60 µg, respectively. It was found that the linearity obtained from 0.5 to 700 µM ($y = 0.0079x + 0.0049$, $R^2 = 0.9996$) with a limit of detection (LOD) of 0.31 µM (S/N =3) and limit of quantification (LOQ) was calculated to be 1.03 µM. We found that 0.01 mM ascorbic acid, 0.5 mM urea, 0.1 mM caffeine, 5.0 mM Cl^-, 7.0 mM glucose, and 20.0 mM sucrose did not affect the UA analysis. The repeatability and reproducibility were obtained at 2.94 %RSD (n=5) and 2.30 %RSD (n=5), respectively. This sensor was applied to detect uric acid in blood samples without any preparation before the test. It showed high accuracy in terms of %recovery within the range of 96.76-104.92.

Keywords: Glassy carbon electrode, Tricobalt tetroxide, Chitosan crosslinking gold nanoparticle, Uric acid

INTRODUCTION

Uric acid (UA) is a waste product produced when the body breaks down purines, which are found in many foods such as red meat, poultry, seafood, drinks with high fructose corn syrup, and alcohol. It is created from processed chemical purines in the body for repair or building cells. UA in human metabolism is excreted via urine by the kidneys. It is recommended that the blood level of men should not exceed 7 mg/dL and that of women, not over 6 mg/dL [1]. However, some references showed that the recommended range of UA in blood for adult males is 4.0-8.5 mg/dL or 0.24-0.51 mM; for adult females, it is 2.7-7.3 mg/dL or 0.16-0.43 mM. UA levels play a crucial role in maintaining health. Elevated UA levels are associated with conditions such as gout, kidney stones, renal failure, and kidney disease. Conversely, lower UA levels have been linked to neurological disorders, including multiple sclerosis, Parkinson's disease, Alzheimer's disease, Fanconi syndrome, and optic neuritis. However, due to UA's antioxidant properties, it contributes to brain protection [2]. Currently, UA levels in the blood are detectable via a variety of medical diagnostic tests, such as high-performance liquid chromatography (HPLC) [3, 4] and spectroscopy [5]. However, these techniques are time-consuming and require specialized equipment and trained personnel. As a result, there is growing interest in the development of methods for UA that can be used for rapid and accurate monitoring of the blood or other bodily fluids using a variety of techniques, such as electrochemical [6-8], optical [9], and colorimetric [10] methods.

DOI: 10.60101/jarst.2024.260199

The electrochemical method is more popular than other techniques as it possesses rapid analysis times, simple experimental procedures, and inexpensive instrumentation. Different electrochemical techniques have been applied for the detection of target analytes, including cyclic voltammetry (CV) [11, 12], electrochemical impedance spectroscopy (EIS) [13], and differential pulse voltammetry (DPV) [14, 15]. Omar et al. [16] have reported the immobilization of uricase onto graphene oxide (GO) and using 1-ethyl-3-(dimethylaminopropyl) carbodiimide (EDC) and N-hydroxysulfosuccinimide (NHS) as crosslinking reagents on glassy carbon electrode (GCE) for the detection of uric acid (UA) via cyclic voltammetry (CV). They found a linear dependence on the UA concentration ranging from 0.02 to 0.49 mM with a detection limit of 3.45 mM and presented good reproducibility. Jirakunakorn et al. [17] developed a method by immobilizing uricase on a porous cryogel platform of graphene-incorporated chitosan (CHIT) on top of a Prussian blue layer (PB) by electrodeposition on a screen-printed carbon electrode (SPCE). They employed an amperometric detector integrated with a flow-injection system, which showed a linear detection range from 0.0025 to 0.40 mmol L^{-1} and a detection limit of 2.5 µmol L^{-1}. Remarkably, common interferents in human serum samples had no significant effect on the detection performance. These reports show the advantages of electrochemical sensors.

Tricobalt tetroxide (Co_3O_4) is still used in various industries and research. It has oxidation numbers of 2+ and 3+ and crystallizes in a cubic structure [18]. Its properties are high surface area, good conductivity [19], strong catalytic activity, and p-type semiconductor [20], These properties make it an ideal material for use in sensors [21, 22], supercapacitors [23], and catalytic [24]. Gold nanoparticles (AuNPs) have a high surface area-to-volume ratio [25] and possess good biocompatibility [26]. It continues to be popular and is still used with various syntheses, such as green synthesis [27]. Numerous studies have explored the applications of AuNPs, such as Ismail et al. [28], the development of an electrochemical sensor based on silica/gold nanoparticles for the detection of arsenic, and Qingshan Yang et al. [29], the development of a glucose sensor using AuNPs and glucose-oxidase. Chitosan (CHIT) is classified as a natural biopolymer, with properties that enable gelling and membrane formation [30]. In the last few years, its applications have expanded to include medicine for wound healing, drug delivery, and tissue engineering due to its biocompatibility and antimicrobial activity. Moreover, they obtained interest from electrochemical sensors for immobilizing nanomaterials, increasing the sensitivity, selectivity, and stability of the electrochemical sensors [31]. For example, CHIT was utilized in improving the stability of glucose sensors based on hydrogels [32], and Chachuli et al. present a polymer-based gas sensor comprising chitosan as binder and graphene as a sensing material for acetone and ethanol [33].

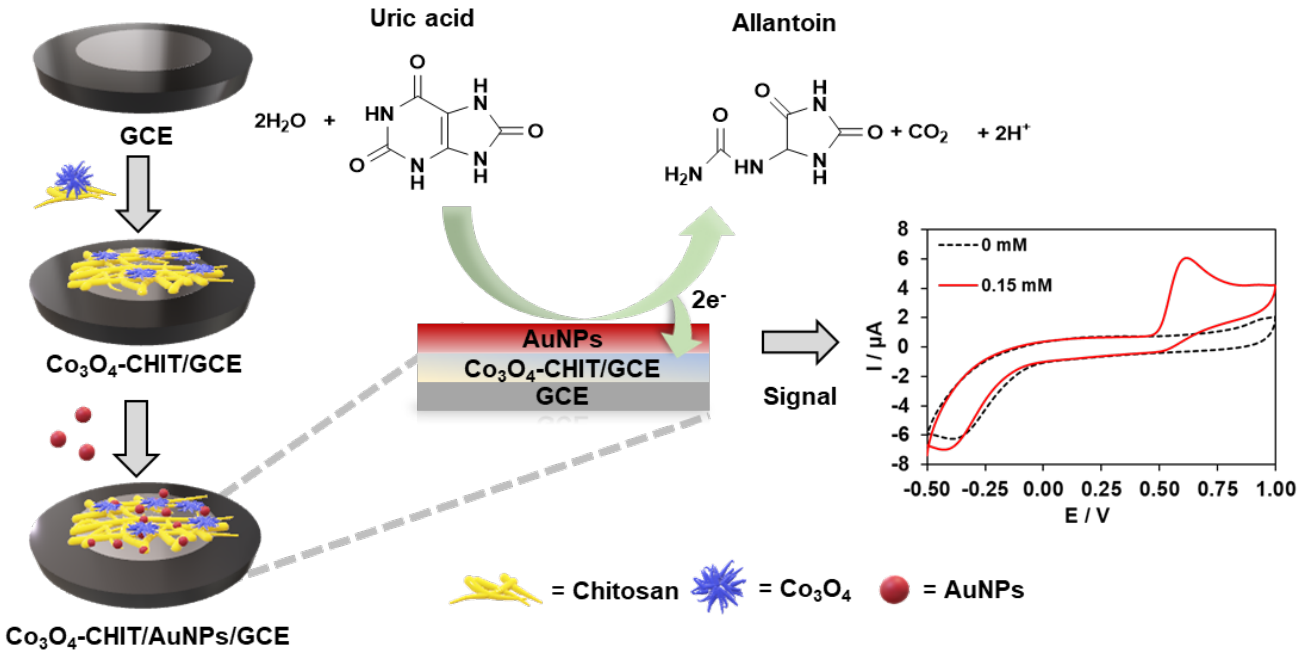

Scheme 1 The fabrication process of the sensor and possible mechanism for UA detection.

Based on our knowledge, there is no report of the fabrication of Co_3O_4 with biocompatible polymers such as CHIT and AuNPs. This research aims to synthesize Co_3O_4 with AuNPs in CHIT polymer to determine UA in blood samples by an electrochemical technique. Hence, this work presents a significant challenge due to the absence of enzymes for UA detection. The primary advantage of this approach is the enhanced long-term stability of the electrodes, as enzymes typically limit the sensor's lifespan and are highly sensitive to temperature fluctuations and chemical interference. Furthermore, eliminating the need for enzymes

DOI: 10.60101/jarst.2024.260199

JOURNAL OF APPLIED RESEARCH ON SCIENCE AND TECHNOLOGY

contributes to cost reduction. Scheme 1 showed the fabrication and conceptual model of possible mechanisms for detecting UA. It was oxidized into allantoin, releasing two electrons and two protons [6, 34]. The obtained current was facilitated by Co_3O_4-CHIT/AuNPs and measured by an electrochemical technique of cyclic voltammetry and amperometry.

MATERIALS AND METHODS

Materials

The cobalt nitrate hexahydrate (99%), and glacial acetic acid were obtained from QRëC (New Zealand). Caffeine (99%), disodium hydrogen phosphate (99%), L-ascorbic acid (99.5%), sodium borohydride (97%), sodium acetate (99.5%), and sodium chloride (99.5%) were provided by Loba Chemie Pvt. Ltd. (India). The D-glucose (99.5%) anhydrous was provided by Ajax Finechem (NSW, Australia). Urea (99%), sodium hydroxide (97%), and potassium dihydrogen phosphate (99.5%) were supplied from RCI Labscan (Bangkok, Thailand). Chitosan (low molecular weight, 75%), uric acid (UA, 99%), gold (III) chloride trihydrate (49%), sodium citrate tribasic dihydrate (99%), and sucrose (99.5%) were received from Sigma-Aldrich, USA. Glutaraldehyde solution (~50%) was provided by Fluka, USA.

All measurements of voltammetry and amperometry were operated with CH1230A (CH instrument, USA) which was controlled by a personal computer. A conventional three-electrode system equipped with a bare glassy carbon electrode (GCE) or the modified GCE as working electrodes, (CH instrument, Ø 3 mm), a Pt wire electrode (CH instrument, Ø 0.5 mm and 3.2 cm long) as a counter electrode, and an Ag/AgCl (3.0 M KCl internal solution, CH instrument) as a reference electrode. All solutions used in this study were prepared with 18.2 MΩ-cm ultrapure water (ZMQ50007, Milli-Q Academic, USA).

Synthesis of gold nanoparticles (AuNPs)

The AuNPs synthesis procedure was adapted from our previous reports[35]. Briefly, 0.01% w/v gold (III) chloride trihydrate, 10 mM sodium borohydride, and 10.0 mM sodium citrate were mixed in a beaker at the mole ratio of Au:$Na_3C_6H_5O_7$:$NaBH_4$ by various 1:0:19, 1:2:17, 1:4:15, 1:9:10, 1:14:5, 1:17:2, and 1:19:0respectively, and vigorously stirred by magnetic stirrer for 15 minutes. Then, the solution was transferred to a hydrothermal synthesis reactor and heated at 120 °C for 30 minutes to obtain AuNPs solution. AuNPs were characterized via scanning absorption spectrum mode by UV-vis spectroscopy (UH5300, Hitachi, Japan).

Synthesis of tricobalt tetroxide (Co_3O_4)

Co_3O_4 was synthesized by modifying the method of Ramesh Lal et al. [36]. Briefly, 0.01 M cobalt nitrate and 0.01 M urea were dissolved in 80 mL of deionized (DI) water in a beaker and stirred for 15 minutes. Next, the solution was transferred to a hydrothermal reactor and heated at 95 °C for 6 h. Then, the suspension in the reactor was evaporated at 80 °C in the hot air oven. Finally, the precipitate was calcined at 500 °C for 5 hours to get tricobalt tetroxide in black-color powder. This synthesized material was characterized by an X-ray diffractometer (XRD) (Bruker, D8, Germany) and scanning electron microscope (SEM) (VEGA, TESCAN, Czech Republic).

Preparation of modified electrode

Co_3O_4-CHIT/AuNPs were deposited on the GCE as follows. Co_3O_4 3.0 mg was dispersed in 1.0 mL of 0.5% CHIT-crosslinked glutaraldehyde by ultrasonicated for 30 min. CHIT acts as a binder to immobilize Co_3O_4 on the electrode surface to ensure strong adhesion and stability of the modified layer. The GCE was cleaned by polishing with a slurry of 0.05 µm Al_2O_3 and rinsed thoroughly with UW. An aliquot of 20.0 µL of Co_3O_4-CHIT was dropped on the cleaned bare glassy carbon electrode surface and left to dry at room temperature. In the last step, 20.0 µL AuNPs solution was placed and left to dry. The Co_3O_4-CHIT/AuNPs/GCE modified electrode was obtained and rinsed with UW before use. AuNPs/GCE and Co_3O_4-CHIT/GCE modified electrodes were modified similarly to Co_3O_4-CHIT/AuNPs/GCE.

Samples analysis

Real blood samples were donated from Sansai Hospital, Sansai district, Chiang Mai, Thailand. The samples were determined for UA without any preparation by the standard addition method.

RESULTS AND DISCUSSION

Characterization of materials

XRD and SEM techniques revealed the crystal phase and morphology of the synthesized Co_3O_4. The XRD pattern of Co_3O_4, as shown in Figure 1A, exhibits diffraction peaks at (111), (220), (311), (222), (400), (422), (511), (440), and (533), which correspond to the cubic crystal structure according to the JCPDS 00-011-1152 reference. Figure 1B shows an SEM image of Co_3O_4 flower-like. The gold nanoparticle (AuNPs) solutions exhibited different colors depending on the molar ratio of Au:$Na_3C_6H_5O_7$:$NaBH_4$ as in Figure 1C. This phenomenon is attributed to the size-dependent optical properties of AuNPs [37]. To confirm the identity of the synthesized AuNPs, their absorbance was measured using a UV-visible spectrophotometer. The absorption spectra were recorded in the 250-800 nm wavelength range. The results indicated that the synthesized AuNPs solutions exhibited maximum absorbance in the range of 520–530 nm as shown in Figure 1D. Surface plasmon resonance (SPR) wavelength is primarily influenced by particle sizes [38]. In the

DOI: 10.60101/jarst.2024.260199

sample with a molar ratio of 1:17:2, the SPR peak appeared at 520 nm with the highest absorbance (0.247), indicating that this sample had the smallest particle size, and the highest concentration compared to other ratios. Due to these favorable characteristics, this AuNPs was selected for further experiments.

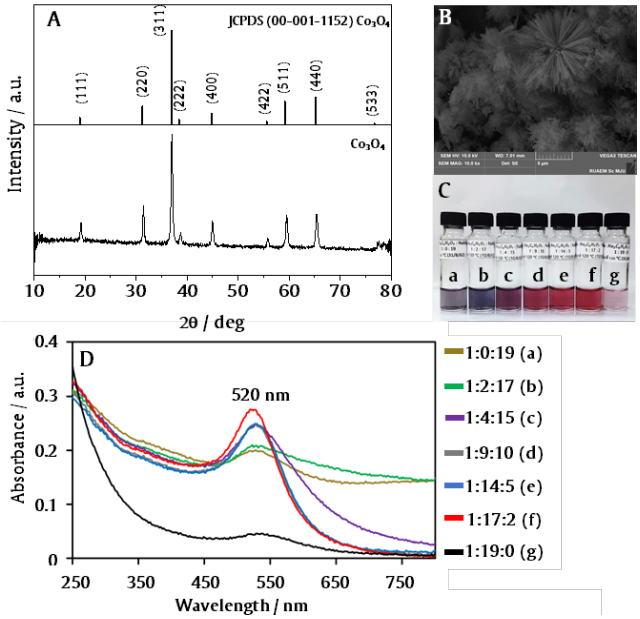

Figure 1 (A) XRD pattern (B) SEM image of Co_3O_4. (C) Photograph and (D) UV-vis spectra of AuNPs solutions at different mole ratios of Au:$Na_3C_6H_5O_7$:$NaBH_4$ at 1:0:1 to 1:19:0 for a to g, respectively. The Labels (a-g) in C and the legends (a-g) in D show the correspondence between C and D.

Cyclic voltammetry of UA

The cyclic voltammogram of 0.15 mM UA was measured in 0.1 M PBS (pH 7.0) at modified/unmodified GCE electrodes to study the electrochemical behavior of UA in Figure 2. The oxidation peak of UA at bare (Figure 2-black), Co_3O_4-CHIT/GCE (Figure 2-brown), AuNPs/GCE (Figure 2-blue), and Co_3O_4-CHIT/AuNPs/GCE (Figure 2-red) appeared at +0.58 V, +0.60 V, +0.60 V, and +0.61 V, respectively. The absence of a reduction peak confirms that the oxidation of UA is an irreversible process in solution. During oxidation, UA donates two electrons and two hydrogen ions, forming allantoin as the primary oxidation product [34, 39]. The reaction mechanism can be represented as reaction (1):

$$\text{Uric acid} + 2H_2O \rightarrow \text{Allantoin} + CO_2 + 2e^- + 2H^+ \quad (1)$$

While oxidation currents were found for 2.94 µA, 2.58 µA, 3.57 µA, and 5.25 µA for bare, Co_3O_4-CHIT/GCE, AuNPs/GCE, and Co_3O_4-CHIT/AuNPs/GCE, respectively, these peaks were almost the same position but notably the current was facilitated by the Co_3O_4-CHIT/AuNPs/GCE which make electron transfer easier with the large surface area resulting in a current higher than the bare GCE, Co_3O_4-CHIT/GCE, AuNPs/GCE for 1.79, 2.03, and 1.47 times, respectively.

Optimization of the Co_3O_4-CHIT/AuNPs/GCE using amperometry

The applied potential of the amperometric technique has a very crucial effect on the oxidation current of UA at the Co_3O_4-CHIT/AuNPs/GCE. It was the first variable parameter to be tested from +0.45 to +0.75 V by spiking UA to the final concentration of 0.15 mM in stirred 0.1 M PBS. Figure 2A displays the current obtained versus the applied potential. The current response increased from +0.45 to +0.65 V, and after that, it decreased from +0.65 to +0.75 V. This trend was related to the cyclic voltammogram of UA. The highest current was obtained at +0.65 V and was chosen for further study.

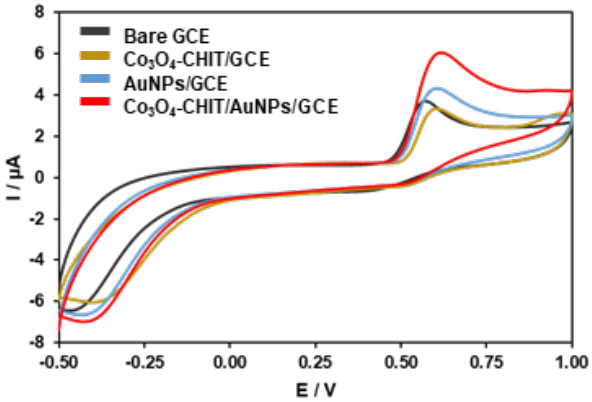

Figure 2 Cyclic voltammograms of bare GCE (black curve), Co_3O_4-CHIT/GCE (brown curve), AuNPs/GCE (blue curve), and Co_3O_4-CHIT/AuNPs/GCE (red curve) of 0.15 mM UA in 0.1 M PBS (pH 7.0) at a scan rate of 50 mV s^{-1}.

Figure 3B shows the obtained currents related to the amount of Co_3O_4 in Co_3O_4-CHIT/AuNPs/GCE. The current steeply increased from 0.0 to 45.0 µg Co_3O_4, reaching its highest at 60.0 µg. It is continuously reduced at 75.0 to 90.0 µg Co_3O_4; the excess thickness causes increased resistance, resulting in lower electron transfer onto the electrode surface [40]. Thus, Co_3O_4 at 60.0 µg was selected for further experiments.

The volume of AuNPs immobilized on the electrode surface varied from 0.0, 10.0, 20.0, 30.0, 40.0, and 50.0 µL in Co_3O_4-CHIT/AuNPs/GCE. The currents were plotted versus the volume of AuNPs in Figure 2C. It was found that 20.0 µL of AuNPs gave the highest signal. The higher excessive AuNPs induced a large barrier to block electron transfer, resulting in lower current at 30.0-50.0 µL.

Figure 2D shows the effect of electrolytes on the signal of 0.15 mM UA at the Co_3O_4-CHIT/AuNPs/GCE. Electrolytes were chosen 0.1 M NaOH, 0.1 M PBS pH 7.0, and acetate buffer pH 5.5 for this study. 0.1 M NaOH and acetate buffer, pH 5.5, can be used as electrolytes, but the currents were lower than in PBS. NaOH shows

DOI: 10.60101/jarst.2024.260199

the lowest obtained current because its pH is more than 10, affecting the precipitation of metal oxide, which resists film conductivity. PBS was chosen for further experiments.

The pH of PBS was varied from pH 6.2 to 7.8 as the electrolyte for UA oxidation at Co_3O_4-CHIT/AuNPs/GCE. The current versus pH of PBS was plotted in Figure 2E. The UA showed the highest oxidation current at pH 7.0, while the current decreased slightly at higher pH 7.4-7.8. The UA oxidation is the preferred basic solution as the product obtains 2 mol of H^+. The elimination of H^+ from the modified electrode surface by reacting with the basic solution, provided the reaction goes forward. Therefore, pH 7.0 can be considered the optimum pH value for detecting UA.

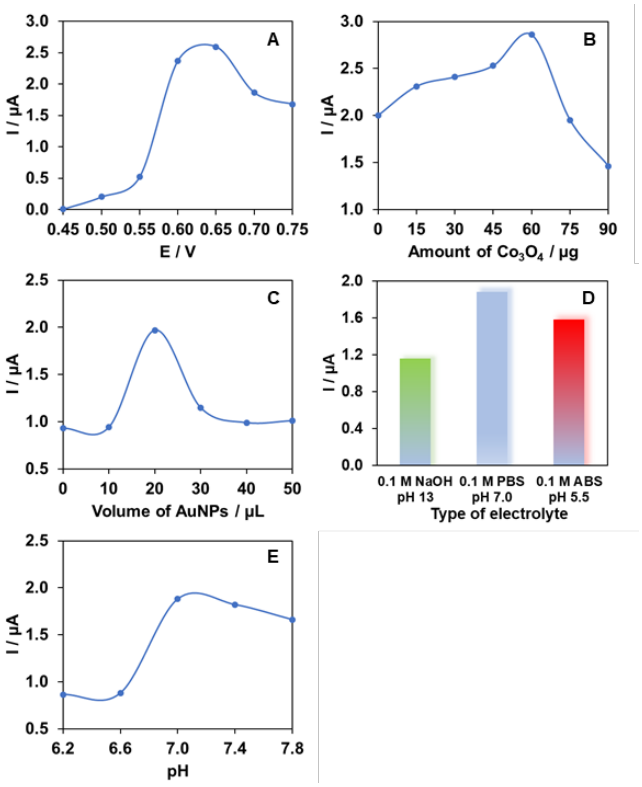

Figure 3 Plot of current response versus variables parameters from the amperometric technique at Co_3O_4-CHIT/AuNPs/GCE; (A) applied potential, (B) amount of Co_3O_4, (C) volume of AuNPs, (D) type of electrolyte, and (E) pH by spiking 0.15 mM.

Linearity

The linearity of UA at Co_3O_4-CHIT/AuNPs/GCE was operated using the obtained conditions by amperometry. Figure 4A shows the successive addition of various concentrations of UA, and the corresponding current versus UA concentration is shown in Figure 4B. There is a linear range from 0.5 – 700 µM ($y = 0.0079x + 0.0049$, $R^2 = 0.9996$). The calculated limit of detection (LOD) (at S/N = 3) was 0.31 µM. Additionally, the limit of quantitation (LOQ) is examined by the equation LOQ= 3.33*LOD, which was found to be 1.03 µM.

Repeatability, reproducibility, interferences, and lifetime

The performance of the Co_3O_4-CHIT/AuNPs/GCE for analyzing UA in terms of repeatability and reproducibility was tested at 0.10 mM UA and 0.15 mM UA, respectively. Figure 5A-red showed the plot of current versus repetition for repeatability assessment by testing five consecutive times at the same Co_3O_4-CHIT/AuNPs/GCE and presenting it in terms of relative standard deviation percentage (%RSD). It showed a value of 2.94 %RSD (n=5). The reproducibility was obtained by operation with the new modifying electrodes at each measurement, and it showed a value of 2.30 %RSD (n=5) in Figure 5A-blue.

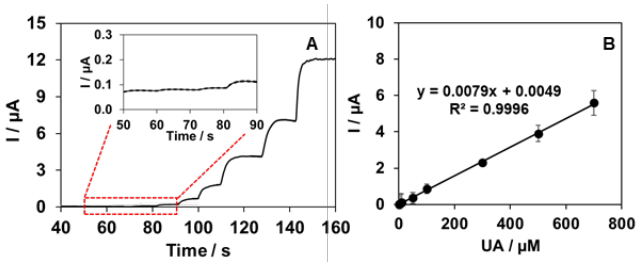

Figure 4 (A) Amperogram of successive addition of UA into 0.1 M PBS pH 7.0 at the Co_3O_4-CHIT/AuNPs/GCE. The inset of A shows zooms in of low UA concentration. (B) Linearity of UA from 0.5 to 700 µM (n=3).

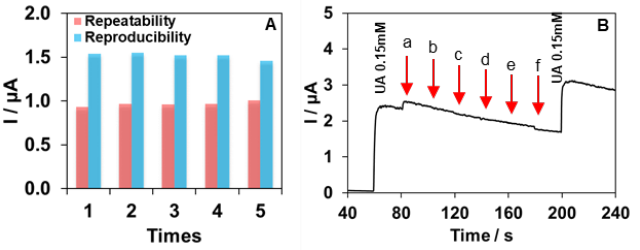

Figure 5 (A) Current response for repeatability (0.10 mM UA) and reproducibility (0.15 mM UA) at Co_3O_4-CHIT/AuNPs/GCE sensor. (B) amperogram of interference effect on the analysis of 0.15 mM UA by spiking of a) 0.01 mM ascorbic acid, b) 0.5 mM urea, c) 0.1 mM caffeine, d) 5.0 mM Cl^-, e) 7.0 mM glucose, and f) 20.0 mM sucrose.

In the study of interference ions of UA, we focused on the ions in blood where UA is present. We select interferences, including ascorbic acid, urea, caffeine, Cl^-, glucose, and sucrose. These compounds were selected because they are commonly derived from dietary intake, are naturally present in the bloodstream, and have oxidation peak potentials close to that of UA, which may potentially interfere with the assay. We found that 0.01 mM ascorbic acid, 0.5 mM urea, 0.1 mM caffeine, 5.0 mM Cl^-, 7.0 mM glucose, and 20.0 mM sucrose did not influence the analyzed UA. Figure 5B shows the amperogram of spiking 0.15

DOI: 10.60101/jarst.2024.260199

mM UA and interfering ions. This evidence proves that the Co_3O_4-CHIT/AuNPs/GCE can be used for UA in the presence of interfering ions. The selectivity of this sensor using metal nanoparticles (Co_3O_4 and AuNPs) reduces interferences contributing to the current signal [34]. Our work agrees that metal nanoparticles enhance selectivity by favoring UA oxidation while suppressing glucose and urea oxidation, as reported by the previous work [36, 41]. Similarly, caffeine does not interfere with this sensor as their oxidation occurs at significantly higher potentials (above +1.2 V vs. Ag/AgCl) [42]. The Cl^- is electrochemically stable and does not oxidize at +0.65 V, ensuring selectivity [43-45]. The direct electrochemical oxidation of sucrose is possible under specific conditions [46]. However, the molecular complexity of sucrose poses challenges, preventing any significant interference. Ascorbic acid is primarily oxidized at lower potentials and is often fully consumed before reaching the applied potential of +0.65 V of Co_3O_4-CHIT/AuNPs/GCE, minimizing its impact.

For the lifetime usage of the modified electrode, we examined continuous operation and found it could be used for 29 cycles in a single preparation. (data do not show). The current from the first five experiments is still higher than 95% compared to the first one.

Determination of uric acid in blood samples

Using the standard addition method, the Co_3O_4-CHIT/AuNPs/GCE sensor was applied to detect UA in blood samples. UA was detectable in all four samples. These samples were then spiked with known concentrations of UA and subsequently re-analyzed. The percentage of recovery was calculated and shown in Table 1. This sensor showed high accuracy, with recovery percentages ranging from 96.76% to 104.92%. The performance of the Co_3O_4-CHIT/AuNPs/GCE sensor for UA was compared to previously reported methods, as summarized in Table 2.

Table 1 Determination of UA concentrations in blood samples.

Samples	UA in sample / µM	Spiked UA / µM	Found UA / µM	%Recovery
1	7.1	200.00	200.6	96.76
2	10.6	200.0	214.5	101.96
3	1.4	200.0	207.6	103.06
4	4.7	200.0	214.5	104.92

Table 2 Comparison of UA sensors by electrochemical approach.

Electrodes	Technique	Linear (µM)	LOD (µM)	Ref.
ITO-ERGO/ZnO	Amperometry	1–400	0.45	[47]
Co_3O_4 porous NSs/GCE	DPV	0-800	12.0	[34]
Co_3O_4-MWCNTs/GCE	CV	100-3,000	5.0	[36]
Co_3O_4 nanostructures/GCE	CV	500-3,500	100.0	[48]
Nafion/Uricase/ZnO/Au	Amperometry	100-590	25.6	[49]
Uricase/AuNPs/MWCNTs/Au	Amperometry	10-800	10.0	[50]
Co_3O_4-CHIT/AuNPs/GCE	Amperometry	0.5-700	0.31	This work

ITO, indium tin oxide electrode; ERGO, electrochemically reduced graphene oxide; ZnO, zine oxide; GCE, glassy carbon electrode; Co_3O_4, tricobalt tetroxide; NSs, nanosheets; DPV, differential pulse voltammetry; MWCNTs, multi-walled carbon nanotubes; CV, cyclic voltammetry; Au, gold electrode; AuNPs, gold nanoparticles.

CONCLUSIONS

In summary, a highly effective UA sensor was successfully developed using Co_3O_4-CHIT/AuNPs modified on a glassy carbon electrode GCE. Incorporating Co_3O_4, CHIT, and AuNPs significantly enhanced the sensor's response to UA due to their synergistic properties. The sensor demonstrated excellent analytical performance, with a wide detection range of 0.5 to 700 µM and a low detection limit of 0.31 µM. Moreover, the sensor exhibited outstanding stability, ease of operation, and strong selectivity. Its long operational lifetime and high accuracy are reflected in a percentage recovery of 96.76% to 104.92%. These results suggest that the Co_3O_4-CHIT/AuNPs/GCE sensor is a promising tool for UA detection in biological samples.

ACKNOWLEDGEMENT

This research project is supported by the National Research Council of Thailand (NRCT) : (Contact No. N41A650115). The author appreciates and acknowledges the Sansai Hospital for providing real blood samples for blinding tests.

DOI: 10.60101/jarst.2024.260199

REFERENCES

1. Maiuolo J, Oppedisano F, Gratteri S, Muscoli C, Mollace V. Regulation of uric acid metabolism and excretion. Int J Cardiol. 2016;213:8-14.
2. Xu L, Li C, Wan T, Sun X, Lin X, Yan D, et al. Targeting uric acid: a promising intervention against oxidative stress and neuroinflammation in neurodegenerative diseases. Cell Commun Signal. 2025;23(1):4.
3. Swinson D, Snaith J, Buckberry J, Brickley M. High performance liquid chromatography (HPLC) in the investigation of gout in palaeopathology. Int J Osteoarchaeol. 2010;20(2):135-43.
4. Li Q, Qiu Y, Han W, Zheng Y, Wang X, Xiao D, et al. Determination of uric acid in biological samples by high performance liquid chromatography-electrospray ionization-tandem mass spectrometry and study on pathogenesis of pulmonary arterial hypertension in pulmonary artery endothelium cells. RSC Adv. 2018;8(45):25808-14.
5. Rocha DL, Rocha FR. A flow-based procedure with solenoid micro-pumps for the spectrophotometric determination of uric acid in urine. Microchem J. 2010;94(1):53-9.
6. Yan Q, Zhi N, Yang L, Xu G, Feng Q, Zhang Q, et al. A highly sensitive uric acid electrochemical biosensor based on a nano-cube cuprous oxide/ferrocene/uricase modified glassy carbon electrode. Sci Rep. 2020;10(1):10607.
7. Zhang Y, Lei W, Xu Y, Xia X, Hao Q. Simultaneous detection of dopamine and uric acid using a poly (l-lysine)/graphene oxide modified electrode. Nanomater. 2016;6(10):178.
8. Jin D, Seo MH, Huy BT, Pham QT, Conte ML, Thangadurai D, et al. Quantitative determination of uric acid using CdTe nanoparticles as fluorescence probes. Biosens Bioelectron. 2016;77:359-65.
9. Hashem SG, Elsaady MM, Afify HG, Omer WE, Youssef AO, El-Kemary M, et al. Determination of uric acid in serum using an optical sensor based on binuclear Pd(II) 2-pyrazinecarboxamide-bipyridine doped in a sol gel matrix. Talanta. 2019;199:89-96.
10. Nishan U, Ullah W, Muhammad N, Asad M, Afridi S, Khan M, et al. Development of a nonenzymatic colorimetric sensor for the detection of uric acid based on ionic liquid-mediated nickel nanostructures. ACS Omega. 2022;7(30):26983-91.
11. Akbari S, Jahani S, Foroughi MM, Hassani Nadiki H. Simultaneous determination of methadone and morphine at a modified electrode with 3D β-MnO_2 nanoflowers: application for pharmaceutical sample analysis. RSC Adv. 2020;10(63):38532-45.
12. Noroozifar M, Khorasani-Motlagh M, Hassani Nadiki H, Saeed Hadavi M, Mehdi Foroughi M. Modified fluorine-doped tin oxide electrode with inorganic ruthenium red dye-multiwalled carbon nanotubes for simultaneous determination of a dopamine, uric acid, and tryptophan. Sens Actuators, B. 2014;204:333-41.
13. Randviir EP, Banks CE. A review of electrochemical impedance spectroscopy for bioanalytical sensors. Anal Methods. 2022;14(45):4602-24.
14. Foroughi MM, Jahani S, Rashidi S, Tayari O, Moradalizadeh M. The development of electrochemical DNA biosensor based on woolen ball-shaped La^{3+}/TiO_2 nanostructure coating: nanomolar detection of vinorelbine. Mater Chem Phys. 2024;315:128893.
15. Hajmalek S, Jahani S, Foroughi MM. Simultaneous voltammetric determination of tramadol and paracetamol exploiting glassy carbon electrode modified with FeNi3 nanoalloy in biological and pharmaceutical media. ChemistrySelect. 2021;6(33):8797-808.
16. Omar MN, Salleh AB, Lim HN, Ahmad Tajudin A. Electrochemical detection of uric acid via uricase-immobilized graphene oxide. Anal Biochem. 2016;509:135-41.
17. Jirakunakorn R, Khumngern S, Choosang J, Thavarungkul P, Kanatharana P, Numnuam A. Uric acid enzyme biosensor based on a screen-printed electrode coated with Prussian blue and modified with chitosan-graphene composite cryogel. Microchem J. 2020;154:104624.
18. Chaiya N, Tapala W, Kunthadee P, Ladrodphan N, Tangkuaram T, Puntharod R. Hydrothermal synthesis of tricobalt tetroxide and characterization. PSRU J Sci Technol. 2023;8(3):20-9.
19. Dongsheng Z, Youlan Y, Yaping D, Rong F. An amperometric l-tryptophan sensor platform based on electrospun tricobalt tetroxide nanoparticles decorated carbon nanofibers. Sens Actuators, B. 2017;241:601-6.
20. Zhou T, Zhang T, Deng J, Zhang R, Lou Z, Wang L. P-type Co_3O_4 nanomaterials-based gas sensor: preparation and acetone sensing performance. Sens Actuators, B. 2017;242:369-77.
21. Vladimirova S, Krivetskiy V, Rumyantseva M, Gaskov A, Mordvinova N, Lebedev O, et al. Co_3O_4 as p-yype material for CO sensing in humid air. Sensors. 2017;17(10).
22. Soomro RA, Nafady A, Ibupoto ZH, Sirajuddin, Sherazi STH, Willander M, Abro MI. Development of sensitive non-enzymatic glucose sensor using

DOI: 10.60101/jarst.2024.260199

complex nanostructures of cobalt oxide. Mater Sci Semicond Process. 2015;34:373-81.

23. Zallouz S, Réty B, Vidal L, Le Meins JM, Matei Ghimbeu C. Co_3O_4 nanoparticles embedded in mesoporous carbon for supercapacitor applications. ACS Appl Nano Mater. 2021;4(5):5022-37.
24. Hu Z, Hao L, Quan F, Guo R. Recent developments of Co_3O_4-based materials as catalysts for the oxygen evolution reaction. Catal Sci Technol. 2022;12(2):436-61.
25. Yeh YC, Creran B, Rotello VM. Gold nanoparticles: preparation, properties, and applications in bionanotechnology. Nanoscale. 2012;4(6):1871-80.
26. Rajendran G, Rajamuthuramalingam T, Michael Immanuel Jesse D, Kathiravan K. Synthesis and characterization of biocompatible acetaminophen stabilized gold nanoparticles. Mater Res Express. 2019;6(9):095043.
27. Niżnik Ł, Noga M, Kobylarz D, Frydrych A, Krośniak A, Kapka-Skrzypczak L, et al. Gold nanoparticles (AuNPs)-toxicity, safety and green synthesis: a critical review. Int J Mol Sci. 2024;25(7):4057.
28. Ismail S, Yusof NA, Abdullah J, Abd Rahman SF. Development of electrochemical sensor based on silica/gold nanoparticles modified electrode for detection of arsenite. IEEE Sens J. 2020;20:3406-14.
29. Yang Q, Zhang X, Kumar S, Singh R, Zhang B, Bai C, et al. Development of glucose aensor using gold nanoparticles and glucose-oxidase functionalized tapered fiber structure. Plasmonics. 2020;15(3):841-8.
30. Bocchetta P, Othman A, Gupta M, Andriani G, Martin P, Kumar Y, et al. Chitosan in electrochemical (bio)sensors: nanostructuring and methods of synthesis. Eur Polym J. 2024;213:113092.
31. Bounegru AV, Bounegru I. Chitosan-based electrochemical sensors for pharmaceuticals and clinical applications. Polym. 2023;15(17):3539.
32. Chmayssem A, Shalayel I, Marinesco S, Zebda A. Investigation of GOx stability in a chitosan aatrix: applications for enzymatic electrodes. Sensors. 2023;23(1):465.
33. Chachuli SAM, Muhammad Azmi NA, Shamsudin NH, Coban O, Aziz SAC. Impact of chitosan as a binder in graphene gas sensor for volatile organic compound detection. ChemistrySelect. 2025;10(4):e202405111.
34. Masrat S, Nagal V, Khan M, Moid I, Alam S, Bhat KS, et al. Electrochemical ultrasensitive sensing of uric acid on non-enzymatic porous cobalt oxide nanosheets-based sensor. Biosensors. 2022;12(12):1140.
35. Tangkuaram T, Ponchio C, Kangkasomboon T, Katikawong P, Veerasai W. Design and development of a highly stable hydrogen peroxide biosensor on screen printed carbon electrode based on horseradish peroxidase bound with gold nanoparticles in the matrix of chitosan. Biosens Bioelectron. 2007;22(9-10):2071-8.
36. Lal R, Bhatia BL, Tahira A, Shaikh SF, Alsalme AM, Al-Othman AA, et al. Synthesis of composite material of cobalt oxide (Co_3O_4) with hydroxide functionalized multi-walled carbon nanotubes (MWCNTs) for electrochemical determination of uric acid. J Mater Sci Mater Electron. 2021;32(15):20047-57.
37. Papafilippou L, Claxton A, Dark P, Kostarelos K, Hadjidemetriou M. Nanotools for sepsis diagnosis and treatment. Adv Healthc Mater. 2020;10:2001378.
38. Subara D, Jaswir I. Gold nanoparticles: synthesis and application for halal authentication in meat and meat products. Int J Adv Sci Eng Inf Technol. 2018;8:1633-41.
39. Krishnamoorthy K, Sudha V, Senthil Kumar SM, Thangamuthu R. Simultaneous determination of dopamine and uric acid using copper oxide nano-rice modified electrode. J Alloys Compd. 2018;748:338-47.
40. Tang T, Zhou M, Lv J, Cheng H, Wang H, Qin D, et al. Sensitive and selective electrochemical determination of uric acid in urine based on ultrasmall iron oxide nanoparticles decorated urchin-like nitrogen-doped carbon. Colloids Surf B. 2022;216:112538.
41. Turkkan G, Bas SZ, Atacan K, Ozmen M. An electrochemical sensor based on a Co_3O_4–ERGO nanocomposite modified screen-printed electrode for detection of uric acid in artificial saliva. Anal Methods. 2022;14(1):67-75.
42. Mersal GAM. Experimental and computational studies on the electrochemical oxidation of caffeine at pseudo carbon paste electrode and its voltammetric determination in different real samples. Food Anal Methods. 2012;5(3):520-9.
43. Du J, Chen Z, Chen C, Meyer TJ. A half-reaction alternative to water oxidation: chloride oxidation to chlorine catalyzed by silver ion. J Am Chem Soc. 2015;137(9):3193-6.
44. Niu X, Li X, Pan J, He Y, Qiu F, Yan Y. Recent advances in non-enzymatic electrochemical glucose sensors based on non-precious transition metal materials: opportunities and challenges. RSC Adv. 2016;6(88):84893-905.

DOI: 10.60101/jarst.2024.260199

JOURNAL OF APPLIED RESEARCH ON SCIENCE AND TECHNOLOGY

45. Hassan MH, Vyas C, Grieve B, Bartolo P. Recent advances in enzymatic and non-enzymatic electrochemical glucose sensing. Sensors. 2021;21 (14):4672.

46. Asghar N, Mustafa G, Jabeen N, Dawood A, Rida, Jabeen Z, Malik QH, et al. Fabrication of efficient and non-enzymatic electrochemical sensors for the detection of sucrose. Sensors. 2023;23(4):2008.

47. Eryiğit M, Urhan BK, Doğan HÖ, Özer TÖ, Ü D. ZnO nanosheets-decorated ERGO layers: an efficient electrochemical sensor for non-enzymatic uric acid detection. IEEE Sens J. 2022;22(6):5555-61.

48. Chang AS, Tahira A, Chang F, Memon NN, Nafady A, Kasry A, et al. Silky Co_3O_4 nanostructures for the selective and sensitive enzyme free sensing of uric acid. RSC Adv. 2021;11(9):5156-62.

49. Zhao Y, Yan X, Kang Z, Pei L, Fang X, Lei Y, et al. Highly sensitive uric acid biosensor based on individual zinc oxide micro/nanowires. Microchim Acta. 2013;180.

50. Chauhan N, Pundir C. An amperometric uric acid biosensor based on multiwalled carbon nanotube-gold nanoparticle composite. Anal Biochem. 2011; 413:97-103.

DOI: 10.60101/jarst.2024.260199

Received: January 24, 2025 | Revised: May 1, 2025 | Accepted: May 6, 2025

Analysis of road settlement on soft soil using 3D finite element method: A case study of the Amata Smart City construction project, Chonburi phase 2

Prachaya Thanakitthada, Attapole Malai* and Kongpop Watcharasawe*
Department of Civil Engineering, Faculty of Engineering, Rajamangala University of Technology Rattanakosin, Nakhon Pathom 73170, THAILAND
*Corresponding author: attapole.mal@rmutr.ac.th, kongpop.wat@rmutr.ac.th

ABSTRACT

The research explores the settlement patterns of road structures built on soft soil at the Amata Smart City Chonburi Phase 2 through evaluating the performance of soil cement column (SCC) support as a ground stabilizing strategy. Soft clay layers extending from 10 to 14 meters deep make up the project site and create substantial difficulties for bearing capacity and long-term subsurface movement. Although the effectiveness of SCC has been widely studied, limited research has addressed the feasibility of constructing roads without SCC by enhancing the strength of native soft soils. This study aims to fill this gap by evaluating alternative soil improvement techniques. A three-dimensional finite element method (3D-FEM) was analyzed to forecast settlements in two conditions involving road structures with or without SCC support. Predicted settlements received evaluations in construction time and the following 30-year operational span. The existing soil strength was evaluated through a parametric analysis to determine whether strengthening the soil would be a suitable alternative to SCC. Without SCC in road construction, maximum settlements amounted to five times higher than those built with it, specifically in the road center area. An Elastic Modulus of 600 MPa proved to be the most effective strength improvement of the original soil, resulting in a 12.28% reduction in differential settlement and a slight 1.75% reduction in total settlement. Applying suitable soil improvement methods allows road construction on soft soil to remain possible by omitting SCC procedures. SCC remains the most effective method for settlement control; however, road construction without SCC is also feasible when the soft soil subgrade is sufficiently improved. Research findings create knowledge that helps developers achieve better road designs, which balance performance quality and economical construction expenses on soft clay-dominated sites.

Keywords: Soft clay, Finite element 3D, Cement column, Road construction

INTRODUCTION

Road construction projects keep expanding due to land transportation being essential for travel logistics. In the region encompassing Bangkok and the provinces of Chonburi, Samut Prakan, Samut Sakhon, and Samut Songkhram, roads have been constructed on soft clay deposits with a water content of 60 - 140% by weight and a void ratio of approximately 2.0 [1]. Such characteristics within the soil lead to weak shear strength, minimal load capacity, and substantial settlement [2]. The poor permeability of soft clay results in long-term settlement during loading phases, creating major obstacles for construction activities. Differential settlement is a primary cause of road structural damage because it produces both transportation efficiency losses and safety hazards [3].

To mitigate settlement and instability in road construction, soil cement columns (SCC) have been widely implemented as a ground improvement technique [4-11]. The application of this method yields permanent engineered columns which are produced by mixing cement with soil at the construction site to both decrease settlement and increase bearing strength [8, 9]. However, SCC construction involves high costs due to the need for specialized machinery and complex procedures. Project implementation using soil cement columns faces financial difficulties during large-scale projects that demand extensive installation of columns. The high costs of installing SCC have prompted researchers to evaluate alternative soil improvement strategies including subbase stabilization with cement (Soil Cement Subbase) [14-17] which delivers more affordable solutions.

Despite the proven effectiveness of SCC, limited research has focused on the feasibility of constructing roads on soft clay without SCC by strengthening the natural subgrade [14-17]. This study addresses this knowledge gap by evaluating the settlement behavior of road structures built without SCC support, using subgrade improvement techniques as a potential alternative [4-11].

DOI: 10.60101/jarst.2024.260742

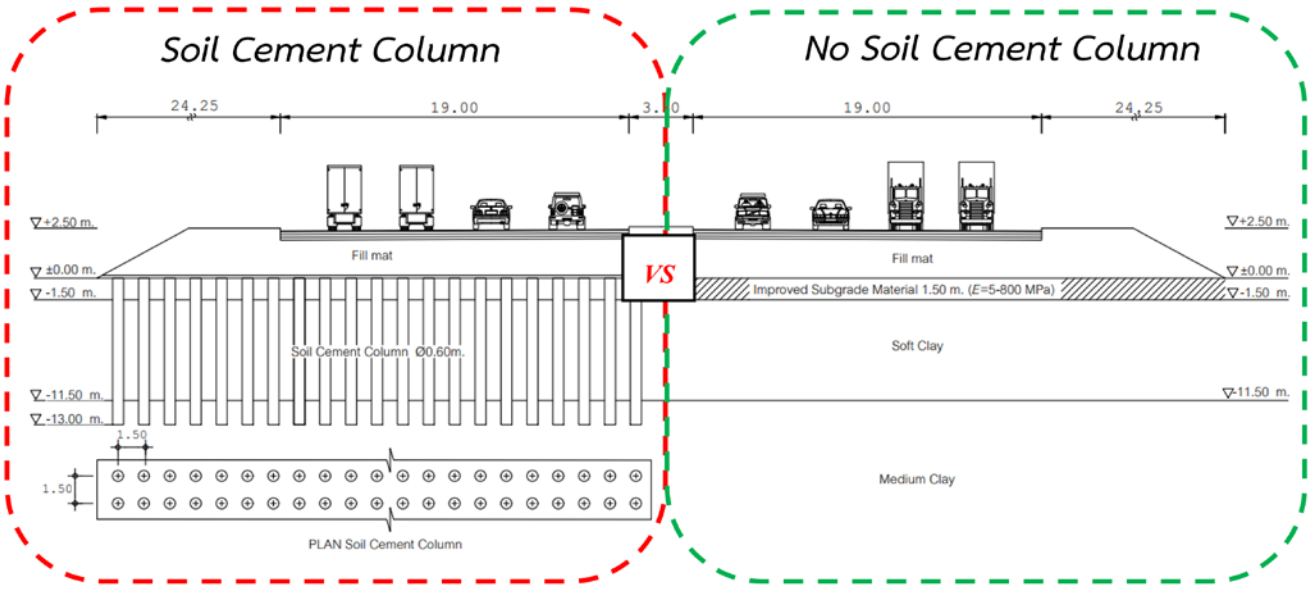

Figure 1 Road structure with and without soil-cement columns.

Multiple studies recently utilized the three-dimensional finite element method (3D-FEM) to study settlement behavior in soft clay because it produces trustworthy results [18-24]. This study applies finite element analysis to simulate the settlement behavior of road structures constructed on soft clay. The examination investigates two road construction methods: soil cement columns and roads without any column support. The main goal focuses on settlement prediction for both construction time and post-construction analysis spanning thirty years. This study investigates the influence of natural soil strength on the feasibility of road construction without SCC. The scope of this research is limited to analyzing settlement behavior under vertical loading only, without considering dynamic traffic loads, environmental effects, or variations in soil stratigraphy beyond the site conditions at Amata Smart City Chonburi Phase 2. The findings obtained from this study are expected to contribute to more effective road planning and design, ensuring long-term structural stability and sustainability.

MATERIALS AND METHODS

The research project evaluates and foretells the settlement patterns in roads and utility systems at various stages of construction without deploying soil cement columns as supporting elements. The analysis evaluates existing soil engineering properties to improve their strength because this strengthens surface load transfer while reducing the likelihood of dangerous differential settlements. A three-dimensional finite element method (3D-FEM) performs the analysis per the cited literature [20,23]. Figure 1 presents the road structure evaluation data between versions with and without soil cement column supports.

A numerical modeling simulation of road settlement patterns on soft clay is conducted through PLAXIS 3D software operations [25]. The research contains two fundamental parts that evaluate (1) settlement patterns in SCC-reinforced road infrastructure and (2) the results of varying existing soil engineering characteristics of Improved Subgrade Material (ISM). A sensitivity analysis on the elastic modulus of ISM, ranging from 5 to 800 MPa, is incorporated to evaluate its impact on settlement behavior.

The Soil-Cement Column (SCC) method involves deep mixing in-situ soft clay with cement to form cylindrical columns that enhance bearing capacity and reduce compressibility. The Improved Subgrade Material (ISM) technique improves shallow soil strength by mixing cement with existing subgrade material and compacting it in layers to form a stabilized mat beneath the road structure.

Finite element model

The road structure in its initial model features soil cement columns with 0.60 meters diameter lasting 13.00 meters and spaced at 1.50 meters intervals. The simulation evaluates both the settlement patterns of structures as well as their performance characteristics. The second part of the analysis makes alterations to enhance the strength characteristics of the existing soil materials. The settlement evaluation between the SCC-stabilized road design and optimized subgrade composition will identify the best solution for road infrastructure development.

A symmetric boundary condition exists for this project road because its 80 meters of total width demonstrates two-sided symmetry, allowing researchers to attain modeling accuracy while minimizing complexity. The model analysis takes place by evaluating symmetrical *YZ* plane boundary conditions at the road centerline while enforcing $U_x = 0$ to restrict *X*-direction movement. A fixed boundary condition has been assigned to

DOI: 10.60101/jarst.2024.260742

JOURNAL OF APPLIED RESEARCH ON SCIENCE AND TECHNOLOGY

the model base to simulate realistic soil responses accurately. The areas that display expected substantial settlement receive mesh refinement as a technique to improve analysis precision. The groundwater table was located 1.5 meters below the ground surface and modeled as a hydrostatic line, with pressure increasing linearly with depth.

The overall dimensions of the model used in this study are 100 meters in width, 250 meters in length, and 26 meters in depth from the ground surface. Mesh refinement was applied in areas expected to exhibit significant settlement, particularly near the road structure and soil improvement zones, with the refined element volumes ranging approximately from 0.2 to 0.6 m³ per element to enhance the analysis precision. The finite element model consists of 684,956 nodes and 326,194 elements, as illustrated in Figure 2.

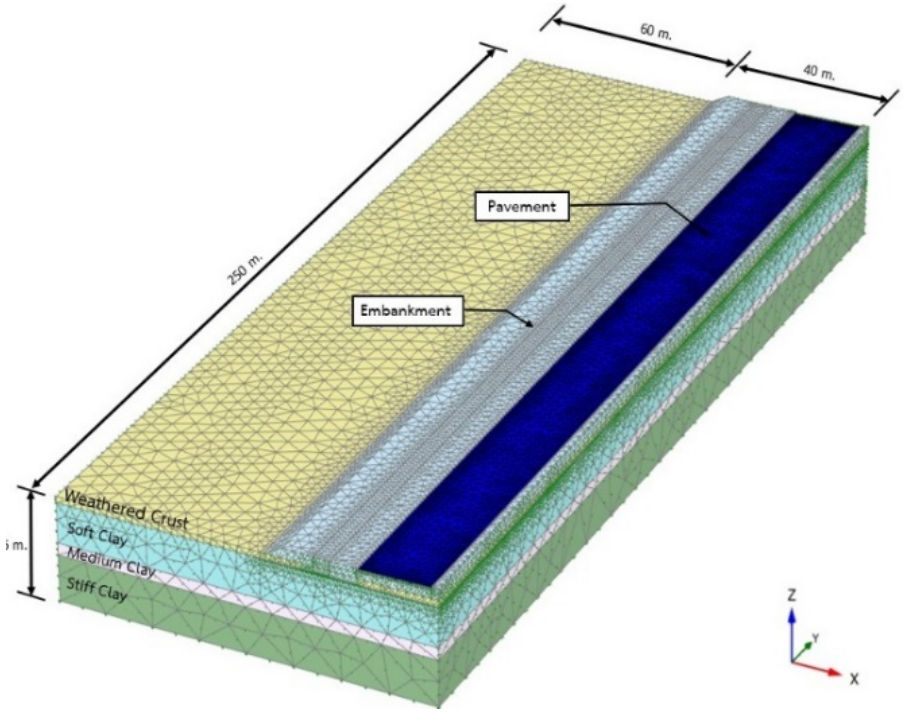

Figure 2 Geometry of the problem and 3D Finite element mesh used in this analysis.

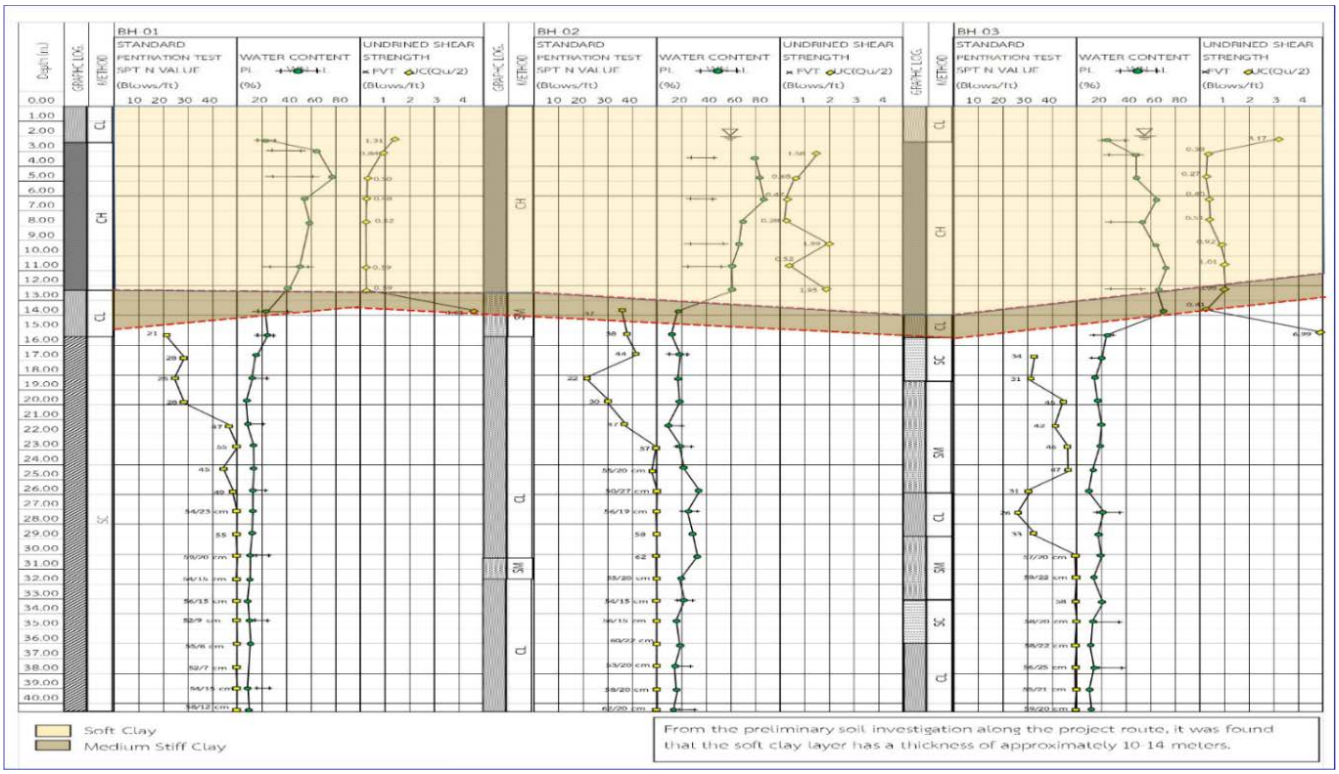

Figure 3 Borehole data for BH-001, BH-002, and BH-003.

DOI: 10.60101/jarst.2024.260742

JOURNAL OF APPLIED RESEARCH ON SCIENCE AND TECHNOLOGY

Subsoil data and parameters

Soil engineering properties evaluations took place at different sites (BH-001, BH-002, BH-003) found inside the Amata Smart City Chonburi Phase 2 development. The project site rests upon a soft clay layer which extends from 10 to 14 meters below the ground surface, as the yellow section shows in Figure 3, indicating the subsurface conditions.

For numerical analysis, the soil layers were classified as follows: the weathered crust layer, with a thickness of 1.50 meters, was identified from 0.00 to -1.50 meters; the soft clay layer, with a thickness of 10.00 meters, was found between -1.50 and -11.50 meters; the medium clay layer, with a thickness of 3.00 meters, was observed from -11.50 to -14.50 meters; and the stiff clay layer, with a thickness of 11.50 meters, was present from -14.50 to -26.00 meters.

The input parameters for finite element modeling were based on previously validated values from a nearby project with similar subsoil characteristics, where calibration against long-term field data was successfully performed Malai et al., 2022 [23]. The researchers applied the soft soil model to simulate the soft and stiff clay layers. The analysis employed the Mohr-Coulomb Model to simulate soil behavior using parameters from Table 1. Long-term settlement was evaluated using coupled consolidation analysis, simulating mechanical deformation and time-dependent pore water pressure dissipation in the soil.

For the Soil Cement Columns (SCC), concrete pavement slabs, and asphalt concrete layers, the Linear Elastic Model was adopted, with material parameters referenced from a reliable study on the intercity highway connecting Highway No. 7 and Bang Na-Trat Highway [10, 23], which is geographically close to the project site.

The differential settlement was determined using Equation (1),

$$\Delta S = S_{center} - S_{corner} \quad (1)$$

where S_{center} and S_{corner} represent the settlement at the center and left edge of the roadway, respectively. The maximum settlement was observed at the center of the road, at X = 100 meters.

Table 1 Constitutive model parameters for each type of material.

Properties	Wea Crust	Soft Clay	Stiff Clay	Dense Sand	Fill Mat.
Model	MC	SS	SS	MC	MC
Type	D	U	U	D	D
γ_{unsat}(kN/m^3)	16	16	18	20	17
γ_{sat} (kN/m^3)	18	16.5	19	20	20
k_h(cm/d)	0.4	0.08	0.08	80	173
k_v(cm/d)	0.2	0.04	0.04	40	86
E(MPa)	5	-	-	100	40
n	0.25	0.30	0.25	0.25	0.25
λ^*	-	0.11	0.085	-	-
K^*	-	0.056	0.017	-	-
C'(kPa)	10	10	15	0	5
Ø′ (deg.)	12	8	30	39	31
OCR	-	1.2	1.65	-	-
k_o	0.65	0.75	0.65	0.37	-
f_a(kPa)	10	39	60	-	-

MC = Mohr Coulomb as yield criteria,
SS = Soft Soil Model, D=Drained, U= Undrained

Simulation Process

The simulation started by calculating initial stress conditions through the coefficient of earth pressure at rest (K_0) value for each soil stratum. The simulation of embankment construction proceeded by adding 2.5 meters of fill material distributed in successive layers of 50 centimeters each. The road structure followed the construction design by including key components for base course, subbase layer [15], pavement, and soil cement columns using the parameters outlined in Table 2.

This study did not explicitly model dynamic traffic effects such as cyclic loading and vibration. The traffic load of 10 kN/m² was modeled as a static uniform load to approximate the long-term average loading effect, a common simplification in consolidation settlement analysis. A 30-year operational simulation occurred while applying a traffic load onto the pavement surface. The research evaluated three models consisting of (1) No Cement Columns (NCC) that excluded soil cement stabilizations, (2) Soil Cement Columns (SCC) employed as load-bearing features, (3) Improved

DOI: 10.60101/jarst.2024.260742

Subgrade Material (ISM) strengthened the weathered crust layer to enhance its stiffness properties. The Elastic Modulus values of the enhanced material in the ISM case were changed between 5 MPa and 800 MPa. Based on preliminary analysis, variations in other constitutive model parameters had negligible effects on the embankment's total and differential settlements. Therefore, only the elastic modulus of the ISM was varied during the sensitivity analysis, while other parameters, including those of the Weathered Crust layer, were kept constant.

A comparison of settlement values and differential settlement between three construction approaches occurred after 30 years of road operation gave information about their long-term performance.

RESULTS AND DISCUSSION

Improved subgrade material (ISM)

Figure 4 illustrates the relationship between The Elastic Modulus of the Improved Subgrade Material (ISM) and settlement values. An increased Elastic Modulus value results in continuous settlement reduction. The settlement values decrease notably throughout the pressure range from zero to four hundred MPa. Beyond 500 MPa Elastic Modulus value the settlement reduction rate becomes slower, and additional material strength increases will not produce considerable settlement reduction benefits.

The blue dashed line shows that the differential settlement quantity decreases when the Elastic Modulus value increases. The data shows that differential settlement decreases intensively during the Elastic Modulus range from 0-200 MPa. The effectiveness of differential settlement reduction experiences decreased performance while the Elastic Modulus remains between 400 MPa and 800 MPa. Under laboratory conditions, the Elastic Modulus of ISM is the main controlling factor for settlement and differential settlement reduction through its elevated values.

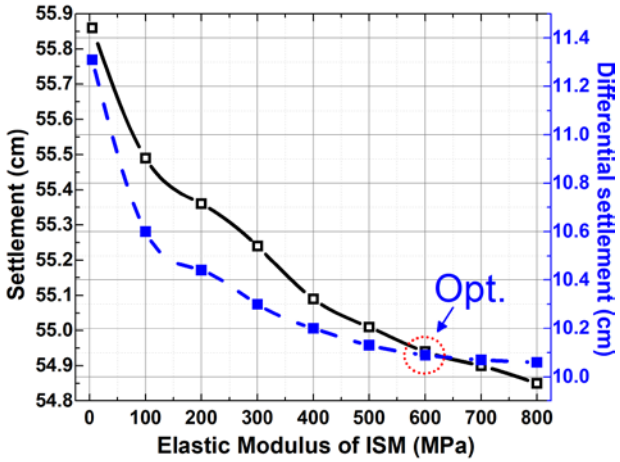

Figure 4 Comparison of Elastic Modulus with Differential Settlement and Maximum Settlement of the Road.

Table 2 Details of Structural Modelling in FEM Analysis.

Type of Structure	Model	Thickness/Diameter (m)	Unit Weight (kN/m^3)	E, (kPa)
Asphalt concrete	P	0.05	5	2.5×10^6
Concrete Pavement	MC	0.15	24	2.4×10^7
Base	MC	0.15	20	6.6×10^4
Sub Base	MC	0.15	20	2.5×10^4
Soil Cement Column	EP	0.60	8	3.6×10^5

P = Plate, EP = Embedded pile

Beyond an Elastic Modulus exceeding 600 MPa the settlement reduction effectiveness becomes marginal because the additional stiffness will not enhance the performance substantially.

The optimal value (Optimal Point, Opt.) was identified at approximately 600 MPa. The optimum point is determined at the intersection of the two curves, representing a balance between differential settlement reduction and control of total settlement. At this modulus, the analysis indicated a 12.28% reduction in differential settlement and a 1.75% reduction in total settlement. Emphasis is placed on the reduction of differential settlement, as it is considered more critical to the structural performance and long-term serviceability of the road. The Differential Settlement Ratio, which represents the degree of road deflection, is expressed in Equation (2).

$$\Delta S_{ratio} = \frac{\Delta S}{Span(L)} \quad (2)$$

When Span (L) represents the width of the road, which in this study is 19 meters.

The ΔS_{ratio} is found to be 1/190. Even with further improvements in soil stiffness, no significant benefits in settlement reduction are observed. Therefore, the Elastic Modulus of ISM should be selected at the optimal value (600 MPa) to effectively reduce both settlement and differential settlement while avoiding unnecessary cost increases.

The road displacement testing involved three scenarios, which included testing with soil cement columns (SCC) and without soil cement columns (NCC) alongside testing with improved subgrade material (ISM) that used an Elastic Modulus set to 600

DOI: 10.60101/jarst.2024.260742

MPa as shown in Figure 4. Analysis of the settlement patterns revealed that the red line representing SCC data demonstrated the smallest distance between points in all investigated road areas, thus proving its potential for settlement reduction. Within the 90 - 100 meter area, the NCC case (black dashed line) demonstrated the largest displacement because this section included the road center, where significant settlement occurred. Irregular patterns combined with fluctuating movements characterized the displacement results in the NCC case.

The damaged structures in the blue line ISM case showed equivalent settlement patterns to NCC yet displayed enhanced stability, proving that ISM soil improvement methods outperformed unenhanced NCC soil foundations.

ISM treatment of existing soil is a practical solution for controlling differential settlement in areas with soft soil. ISM offers cost-effective road maintenance through its budget-friendly solution with stable roadway conditions against SCC standards. ISM represents a suitable option when cost reduction stands as a primary requirement. The analysis presented in this study exists only as an initial evaluation but needs further evaluation to determine long-term settlement risks. A complete geotechnical investigation with a thorough design for the road structures must be performed to determine appropriate site-specific solutions.

Characteristics of road settlement

Three road conditions were examined through displacement evaluations in Figure 5, including SCC, where soil cement columns existed, and NCC, which had no soil cement columns, and ISM with an Elastic Modulus set to 600 MPa. The analysis results show that Soil Cement Columns (red line) delivered the minimum displacement of the road surface through all sections, thus confirming their effectiveness in reducing settlement. Soil cement columns (black dashed line) produced the maximum settlement result that peaked within the 90-100 meter zone, corresponding to the road center where significant subsidence happened. The displacement patterns in the NCC case showed mixed and unpredictable results throughout the experiment.

The case using improved soil by ISM (blue line) displayed displacement behaviors similar to those of NCC but achieved higher stability, demonstrating that soil modification from ISM helped lower settlement differences over NCC since NCC lacked any enhancement measures.

Using improved existing soil through ISM presents itself as a well-established method to reduce differential settlement in regions with soft soils. The road stability remains acceptable when this approach is used instead of SCC, and it generates cost savings. ISM proves to be a suitable, cost-efficient solution within projects requiring financial savings. The paper delivers initial analysis results, but further evaluations must be conducted to determine potential dangers related to long-term settlement behavior. A thorough geotechnical analysis and complete road design evaluations must be performed to determine site-appropriate solutions.

Although the effectiveness of soil cement columns (SCC) has been widely validated [1-13], limited studies have explored the feasibility of constructing roads on soft clay without SCC by strengthening the natural subgrade [15-17]. This research addresses the identified gap by evaluating settlement behavior.

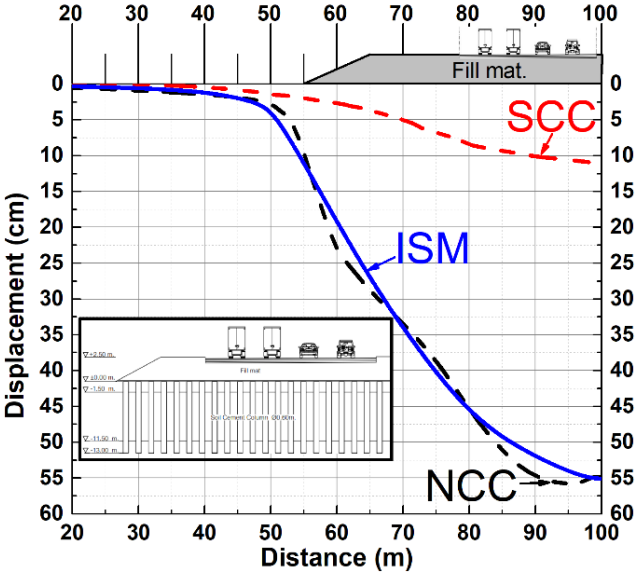

Figure 5 Road displacement comparison between cement deep mixing piles (SCC), no cement deep mixing piles (NCC), and Improved Subgrade Material (ISM) under alternative subgrade improvement strategies.

Long-term settlement of the road

A 30-year operational period revealing the road settlement is presented in Figure 6. The road structure received its maximum settlement of 11 centimeters within the center, while its minimum settlement of 3 centimeters occurred at the edge of the embankment after 30 years in operation.

The maximum settlement for the ISM case developed at the center of the road increased from 30 to 55 centimeters throughout 3, 5, 10, 20, and 30 years of operation. The ground experienced a 5-centimeter yearly increase in settlement throughout the initial 3 to 10 years. The settlement rate from years 20 to 30 steadily declined before reaching a stable position.

A clear difference exists between the settlement patterns of SCC and ISM because of the variations in differential settlement behavior. Overall, the settlement remains better in the SCC design, yet the ISM design experiences higher levels of settlement.

Road structure deterioration becomes less likely due to improved soil quality, which increases stability

DOI: 10.60101/jarst.2024.260742

and reduces unacceptable differential ground settlements. The selection of soil improvement techniques needs careful assessment between cost expenses and structural stability factors to match the site conditions for environmental and geotechnical needs.

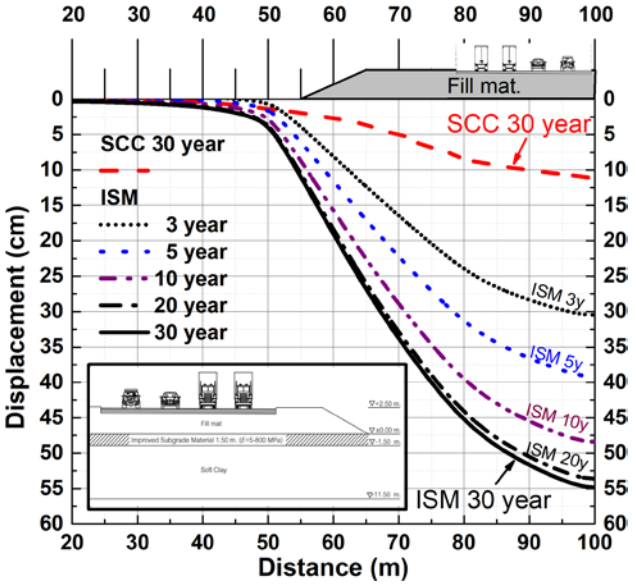

Figure 6 Road displacement comparison between soil cement columns (SCC) and improved subgrade material (ISM) over a 30-year operational period.

CONCLUSIONS

The study investigated settlement patterns of road structures built on soft clay sections within the Amata Smart City Chonburi Phase 2 Industrial Estate. The research followed a two-step approach by analyzing (1) SCC-supported roads and comparing them with (2) NCC-supported roads. The study assessed existing soil layer improvement (ISM) as a substitute for boosting soil strength and decreasing differential settlement. The research results demonstrate the following essential points:

1. The settlement rate of roads without soil cement column support (NCC) was five times higher than that of roads with SCC support, with the maximum settlement occurring at the center of the road.
2. Improving the existing soil layer (ISM) by increasing the elastic modulus (Elastic Modulus) showed that the optimal value for minimizing both settlement and differential settlement was 600 MPa, which provided the most effective results.
3. The long-term settlement behavior analysis indicated that the SCC-supported road structure exhibited a maximum settlement of approximately 11 cm at the center of the road. In contrast, the ISM-supported road structure experienced a maximum settlement of 55 cm over 30 years.
4. The trend of differential settlement demonstrates that greater settlement reduction is achieved in roads supported by SCC, whereas higher settlement is observed in roads utilizing ISM.

The research evidence demonstrated that soil cement columns (SCC) proved to be the most optimal approach to minimize road settlement problems while upholding structural integrity. Improving existing soil layer (ISM) is a practical substitute that lowers construction expenditures. The present investigation serves as a preliminary assessment thus, more analysis of settlement risks needs additional investigation. A complete geotechnical assessment and road structure design work must be carried out to confirm compatibility with local site conditions. Furthermore, this study considers only a static uniform traffic load. Future research should incorporate dynamic traffic effects, including cyclic loading and vibrations, to gain deeper insights and more accurately assess both short-term and long-term settlement behavior. Additionally, advanced constitutive models such as the Soft Soil Creep (SSC) are recommended to capture time-dependent behavior better.

ACKNOWLEDGEMENT

The authors express gratitude to the Department of Civil Engineering, Faculty of Engineering, Rajamangala University of Technology Rattanakosin, Salaya Campus, for providing facilities, equipment, and instruments in support of this research.

REFERENCES

1. Phetket K, Tangboontem P. The use of soil cement columns in Bangkok soft clay. Khao Chang. 1993; 254:41-7.
2. Sricharoen C, Rachan R, Horpibulsuk S. Development of strength in soil cement columns and soil cement-fly ash columns in Bangkok soft clay. KMUTT Res Dev J. 2014;2:151-63.
3. Hungwattanakul N. Study on the design of roads on Bangkok and metropolitan soft soil [master's thesis]. Bangkok: Kasetsart University; 2000.
4. Srijan A, Gupta AK. Sustainable material as a column filler in soft clay bed reinforced with encased column: numerical analysis. Sci Rep. 2025;15:1-13. doi:10.1038/s41598-025-12345-6.
5. Hoy M, Srijaroen C, Horpibulsuk S, Phunpeng V, Rachan R, Arulrajah A. Innovative solution: soil cement column walls as a temporary retaining structure for excavation in soft Bangkok clay. Smart Constr Sustain Cities. 2023;1:1-19. doi:10.1016/j.scs.2023.100001.
6. Abed AA, Korkiala-Tanttu L, Forsman J, Koivisto K. 3D simulations of deep mixed columns under

DOI: 10.60101/jarst.2024.260742

road embankment. Rakenteiden Mekaniikka. 2021;54(1):1-20. doi:10.23998/rm.84590.

7. Nguyen TN, Nguyen HH. Using finite element method to analyze stability of road foundation on soft ground reinforced by SDCM columns. IOSR J Mech Civ Eng. 2023;20:57-61. doi:10.9790/1684-2001055761.
8. Wang YN, Qin HR, Zhao LS. Full-scale loading test of jet grouting in the artificial island-immersed tunnel transition area of the Hong Kong–Zhuhai-Macau sea link. Int J Geomech. 2023;23(2):05022006. doi:10.1061/(ASCE)GM.1943-5622.0002280.
9. Wang YN, Peng JR, Kou XQ, Qin HR, Zhao LS. Improved settlement calculation method for offshore sand compaction pile based on measurements of the Hong Kong-Zhuhai-Macau Bridge. Int J Geomech. 2025;25(5):05025002. doi:10.1061/(ASCE)GM.1943-5622.0002676.
10. Yanto FH, Purwana YM, Surjandari NS. Finite element method (FEM) of rigid pavement laid on soft soil stabilized with soil cement column. Appl Mech Mater. 2016;845:83-8. doi:10.4028/www.scientific.net/AMM.845.83.
11. Junhirun J. Behavior of roads on soft soil improved with cement columns: Case study on Highway No. 34 (Bang Na-Chonburi) [master's thesis]. Bangkok: King Mongkut's University of Technology Thonburi; 2000.
12. Opakulwong P, Chaiyaphut S, Khongsombun T. Study on soil cement column reinforcement for sheet pile walls using finite element method. Proc 26th Natl Civ Eng Conf; 2021. p. GTE-13-1-GTE-13-8.
13. Bozkurt S, Abed A, Karstunen M. Finite element analysis for a deep excavation in soft clay supported by lime-cement columns. Transp Geotech. 2023;162:1-19. doi:10.1016/j.trgeo.2023.100162.
14. Department of Highways, Pavement Material Inspection and Advisory Group. Soil cement mix design. Bur Anal Insp Dep Highw. 2021
15. Wongkhan K, Boonrat K, Traisuth C. Improvement of recycled concrete aggregate quality using hydraulic cement for pavement materials. In: Proceedings of the 27th National Civil Engineering Conference; 2022. p. MAT17-1-MAT17-6.
16. Saroglou H. Compressive Strength of Soil Improved with Cement. In: International Foundation Congress and Equipment Expo 2009; 2009 Mar; Orlando, FL. Reston, VA: American Society of Civil Engineers; 2009. doi:10.1061/41023(337)37.
17. Tan EH, Zahran EMM, Tan SJ. A comparative experimental investigation into the chemical stabilisation of sandstone aggregates using cement and styrene-butadiene copolymer latex for road sub-base construction. Transp Geotech. 2022;37:1-14. doi:10.1016/j.trgeo.2022.100837.
18. Jintarakam K, Mahasuwanchai P, Watcharasawe K, Athisakul C, Jongpradit P, Leelataweewat S. 3D Laser Scanning Technology and Finite Element Method for Thai Ancient Masonry Fort: A case study of Mahakarn Fort. Proc 25th Natl Civ Eng Conf; 2020. p. STR10-1-STR10-9.
19. Watcharasawe K, Jongpradist P, Kitiyodom P, Matsumoto T. Measurements and analysis of load sharing between piles and raft in a pile foundation in clay. Geomech Eng. 2021;24(6):559-72. doi:10.12989/gae.2021.24.6.559.
20. Watcharasawe K, Kitiyodom P, Jongpradist P. 3-D numerical analysis of consolidation effect on piled raft foundation in Bangkok subsoil condition. Int J Geomate. 2017;12:105-11. doi:10.21660/2017.31.171202.
21. Watcharasawe K, Kitiyodom P, Jongpradist P. Numerical analyses of piled raft foundation in soft soil using 3D-FEM. Geotech Eng J SEAGS AGSSEA. 2015;46(1):109-16.
22. Roeun D, Sukkarak R, Likitlersuang S. Influences of subsoil modeling on underground deep excavation behavior in Phnom Penh City, Cambodia. Int J Geosynth Ground Eng. 2024;10:27. doi:10.1007/s40891-024-00534-6.
23. Malai A, Youwai S, Watcharasawe K, Jongpradist P. Bridge approach settlement mitigation using expanded polystyrene foam as light backfill: case study and 3D simulation. Transp Geotech. 2022;35:1-13. doi:10.1016/j.trgeo.2022.100747.
24. Rukdeechuai T, Jongpradist P, Wonglert A, Kaewsri T. Influence of soil models on numerical simulation of geotechnical works in Bangkok subsoil. Res Dev J. 2009;20:17-28.
25. Bentley Systems Inc. PLAXIS 3D 2024.2 Reference Manual, Bentley Systems, 2024.

Received: March 12, 2025 | Revised: April 28, 2025 | Accepted: May 16, 2025

JOURNAL OF APPLIED RESEARCH ON SCIENCE AND TECHNOLOGY
JARST
INSTITUTE OF RESEARCH AND DEVELOPMENT
RAJAMANGALA UNIVERSITY OF TECHNOLOGY THANYABURI
ISSN ONLINE: 2773-9473
https://ph01.tci-thaijo.org/index.php/rmutt-journal

Electrospun PLA/PBS/MWCNT nanocomposite fibers for high-performance air filtration: A sustainable approach

Manisara Phiriyawirut*, Prin Wangtanapat, Apiwit Chanthanchumpunon and Ratchanon Phanchaweng

Department of Tool and Materials Engineering, Faculty of Engineering, King Mongkut's University of Technology Thonburi, Bangkok 10140, THAILAND

*Corresponding author: manisara.pee@kmutt.ac.th

ABSTRACT

For the development of high-performance air filtration materials, electrospun polylactic acid (PLA)/polybutylene succinate (PBS) blend fibers, reinforced with multi-walled carbon nanotubes (MWCNTs), were fabricated and subjected to comprehensive characterization. A PLA/PBS blend, at a 95/5 wt% ratio, was prepared through the dissolution of the constituent polymers in a dichloromethane/dimethylformamide mixture, using a 3:1 v/v ratio at a 17 wt% concentration. MWCNTs were introduced into the polymer solution, with dispersion facilitated by a Triton X-100 surfactant and ultrasonication, at concentrations ranging from 0 to 4 wt%. Electrospinning was performed under optimized conditions, specifically an applied voltage of 16 kV and a tip-to-collector distance of 18 cm. Upon the incorporation of MWCNTs, minor alterations to fiber morphology were observed, including a slight increase in fiber diameter and an enhancement in the uniformity of surface pore distribution. Thermal properties were analyzed, revealing a trend of decreasing glass transition temperature, melting temperature, and thermal stability as the MWCNT content increased. Mechanical properties were evaluated, with improvements in tensile strength and Young's modulus documented with increasing MWCNT content. Filtration efficiency was assessed, and significant enhancements were achieved, with performance comparable to N95 masks (98-99%) recorded. Notably, a reduction in pressure drop across the filters was observed with increasing MWCNT content, indicating improved breathability. The potential of these biodegradable and environmentally sustainable nanocomposite fibers as an alternative to conventional filtration materials, addressing the growing concerns surrounding air pollution, is demonstrated by these results. This study highlights the feasibility of employing biopolymers and carbon nanomaterials for a more sustainable approach to air filtration, offering a viable solution for developing advanced, eco-friendly filtration technologies.

Keywords: Electrospinning, Polylactic acid, Polybutylene succinate, Multi-wall carbon nanotube, Filtration

INTRODUCTION

Human health is increasingly jeopardized by air pollution, with fine particulate matter (PM2.5) being a primary concern. Respiratory diseases, cardiovascular issues, and even cancer have been linked to PM2.5 exposure [1]. The urgent need for effective air filtration technologies, as emphasized by the World Health Organization (WHO), is crucial for mitigating these health risks [2]. Conventional filtration materials, such as surgical masks and N95 respirators, offer some protection. However, their reliance on non-biodegradable materials and potential limitations in filtration efficiency, breathability, and long-term sustainability have been noted [3].

As a versatile technique, electrospinning has emerged for the fabrication of nanofibrous membranes across diverse applications, including filtration [4-6]. The high surface area-to-volume ratio and interconnected porous structure inherent in electrospun nanofibers have been observed to be advantageous for capturing fine particulate matter [7]. Numerous studies have explored the capabilities of electrospun nanofibers for air filtration [8]. For example, nanofibers made from polymethyl methacrylate (PMMA) and ethylene vinyl alcohol (EVOH) were fabricated for biofiltration applications, demonstrating excellent filtration efficiency and low pressure drop [9]. Furthermore, polylactic acid (PLA) nanofibers were investigated for air filtration, with their biodegradable nature highlighted as a potential replacement for traditional materials [10].

Biodegradable polymers, notably PLA and polybutylene succinate (PBS), have been considered as promising materials for developing environmentally friendly filtration membranes [11-12]. While PLA offers biodegradability and filtration efficiency, its brittleness and relatively large pore sizes have been acknowledged [13]. Blending PLA with PBS has been shown to mitigate these limitations by improving

DOI: 10.60101/jarst.2024.261054

mechanical properties and processability. The effects of varying PLA/PBS blend compositions on electrospun fiber properties were studied, revealing a decrease in fiber diameter and an increase in crystallinity upon PBS addition [14]. Additionally, the miscibility of PLA/PBS blends was investigated, with phase separation behavior found to be influenced by blend composition and processing conditions [15]. The compatibility between PLA and PBS, and their ability to form miscible blends, has been well-established [16].

The incorporation of nanomaterials into electrospun polymer matrices has been observed to enhance membrane properties [17-19]. Carbon nanotubes (CNTs), particularly multi-walled carbon nanotubes (MWCNTs), have attracted attention due to their unique properties. MWCNTs are known for their exceptional mechanical properties, electrical conductivity, and high aspect ratio, which have been shown to improve filtration efficiency and mechanical strength in composite membranes. Furthermore, the dispersion of MWCNTs within the polymer solution during electrospinning can be improved by the incorporation of MWCNTs, leading to more uniform fibers [20-21]. The influence of MWCNTs on electrospun polyurethane (PU) fiber properties was investigated, showing that MWCNTs affected PU crystallinity and improved nanofiber properties [22]. Gas barrier properties of electrospun PLA/PBS blend fibers were also investigated, with MWCNTs improving barrier properties, especially for smaller gas molecules [23].

The improvement of mechanical properties and filtration performance of electrospun nanofibers by MWCNTs has been extensively studied [24-26]. However, MWCNT dispersion within the polymer matrix remains challenging due to strong van der Waals interaction. To address this, surfactants have been employed. The effectiveness of nonionic surfactants in MWCNT dispersion in epoxy composites was demonstrated, with Triton X-100 showing significant effectiveness [27]. Similarly, the use of Triton X-100 was reported to significantly improve CNT dispersion in polyvinyl pyrrolidone (PVA) solutions [28].

Significant research has been conducted on the biocompatibility of CNT-polymer composites for various biomedical applications, such as tissue engineering scaffolds and drug delivery systems [29]. These studies often demonstrate that when CNTs are well-dispersed and embedded within a biocompatible matrix, they can exhibit acceptable biocompatibility profiles with minimal cytotoxic effects.

This research investigates the fabrication and characterization of electrospun PLA/PBS nanocomposite fibers reinforced with multi-walled carbon nanotubes (MWCNTs) for high-performance air filtration applications. To facilitate MWCNT dispersion, Triton X-100 is employed. The influence of MWCNT content on fiber morphology, thermal characteristics, mechanical behavior, and filtration performance is systematically evaluated. The development of biodegradable air filtration materials exhibiting high performance is anticipated to contribute to sustainable solutions for air pollution mitigation.

MATERIALS AND METHODS

Materials

For the preparation of nanocomposite fibers, the following materials were utilized: Polylactic acid (PLA), specifically the 042D grade, was obtained from NatureWorks LLC. Polybutylene succinate (PBS), identified as BioPBS FZ91PM grade, was provided by PTT MCC BIOCHEM CO., LTD. Multi-walled carbon nanotubes (MWCNTs) were sourced from Nano Generation Co., Ltd. To facilitate MWCNT dispersion, the surfactant Triton X-100 (Polyoxyethylene octyl phenyl ether) was acquired from Alfa Aesar. Dimethylformamide (DMF) and dichloromethane (DCM) solvents were procured from RCI Labscan Limited.

Polymer solution preparation

A solvent mixture, consisting of dichloromethane (DCM) and dimethylformamide (DMF) in a 3:1 volumetric ratio, was prepared. Polylactic acid (PLA) and polybutylene succinate (PBS) were individually dissolved in this mixed solvent at a concentration of 17 wt%. PLA was dissolved at 100°C, while PBS was dissolved at 150°C. Both solutions were subjected to continuous stirring for 24 hours to ensure complete dissolution. Subsequently, the PLA and PBS solutions were combined at a weight ratio of 95:5 and stirred for an additional 24 hours at 100°C. To enhance MWCNT dispersion, Triton X-100 surfactant was added to the PLA/PBS solution at a 1 wt% concentration and stirred for 20 minutes at 100°C. Varying concentrations of MWCNTs (0, 1, 2, 3, and 4 wt%) were then incorporated into the solution and stirred for 24 hours at 100°C. To achieve a homogeneous dispersion of MWCNTs, the resultant solutions were subjected to high-intensity ultrasonication at frequency of 50-60 Hz for 5 minutes.

Electrospinning process

Electrospinning was employed to fabricate the nanofibers. The prepared polymer solutions containing varying concentrations of MWCNTs (0, 1, 2, 3, and 4 wt%) were loaded into a syringe pump and fed through a stainless-steel needle. A high voltage of 16 kV was applied between the needle tip and a grounded collector, which was placed 18 cm away. The electrospinning process was conducted at room temperature.

Characterization

Viscosity and electrical conductivity: The viscosity of the polymer solutions was determined using a Brookfield DV-III ULTRA rotational viscometer, while the electrical conductivity of the solutions

DOI: 10.60101/jarst.2024.261054

JOURNAL OF APPLIED RESEARCH ON SCIENCE AND TECHNOLOGY

was measured using a Hach HQD HQ40d conductivity meter. Both measurements were conducted at room temperature.

Morphology: The surface morphology of the electrospun fibers was examined using a JEOL JSM-6610 LV scanning electron microscope (SEM). Prior to imaging, samples were sputter-coated with a thin layer of gold to enhance electrical conductivity. Fiber diameter and pore size were subsequently determined from the SEM micrographs using ImageJ software.

Crystal structure: The crystalline structure of the electrospun fibers was analyzed by X-ray diffraction (XRD) using a Bruker axx D8 DISCOVER diffractometer. XRD patterns were obtained within a 2θ range of 5° to 55° to identify crystalline phases present in the samples.

Thermal properties: Thermal properties of the electrospun fibers were evaluated using differential scanning calorimetry (DSC, NETZSCH DSC 204 F1 Phoenix) and thermogravimetric analysis (TGA, NETZSCH TG 209 F3 Tarsus). DSC measurements, conducted under a nitrogen atmosphere at a heating and cooling rate of 10°C/min within a temperature range of -60 to 230°C with a nitrogen flow rate of 50 mL/min, determined the glass transition temperature (Tg), melting temperature (Tm), and degree of crystallinity. Thermal stability was assessed using TGA, performed under a nitrogen atmosphere at a heating rate of 10 °C/min from 25 to 600°C with a nitrogen flow rate of 20 mL/min.

Mechanical properties: Tensile strength of the electrospun fibers was measured according to ASTM D882-02 using a TA.XT plus C universal testing machine.

Filtration Performance Testing: The filtration efficiency of the electrospun PLA and PLA/PBS/MWCNT composite fibers was determined using a TSI DustTrak 8533 aerosol monitor. Di-ethyl-hexyl-sebacate (DEHS) particles, with a size range of 0.2 to 0.3 micrometers, were generated using an ATM226 aerosol generator. Circular filter samples, 6 cm in diameter and 0.15 ± 0.5 mm in thickness, were placed in a custom-built test rig. The airflow rate through the filter was maintained at 4 liters per minute. The filtration efficiency (η) was calculated based on the upstream and downstream particle concentrations measured by the DustTrak monitor and was determined using equation 1. Here, C_{left} represents the concentration of particles upstream of the filter and C_{right} represents the concentration downstream. The pressure drop across the filter (ΔP) was determined by measuring the change in water level in a manometer connected to the filter holder (ΔH) using equation 2. The filtration efficiency and pressure drop of the electrospun fibers were then compared to those of commercial N95 and surgical masks.

$$\eta = \frac{C_{left} - C_{right}}{C_{left}} \times 100\% \quad (1)$$

$$\Delta P = \frac{101{,}325\ \text{Pa} \times \Delta H}{10\ \text{m}H_2O} \quad (2)$$

RESULTS AND DISCUSSION

Viscosity of Polymer Solutions

Solution viscosity, a critical parameter influencing electrospinning behavior, was measured at room temperature using a rotational viscometer. The viscosity of the 17 wt% PLA solution was determined to be 36.48 ± 0.2 cP, as presented in Table 1. A slight reduction in viscosity, to 33.8 ± 0.1 cP, was observed upon the incorporation of PBS into the PLA solution. This minor decrease is attributed to the enhanced compatibility between the PLA and PBS polymers. It is suggested that the introduction of PBS may have led to a slight disruption in the PLA chain entanglements, thereby lowering the overall resistance to flow. This observation is consistent with previous studies that have documented the improved miscibility of PLA and PBS blends, leading to a more homogeneous solution.

Table 1 Viscosity and electrical conductivity of pure PLA. Pure PBS, PLA/PBS and PLA/PBS/MWCNT solutions.

Sample	Viscosity (cP)	Electrical Conductivity (μS/cm)
PLA	36.5 ± 0.2	1.96 ± 0.01
PBS	N/A	1.55 ± 0.01
PLA/PBS	33.8 ± 0.1	2.59 ± 0.01
PLA/PBS/MWCNT-1	35.3 ± 0.0	97.5 ± 0.01
PLA/PBS/MWCNT-2	38.7 ± 0.2	231 ± 0.01
PLA/PBS/MWCNT-3	44.6 ± 0.2	332 ± 0.01
PLA/PBS/MWCNT-4	51.6 ± 0.2	382 ± 0.01

A noticeable increase in solution viscosity was recorded upon the incorporation of multi-walled carbon nanotubes (MWCNTs). Specifically, the viscosity of the PLA/PBS/MWCNT solutions was found to range from 35.2 ± 0.1 cP to 51.58 ± 0.2 cP, with the variation directly corresponding to the MWCNT content. This increase in viscosity is attributed to the development of a three-dimensional network within the solution. This network formation is believed to be facilitated by the high aspect ratio and substantial surface area characteristics of MWCNTs. The increased interactions between the MWCNTs, PLA, and PBS molecules, including van der Waals forces and π-π interactions, are thought to contribute to viscosity enhancement. These results are consistent with findings reported in previous investigations [23], where it was demonstrated that the introduction of MWCNTs into polymer solutions led to an increase in viscosity, presumably due to the creation of a more entangled polymer network. It is

DOI: 10.60101/jarst.2024.261054

JOURNAL OF APPLIED RESEARCH ON SCIENCE AND TECHNOLOGY

suggested that the increased viscosity directly impacts the electrospinning process, possibly leading to changes in fiber morphology and uniformity.

Electrical conductivity of polymer solutions

Electrical conductivity measurements were performed on the prepared polymer solutions at room temperature, with the exception of the PBS solution, for which measurements were taken at 50°C to prevent solidification. The conductivity values obtained for PLA, PBS, PLA/PBS, and PLA/PBS/MWCNT solutions are presented in Table 1.

A conductivity of 1.96 ± 0.01 µS/cm was measured for the PLA solution, while the PBS solution exhibited a slightly lower conductivity of 1.55 ± 0.01 µS/cm. An increase in conductivity to 2.59 ± 0.01 µS/cm was observed upon blending PLA with PBS. The increase in conductivity observed upon blending PLA with PBS can be attributed to several factors related to the miscibility and interaction between the two polymers, as well as the potential presence of ionic impurities within each polymer that become more mobile or concentrated at the interface upon blending. However, the most significant enhancement in electrical conductivity was achieved with the incorporation of MWCNTs. The conductivity of the PLA/PBS/MWCNT solutions ranged from 97.5 ± 0.01 to 382 ± 0.01 µS/cm, dependent upon the MWCNT content.

This substantial increase in conductivity is believed to be the result of a conductive network formed within the polymer matrix. The MWCNTs, acting as conductive fillers, facilitate electron transport, thereby enhancing the overall conductivity of the composite. It is suggested that this finding aligns with previous research [30], where a similar increase in electrical conductivity was reported upon the addition of MWCNTs to polymer matrices. The formation of a conductive network was likely aided by the high aspect ratio of the MWCNTs and their ability to create interconnected structures within the polymer blend.

Morphology of electrospun fibers

The visual appearance of the electrospun fibers is presented in Figure 1. A white, opaque appearance was observed for the electrospun PLA fibers, suggesting a structure that appeared dense and possibly non-porous to the naked eye. The PLA/PBS blend fibers displayed a similar visual morphology to the pure PLA fibers. However, with the introduction of MWCNTs, a noticeable color change was observed. The fiber mats transitioned from a white hue to a dark gray, with the intensity of the gray coloration becoming progressively more pronounced as MWCNT content was increased. This gradual darkening was taken as a clear visual indication of the successful incorporation and increasing concentration of MWCNTs within the PLA/PBS polymer matrix.

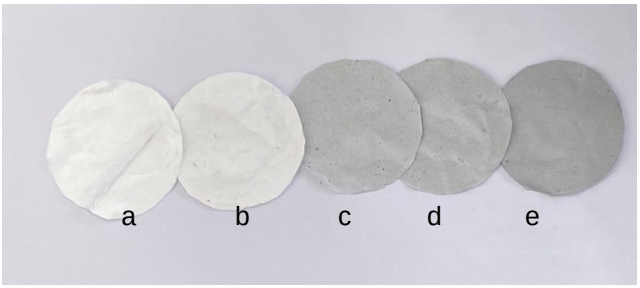

Figure 1 Visual appearance of electrospun fibers: (a) Pure PLA, (b) PLA/PBS, and PLA/PBS/MWCNT composites with varying MWCNT concentrations: (c) 1 wt%, (d) 2 wt% and (e) 3 wt%.

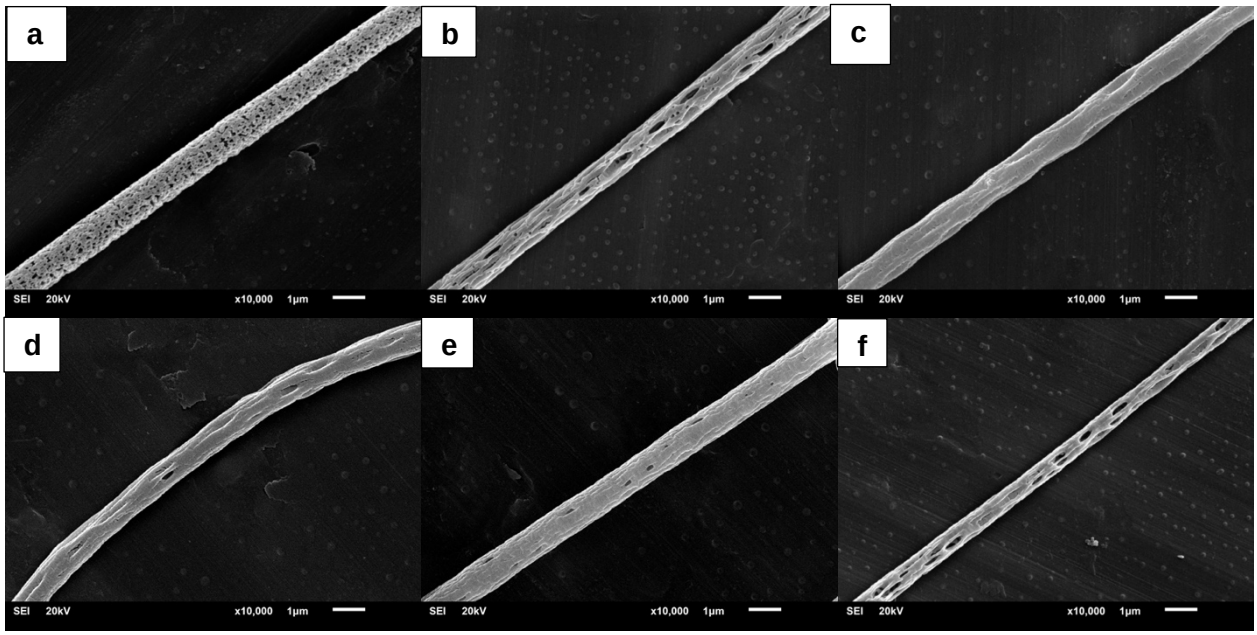

Figure 2 SEM images of electrospun fibers: (a) Pure PLA, (b) PLA/PBS, and PLA/PBS/MWCNT composites with varying MWCNT concentrations: (c) 1 wt%, (d) 2 wt%, (e) 3 wt%, and (f) 4 wt%. Scale bar: 1 µm.

DOI: 10.60101/jarst.2024.261054

JOURNAL OF APPLIED RESEARCH ON SCIENCE AND TECHNOLOGY

It should be clarified that, owing to challenges encountered in detaching the fiber mat containing 4 wt% MWCNT from the aluminum foil substrate without significant damage, XRD analysis, mechanical property evaluation, and filtration performance testing could not be performed on this specific composition. This strong adhesion may be attributed to an enhanced interaction between the MWCNTs and the substrate, potentially resulting from a combination of significant Van der Waals forces arising from the extensive contact area and mechanical interlocking of the nanofiber network with the aluminum foil's surface. Furthermore, due to the high melting temperature and crystallinity of PBS, the electrospinning of pure PBS fibers proved challenging under the chosen processing conditions. Consequently, the morphology of pure PBS fibers was not investigated in this study.

Distinct morphological features of the electrospun PLA, PLA/PBS, and PLA/PBS/MWCNT fibers were observed through scanning electron microscopy (SEM) and are presented in Figure 2. Pure PLA fibers, as imaged, displayed a characteristic bead-on-string morphology, punctuated by micro-sized pores. The formation of these pores is believed to be a consequence of rapid solvent (DCM/DMF) evaporation during the electrospinning process. Upon blending PLA with PBS, a morphology similar to pure PLA was noted, though pores with slightly elongated shapes were evident. The increased flexibility imparted by PBS to the PLA matrix is thought to have facilitated this elongation.

A notable impact on fiber morphology was observed with the incorporation of MWCNTs into the PLA/PBS blend. MWCNTs appeared to function as nucleation sites, promoting the formation of more uniform and well-defined pores. With increasing MWCNT content, the pore distribution along the fiber surface became increasingly uniform, and the pores themselves exhibited greater elongation. This behavior is attributed to the improved mechanical properties of the composite fibers, which are thought to have allowed them to withstand greater stretching forces during electrospinning. Furthermore, the increased viscosity of the polymer solution, a result of MWCNT addition, is believed to have contributed to the formation of finer and more uniform fibers. These morphological changes are consistent with findings reported in previous studies, where the introduction of nanofillers has been shown to significantly influence electrospun fiber morphology [31].

It was found that the MWCNTs are typically embedded and physically entrapped within the polymer matrix (PLA/PBS in this case). This strong physical integration significantly limits the potential for the release of free CNTs during normal use of the filter. The polymer acts as a binder, effectively immobilizing the nanofiller.

The average fiber diameter and diameter distribution for the PLA and PLA/PBS/MWCNT composite fibers, as determined from SEM images, are summarized in Table 2. Pure PLA fibers exhibited an average diameter of 669 nm. The addition of PBS to the PLA matrix resulted in a decrease in the average fiber diameter to approximately 390 nm. This reduction in fiber diameter can be attributed to the improved processability of the PLA/PBS blend, which is likely due to the enhanced compatibility between the two polymers.

Table 2 Fiber morphology and diameter distribution of electrospun pure PLA, PLA/PBS, and PLA/PBS/MWCNT fibers.

Sample	SEM image (500x)	Diameter distribution	Average diameter (nm)
PLA	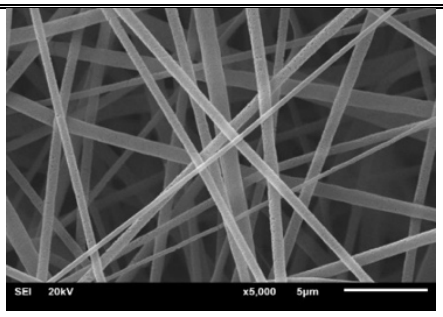	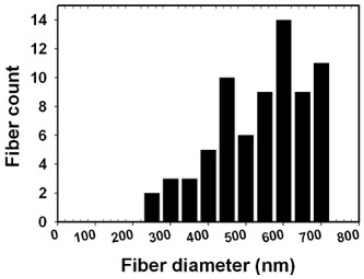	669±270
PLA/PBS	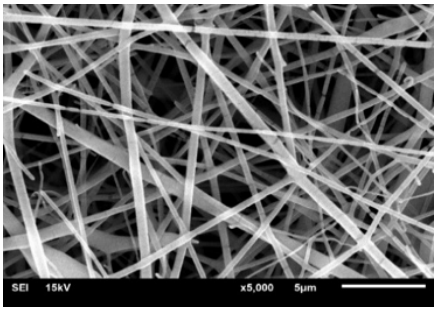	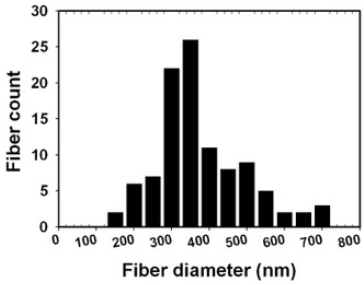	390±180

DOI: 10.60101/jarst.2024.261054

Sample	SEM image (500x)	Diameter distribution	Average diameter (nm)
PLA/PBS/MWCNT-1	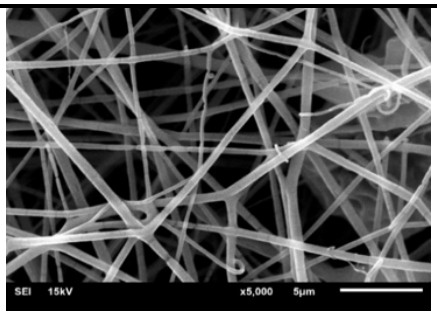	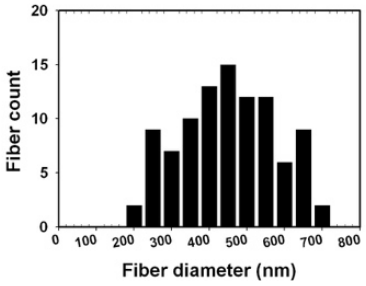	440±140
PLA/PBS/MWCNT-2	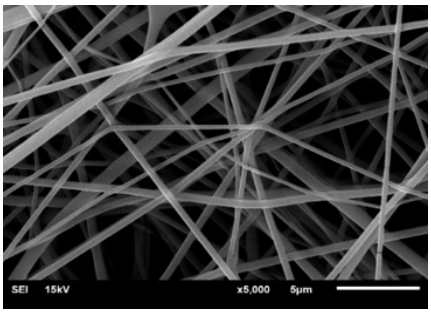	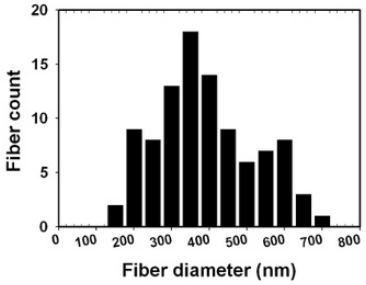	430±240
PLA/PBS/MWCNT-3	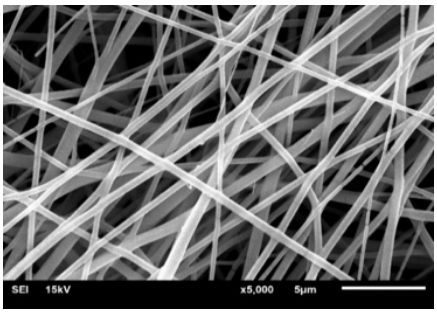	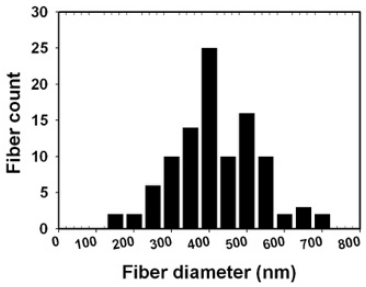	420±160
PLA/PBS/MWCNT-4	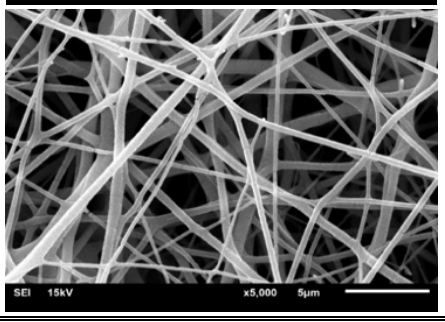	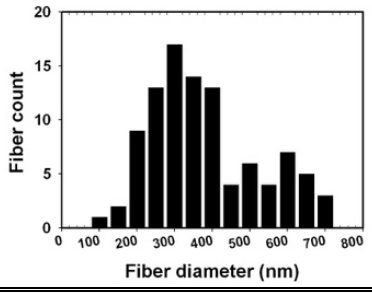	370±210

* Electrospinning conditions: 16 kV, 18 cm tip-to-collector distance, 90 min spinning time.

The sample designation "PLA/PBS/MWCNT-x" indicates the weight percentage concentration of multi-walled carbon nanotubes (MWCNTs) within the PLA/PBS blend. For instance, the notation "PLA/PBS/MWCNT-1" denotes an MWCNT concentration of 1 wt%.

Upon incorporation of MWCNTs, a slight increase in diameter was detected when compared to the pure PLA/PBS blend, despite an observed increase in solution viscosity. This seemingly contradictory result can be attributed to the interplay between viscosity and electrical conductivity. While an elevated viscosity is generally understood to yield thicker fibers, the enhanced electrical conductivity imparted by MWCNTs has been shown to facilitate the formation of thinner fibers. This is due to an increase in Coulombic repulsion and electrostatic forces within the electrospinning jet. This phenomenon, where competing forces influence fiber diameter, has been documented in prior research [32]. The final fiber diameter, therefore, is determined by the equilibrium established between these opposing forces.

Furthermore, a trend toward a slight decrease in average fiber diameter was noted at higher MWCNT loadings. This reduction can be rationalized by the formation of a more conductive network within the polymer matrix. This network, in turn, facilitates the elongation of the Taylor cone during the electrospinning process, resulting in the production of thinner fibers. This observation aligns with findings reported by Xin and Chen [33], wherein a similar trend was observed

DOI: 10.60101/jarst.2024.261054

during the electrospinning of polysulfonamide (PSA) solutions containing MWCNTs. The established conductive network allows for the efficient transfer of charge, increasing the stretching force applied to the jet.

Crystal structure analysis

The crystalline structure of the electrospun fibers was examined through X-ray diffraction (XRD) analysis. Illustrated in Figure 3 illustrates the obtained XRD patterns for pure PLA, PBS, and the PLA/PBS/MWCNT composite fibers.

A characteristic peak at 2θ = 16.9° was observed in the XRD pattern of pure PLA, correlating with the crystalline structure of PLA as documented in prior research [34]. Similarly, peaks at 2θ = 19.5 and 22.5° were identified in the XRD pattern of pure PBS, aligning with findings from previous PBS studies [34]. A distinct peak at 2θ = 25.7°, associated with the (002) plane of the graphitic structure, was recorded for the MWCNTs [35].

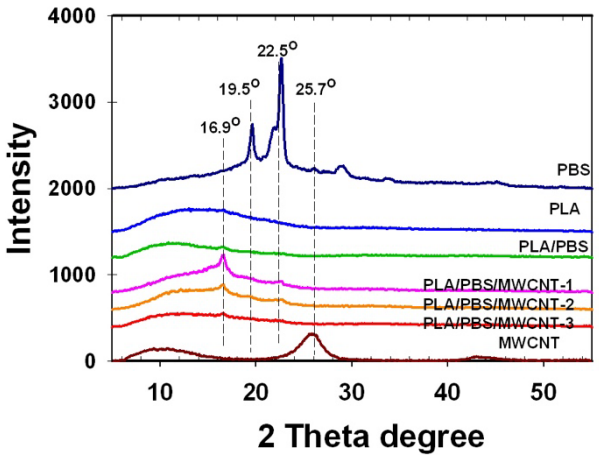

Figure 3 XRD patterns of MWCNT, electrospun pure PLA, pure PBS, PLA/PBS and PLA/PBS/MWCNT fibers.

Within the PLA/PBS/MWCNT composite fibers, the presence of the characteristic PLA peak at 2θ = 16.9° was confirmed. A slight increase in the intensity of this PLA peak was noted with the addition of 1 wt% MWCNTs, suggesting a slight enhancement in PLA crystallinity. However, as MWCNT content was further increased, a reduction in the PLA peak intensity was observed, indicating a decrease in crystallinity. This phenomenon is thought to stem from the nucleation effect of MWCNTs. At lower MWCNT concentrations, the MWCNTs appear to function as nucleation sites, facilitating PLA crystallization. Conversely, at elevated concentrations, the MWCNTs may impede polymer chain mobility, thereby limiting overall crystallinity. This behavior bears resemblance to the results presented by Xin and Chen [33], where a decrease in polysulfonamide fiber crystallinity was reported with increasing MWCNT content.

Thermal properties

The thermal behavior of the electrospun fibers was examined using differential scanning calorimetry (DSC), with key thermal transitions shown in Figure 4 and summarized in Table 3.

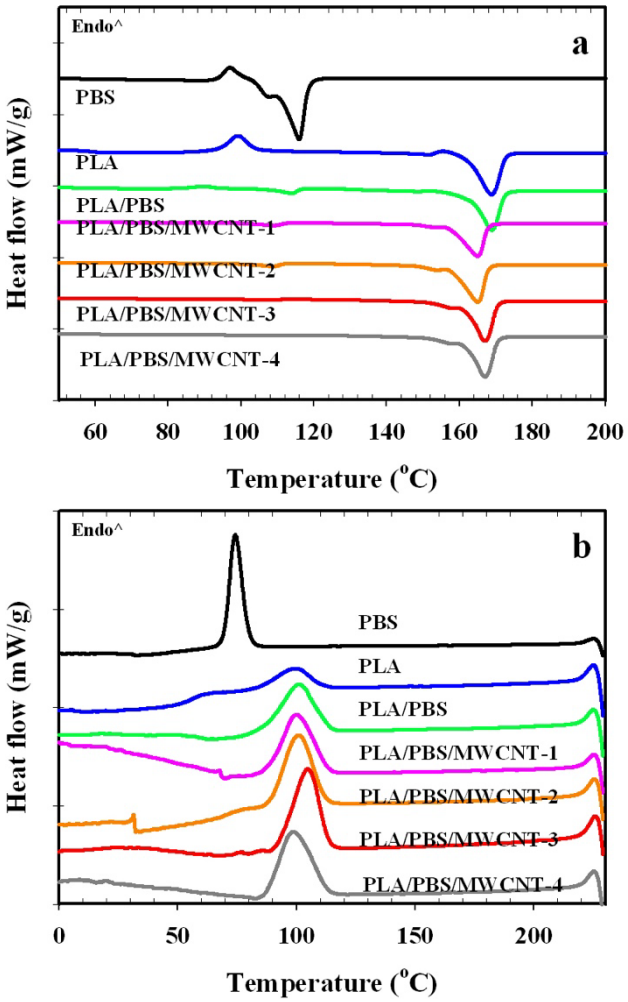

Figure 4 DSC thermogram of electrospun pure PLA, pure PBS, PLA/PBS and PLA/PBS/MWCNT fibers. (a) Heating scan and (b) Cooling scan.

The glass transition temperature (T_g) of PLA was determined to be 62.3°C. Conversely, a distinct T_g for PBS was not discernible within the measured temperature range. This absence is consistent with the reported low T_g of PBS, which is -31.2°C [14]. A single T_g, observed at 62°C, was recorded for the PLA/PBS blend, indicating good miscibility between the two polymers. This single T_g value was found to be in agreement with findings by Phiriyawirut et al. [14], who also reported a single T_g for PLA/PBS blends. It should be noted that while Phiriyawirut et al. observed a decrease in T_g with increasing PBS content, no such decrease was observed in the present study. This discrepancy is likely attributable to the low PBS content (5 wt%) used. However, the addition of MWCNTs to the PLA/PBS blend resulted in a decrease in T_g. This trend aligns with observations made by Yuen [36], who reported a decrease in T_g with

DOI: 10.60101/jarst.2024.261054

increasing MWCNT content in polyimide composites. Yuen attributed this reduction to the non-polar nature of MWCNTs, which, when incorporated, weakens interactions with the polymer matrix. This weakening is thought to lead to increased free volume and, consequently, enhanced mobility of the polymer chains.

The crystallization temperature (T_c) was measured at 99.6°C for PLA and 74.2°C for PBS. For the PLA/PBS blend, the T_c of PLA was observed at 101.1°C. The incorporation of MWCNTs into the PLA/PBS blend did not appear to significantly alter the T_c of PLA, with values ranging from 98.6 to 104.8°C. The T_c of PBS was not detected in the blends, likely due to its low concentration.

The melting temperature (T_m) of PLA was 159.5°C, and that of PBS was 103.8°C. The PLA/PBS blend showed two T_m values, one at 108.2°C corresponding to PBS and the other at 158.5°C corresponding to PLA. The addition of MWCNTs to the PLA/PBS blend resulted in a decrease in both T_m values, shifting to 102.6°C for PLA and 152°C for PBS. This decrease in T_m is consistent with the findings of Chow et al. [37], who reported a similar decrease in T_m for PLA/PP electrospun fibers with the addition of MWCNTs. They attributed this phenomenon to the high thermal conductivity of MWCNTs, which can act as nucleating agents and facilitate heat distribution within the fibers, leading to a reduction in the melting temperature.

The crystallinity of the electrospun fibers was investigated using DSC. Pure PLA fibers exhibited a crystallinity of 50.70%, while PBS fibers showed a crystallinity of 34.26%. The PLA/PBS blend fibers had a crystallinity of 51.19%, indicating that the addition of PBS did not significantly alter the crystallinity of PLA in the blend. This result differs from the findings reported by Phiriyawirut et al. [14], who observed an increase in PLA crystallinity in PLA/PBS blends due to the nucleating effect of PBS. They also noted a tendency for decreased crystallinity with increasing PBS content. The nucleating effect of PBS on PLA crystallinity, as reported by Phiriyawirut et al. [14], is strongly dependent on the interfacial interactions between the constituent polymers. These interactions can be influenced by the molecular weight of both components. Variations in molecular weight could lead to differences in the degree of mixing, phase morphology, and the nature of the interface, consequently affecting the effectiveness of PBS as a nucleating agent for PLA. Therefore, despite a potentially similar blend ratio, the differing molecular weights of the PLA and PBS components between this study and that of Phiriyawirut et al. [14] likely play a crucial role in the observed discrepancies in PLA crystallinity within the blend. Chain mobility, interfacial interactions, and the effectiveness of PBS as a nucleating agent for PLA are all influenced by molecular weight.

Table 3 Thermal transition temperatures and crystallinity of electrospun pure PLA, pure PBS, PLA/PBS and PLA/PBS/MWCNT fibers.

Sample	T_g (°C)	T_c (°C)	T_m (°C)		ΔH_m (J/g)		X_c (%)	
			PBS	PLA	PBS	PLA	PBS	PLA
PLA	62.3	99.6	-	159.5	-	47.51	-	50.70
PBS	-	74.2	103.8	-	68.52	-	34.26	-
PLA/PBS	62	101.1	108.2	158.5	4.48	50.5	0.11	51.19
PLA/PBS/MWCNT-1	58.2	100.1	102.6	152	2.93	59.2	0.06	59.19
PLA/PBS/MWCNT-2	53.5	100.8	100.6	146	3.17	41.89	0.04	41.57
PLA/PBS/MWCNT-3	53.1	104.6	101.3	148	3.88	49.01	0.03	48.12
PLA/PBS/MWCNT-4	56.4	98.6	96	151	1.21	52.03	0.01	50.53

The addition of MWCNTs at 1 wt% increased the crystallinity of the PLA/PBS blend to 59.19%. This increase in crystallinity with the addition of 1 wt% MWCNTs can be explained by the nucleating effect of MWCNTs. This observation is consistent with the research by Ceregatti [38] on the thermal and electrical properties of PLA/CNT composites, where the percentage of PLA crystallinity increased with increasing MWCNT content. Ceregatti attributed this increase to the higher concentration of nanoparticles providing a greater number of nucleation sites. MWCNTs act as heterogeneous nucleation sites, accelerating the crystallization of PLA.

However, further increasing the MWCNT content from 1 wt% to 4 wt% in the PLA/PBS blend led to a decrease in crystallinity. This decrease at higher MWCNT loadings is likely due to the agglomeration of MWCNTs, which hinders their ability to act as effective nucleating agents. The observed agglomeration at 4 wt% MWCNT suggests that the combination of the Triton X-100 concentration and the ultrasonication conditions employed may not have been sufficient to effectively overcome strong inter-nanotube attractions and maintain a stable, well-dispersed state at this higher loading. Consequently, improved dispersion at higher MWCNT loadings might necessitate a higher surfactant concentration, optimized ultrasonication

DOI: 10.60101/jarst.2024.261054

parameters (e.g., higher power, longer duration, pulsed sonication), or the incorporation of a different or additional dispersing agent. The observed decrease in crystallinity with increasing MWCNT content in this DSC study is also consistent with the XRD results, where the intensity of the PLA peak at 2θ = 16.9° decreased with increasing MWCNT content. This correlation between DSC and XRD data further supports the conclusion that MWCNT dispersion plays a crucial role in influencing the crystallinity of the PLA/PBS/MWCNT composite fibers. Ghane et al. [39] also found a similar trend in their work on electrospun polyamide-6/MWCNT nanocomposite fibers and films, where the enthalpy of melting (ΔH_m), and thus the degree of crystallinity (X_c) increased with increasing MWCNT content up to a certain point, beyond which further increases in MWCNT led to a decrease in crystallinity. This was attributed to the role of MWCNTs as nucleating agents at lower concentrations, promoting the formation of ordered 3D structures around their axes, while at higher concentrations, agglomeration hinders this effect.

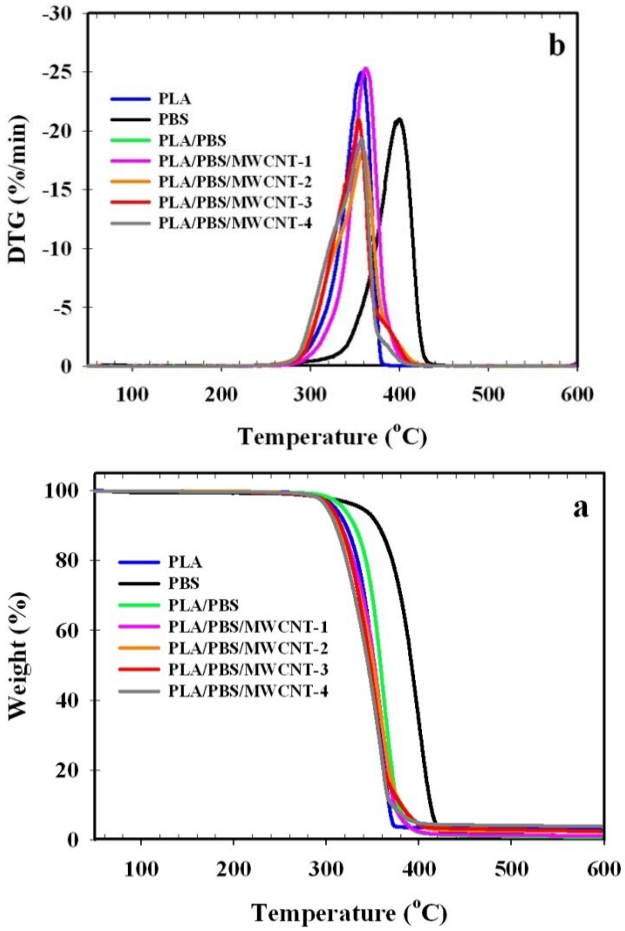

Figure 5 TGA analysis of electrospun pure PLA, pure PBS, PLA/PBS and PLA/PBS/MWCNT fibers. (a) TGA thermogram and (b) DTG thermogram.

The thermal stability of the electrospun fibers was evaluated through thermogravimetric analysis (TGA), as shown in Figure 5. For each sample, the onset degradation temperature (T_{onset}) and maximum degradation temperature (T_{max}) were determined. These values, along with the percentage weight loss, are presented in Table 4 for electrospun PLA, PBS, and PLA/PBS blends containing varying MWCNT loadings.

Table 4 Thermal degradation behavior of electrospun pure PLA, pure PBS, PLA/PBS and PLA/PBS/MWCNT fibers.

Sample	T_{onset} (°C)	T_{max} (°C)	Weight loss (%)
PLA	330.2	357.2	97.15
PBS	371.8	400.0	98.99
PLA/PBS	339.1	361.8	99.30
PLA/PBS/MWCNT-1	331.8	360.1	98.77
PLA/PBS/MWCNT-2	322.5	359.5	97.54
PLA/PBS/MWCNT-3	327.2	353.8	97.52
PLA/PBS/MWCNT-4	321.4	357.4	96.08

It was observed that pure PLA exhibited a T_{onset} of 330.2°C, while PBS displayed a higher T_{onset} of 371.8 °C. The PLA/PBS blend, however, showed a T_{onset} of 339.1°C. This increase in T_{onset} compared to pure PLA indicates that the addition of PBS contributed to an improvement in the thermal stability of PLA. A similar trend was noted for the T_{max} values, where an increase was observed with the addition of PBS to PLA.

These observations are consistent with previous findings. For instance, Vorawongsagul et al. [40] examined the thermal properties of 80/20 PLA/PBS blends. They reported T_{onset} values of 362°C for PLA and 400°C for PBS. Their study revealed a two-stage degradation process in the PLA/PBS blends, with the first stage attributed to the thermal degradation of PLA and the second stage associated with the decomposition of PBS. In the present study, however, a single degradation step was observed for the PLA/PBS blend. This difference may be attributed to the relatively low PBS content (5 wt%) used, which might not have been sufficient to clearly delineate both degradation stages. The lower PBS content likely resulted in an overlapping degradation profile, making the two distinct stages less apparent.

Within the tested temperature range, no significant degradation of the multi-walled carbon nanotubes (MWCNTs) was observed. This observation aligns with the understanding that MWCNT degradation typically occurs around 800°C [37]. Upon the addition of MWCNTs to the polylactic acid (PLA)/polybutylene succinate (PBS) blend, a decrease in the onset degradation temperature (T_{onset}) was noted as MWCNT content increased. This finding is consistent with observations reported by Chow and Lim [37], who investigated PLA/polypropylene (PP)/MWCNT composites. They found a lowered degradation temperature for the PLA phase within the composites

DOI: 10.60101/jarst.2024.261054

compared to the PLA/PP blend. This reduction might be explained by the high thermal conductivity of MWCNTs, which can enhance heat transfer and accelerate polymer nanocomposite degradation, thereby lowering the activation energy for the process. Furthermore, given PLA's known susceptibility to thermal degradation, the presence of highly conductive MWCNTs may exacerbate this, enhancing heat dissipation.

A tendency for weight loss to decrease with increasing MWCNT loading was observed in the PLA/PBS blends. This trend suggests that higher MWCNT content contributes to an increase in residual char content post-combustion. This result is consistent with work by Eun et al. [41], who studied polyvinylidene fluoride (PVDF) nanofibers with MWCNTs. They reported a decrease in weight loss with increasing MWCNT content (2 to 10 wt%), attributed to the higher thermal stability of MWCNTs compared to PVDF.

The introduction of MWCNTs into the PLA/PBS blend resulted in a decreased T_{onset}, indicating a reduction in composite fiber thermal stability. This could be attributed to a catalytic effect of MWCNTs on polymer matrix thermal degradation. The high thermal conductivity of MWCNTs may facilitate heat transfer within the composite, accelerating degradation. Additionally, defects and impurities within MWCNTs could serve as initiation sites for thermal degradation.

An increase in composite fiber weight loss with increasing MWCNT content was also observed. This is likely due to the higher thermal stability of MWCNTs, which may act as a barrier, hindering the volatilization of polymer degradation products. Similar observations have been documented in the literature [37, 41].

Mechanical properties

The mechanical properties of the electrospun PLA, PLA/PBS, and PLA/PBS/MWCNT composite fibers were assessed through tensile testing, conducted in accordance with ASTM D882-02 standards. The resulting data, including tensile strength, elongation at break, and Young's modulus, are presented in Figure 6.

For the pure PLA fibers, a tensile strength of 0.42 MPa and a Young's modulus of 7.08 MPa were measured. Upon the introduction of PBS into the PLA matrix, a notable increase in both tensile strength and Young's modulus was observed, with values reaching 0.73 MPa and 8.27 MPa, respectively. This improvement can be attributed to the enhanced chain mobility within the polymer matrix, resulting from the plasticizing effect exerted by PBS. Additionally, a significant increase in elongation at break was recorded for the PLA/PBS blend when compared to pure PLA fibers.

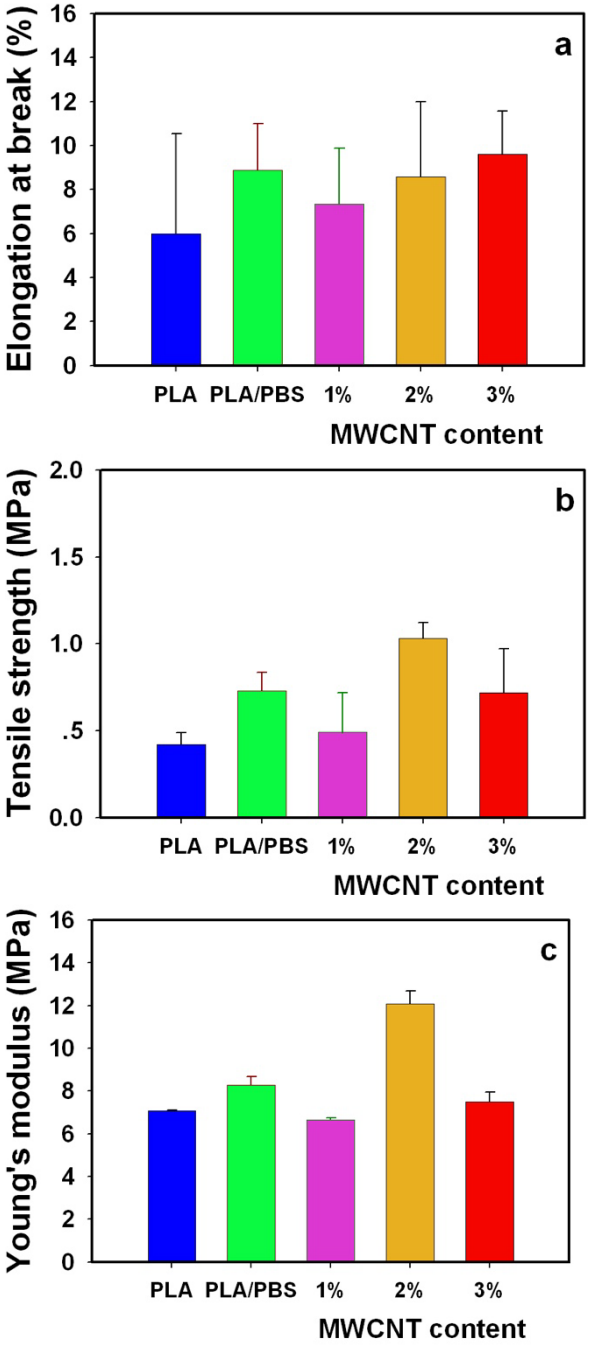

Figure 6 Tensile properties of electrospun pure PLA, PLA/PBS and PLA/PBS/MWCNT fibers (a) Elongation at break, (b) Tensile strength and (c) Young's modulus.

However, the addition of MWCNTs did not yield a statistically significant change in elongation at break. This observation differs from the findings reported by Badar et al. [23]. This discrepancy might be explained by variations in processing conditions, MWCNT loading, or the specific polymer matrix employed in the previous study. Further investigation into these parameters could provide a more comprehensive understanding of the observed differences.

Tensile strength and Young's modulus were evaluated to determine the mechanical performance of the composite fibers. The PLA/PBS blend exhibited

DOI: 10.60101/jarst.2024.261054

increased tensile strength and Young's modulus compared to pure PLA, consistent with enhanced interfacial adhesion between the PLA and PBS phases, as previously reported [14]. The incorporation of MWCNTs further increased the Young's modulus, indicating enhanced stiffness due to the formation of a more rigid, interconnected MWCNT network that restricts polymer chain deformation.

The influence of MWCNTs on tensile strength was less consistent, displaying variability with MWCNT loading. This behavior is attributed to competing effects of reinforcement and agglomeration. At lower loadings, MWCNTs acted as reinforcing agents, enhancing mechanical properties likely due to effective stress transfer at the MWCNT-polymer interface [23]. However, at higher loadings, MWCNT agglomeration led to stress concentrations and a reduction in tensile strength, a trend also observed by Islam et al. [42].

Filtration efficiency

Filtration efficiency of electrospun PLA, PLA/PBS, and PLA/PBS/MWCNT composite fibers was assessed using a TSI DustTrak 8533 aerosol monitor. Results were then compared with those obtained from commercial surgical masks and N95 respirators. As presented in Table 5, the electrospun fibers demonstrated exceptional filtration performance, reaching levels comparable to N95 masks. Average filtration efficiency for the electrospun fibers was found to range between 98% and 99%, a significant improvement over the 19.5-19.9% efficiency recorded for standard surgical masks.

Table 5 Filtration efficiency and pressure drop of surgical masks, N95 respirators, and electrospun pure PLA, PLA/PBS and PLA/PBS/MWCNT fibers.

Sample	Filtration efficiency (%)	Pressure drop (Pa)
Surgical masks	19.9±2.5	152±11.7
N95 respirators	98.6±0.0	304±58.5
Electrospun fibers		
PLA	99.1±0.2	709±58.5
PLA/PBS	99.2±0.2	1165±50.7
PLA/PBS/MWCNT-1	98.5±1.0	1064±155
PLA/PBS/MWCNT-2	99.1±0.1	963±163
PLA/PBS/MWCNT-3	99.2±0.1	760±183

The high filtration efficiency observed in the electrospun fibers is attributed to several factors. Firstly, a high surface area-to-volume ratio, characteristic of electrospun fibers, provides numerous sites for particle capture. Secondly, the small pore size within the fiber network effectively traps fine particles, including those in the submicron range. Thirdly, an interconnected fibrous network forms a multi-layered filtration barrier, which enhances capture efficiency. Lastly, the incorporation of MWCNTs provides additional sites for particle capture and improves the mechanical stability of the fibrous mat, further contributing to the enhanced filtration performance.

Breathability, as indicated by pressure drop across the filter materials, was assessed. The pressure drop values obtained for electrospun PLA/PBS/MWCNT composite fibers, alongside commercial surgical masks and N95 respirators, are presented in Table 5. Surgical masks were found to exhibit a pressure drop of 152 Pa, while N95 respirators demonstrated a range from 30 to 304 Pa. In contrast, the electrospun fibers showed pressure drop values ranging from 709 to 1165 Pa. These elevated values suggest that the developed PLA/PBS/MWCNT composite fibers, in their current state, may not be suitable for direct application in personal respiratory masks due to potentially compromised user comfort arising from excessive pressure drop.

The higher pressure drop observed for the electrospun fibers is thought to be a consequence of their denser and more tortuous structure when compared to the nonwoven fabrics utilized in commercial masks. The smaller pore sizes and increased fiber density inherent in electrospun mats are believed to contribute to a greater resistance to airflow, thereby resulting in the elevated pressure drop.

The influence of MWCNT addition on the PLA/PBS blend's pressure drop was shown to be multifaceted. While an increase in fiber diameter and a more elongated pore morphology, associated with increasing MWCNT content, might have been expected to reduce pressure drop, a consistent trend was not observed. This suggests that factors such as fiber orientation and the level of fiber entanglement may have played a significant role in determining the pressure drop.

It has been established in previous studies that fiber morphology, including fiber diameter, pore size distribution, and fiber orientation, can significantly affect the airflow resistance of nonwoven fabrics [43]. Generally, smaller fiber diameters and a narrower pore size distribution are associated with higher pressure drops. However, the complex interactions between these factors, coupled with the unique characteristics of the electrospun fibers, make it challenging to accurately predict the precise relationship between fiber morphology and pressure drop.

CONCLUSIONS

This study successfully fabricated and characterized electrospun PLA/PBS composite fibers reinforced with MWCNTs for high-performance air filtration. The incorporation of MWCNTs enhanced electrical conductivity, mechanical strength, and filtration efficiency. Notably, increased polymer solution viscosity with 1-3 wt% MWCNT led to a slight

DOI: 10.60101/jarst.2024.261054

increase in fiber diameter, while a decrease at 4 wt% MWCNT suggests that the dominant effect of increased electrical conductivity at higher loadings can overcome viscosity, promoting finer fiber formation. The electrospun fibers' high porosity and surface area contributed to excellent filtration, further improved by MWCNTs acting as capture sites and stabilizing the fiber structure. Thermal analysis revealed MWCNT influences on crystallization and stability, with low concentrations acting as nucleating agents and high concentrations hindering chain mobility. Mechanical property improvements, particularly tensile strength and Young's modulus were also observed with MWCNT addition.

Based on processability for large-scale production, optimal fiber morphology, comparable filtration efficiency across all MWCNT loadings, and improved breathability with increasing MWCNT content, our novel finding indicates that a 2 wt% MWCNT loading in the electrospun PLA/PBS blend presents the most cost-effective balance for high-performance air filtration. This composition offers good fiber formation, desirable morphology, effective filtration, and enhanced breathability while minimizing material costs associated with higher MWCNT concentrations.

Future research should optimize MWCNT dispersion and loading for further performance enhancement and explore long-term stability and potential in other applications such as water purification and biomedical devices.

Declaration of AI and AI-Assisted Technologies in the Writing Process

The authors utilized Gemini to improve the legibility and clarity of the text during the preparation of this work. The authors assume full responsibility for the content of the publication and review and edit the content as necessary after using this tool/service.

ACKNOWLEDGEMENT

The experimental results reported in this study are part of the undergrad senior project, Department of Tool and Materials Engineering, Faculty of Engineering, King Mongkut's University of Technology Thonburi (KMUTT). The authors gratefully acknowledge the financial support from the Thailand Science Research and Innovation (TSRI) under Fundamental Fund 2023 (Project: Advanced Materials and Manufacturing for Applications in New S-curve Industries).

REFERENCES

1. Sangkham S, Phairuang W, Sherchan SP, Pansakun N, Munkong N, Sarndhong K, et al. An update on adverse health effects from exposure to PM2.5. Environ Adv [internet]. 2024;18:100603. Available from: https://doi.org/10.1016/j.envadv.2024.100603.
2. Pai SJ. Carter TS, Heald CL, Kroll JH. Updated world health organization air quality guidelines highlight the importance of non-anthropogenic PM2.5, Environ Sci Technol Lett [internet]. 2022;9(6):501-6. Available from: http://doi.org/10.1021/acs.estlett.2c00203.
3. Selvaranjan K, Navaratnam S. Rajeev P, Ravintherakumaran N. Environmental challenges induced by extensive use of face masks during COVID-19: A review and potential solutions. Environ Challenges [internet]. 2021;3:100039. Available from: https://doi.org/10.1016/j.envc.2021.100039.
4. Villarreal-Gómez LJ, Cornejo-Bravo JM, Vera-Graziano R, Grande D. Electrospinning as a powerful technique for biomedical applications: A critically selected survey. J Biomater Sci Polym Ed [internet]. 2015;27(2);157-76. Available from: https://doi.org/10.1080/09205063.2015.1116885.
5. Phan DN, Khan MQ, Nguyen NT, Phan TT, Ullah A, Khatri M, et al. A review on the fabrication of several carbohydrate polymers into nanofibrous structures using electrospinning for removal of metal ions and dyes, Carbohydr Polym [internet]. 2021;252:117175. Available from: https://doi.org/10.1016/j.carbpol.2020.117175.
6. Dai H, Liu X, Zhang C, Ma K, Zhang Y. Electrospinning polyacrylonitrile/graphene oxide/polyimide nanofibrous membranes for high-efficiency PM2.5 filtration. Sep Purif Technol [internet]. 2021;276:119243. Available from: https://doi.org/10.1016/j.seppur.2021.119243.
7. Liu H, Zhu Y, Zhang C, Zhou Y, Yu DG. Electrospun nanofiber as building blocks for high-performance air filter: A review, Nano Today. 2024;55:102161. Available from: https://doi.org/10.1016/j.nantod.2024.102161.
8. Yu Z, Fan T, Liu Y, Li L, Liu J, Yang B, et al. Efficient air filtration through advanced electrospinning techniques in nanofibrous materials: A review. Purif Technol [internet]. 2024;349;127773. Available from: https://doi.org/10.1016/j.seppur.2024.127773.
9. Karabulut FNH, Höfler G, Ashok Chand N, Beckermann GW. Electrospun nanofibre filtration media to protect against biological or nonbiological airborne particles. Polym [internet]. 2021;13(19):3257. Available from: https://doi.org/10.3390/polym13193257.
10. Wang L, Gao Y, Xiong J, Shao W, Cui C, Sun N, et al. Biodegradable and high-performance multiscale

DOI: 10.60101/jarst.2024.261054

structured nanofiber membrane as mask filter media via poly(lactic acid) electrospinning. J Colloid Interface Sci [internet]. 2022;606;961-70. Available from: https://doi.org/10.1016/j.jcis.2021.08.079.

11. Wang Z, Zhao C, Pan Z. Porous bead-on-string poly(lactic acid) fibrous membranes for air filtration. J Colloid Interface Sci [internet]. 2015;441121-29. Available from: https://doi.org/10.1016/j.jcis.2014.11.041.
12. Souzandeh H, Wang Y, Netravali AN, Zhong WH. Towards sustainable and multifunctional air-filters: A review on biopolymer-based filtration materials. Polym Rev [internet]. 2019;59(4):651-86. Available from: https://doi.org/10.1080/15583724.2019.1599391.
13. Hamad K, Kaseem M, Ayyoob M, Joo J, Deri F. Polylactic acid blends: The future of green, Prog Polym Sci [internet]. 2018;85:83-127. Available from: https://doi.org/10.1016/j.progpolymsci.2018.07.001.
14. Phiriyawirut M, Sarapat K, Sirima S, Prasertchol A. Porous electrospun nanofiber from biomass-based polyester blends of polylactic acid and polybutylene succinate. OJPChem [internet]. 2019:9(1):1-15. Available from: http://doi.org/10.4236/ojpchem.2019.91001.
15. Stoyanova N, Paneva D, Mincheva R, Toncheva A, Manolova N, Dubois P, et al. Poly(l-lactide) and poly(butylene succinate) immiscible blends: From electrospinning to biologically active materials. Mater Sci Eng C [internet]. 2014;41:119-26. Available from: https://doi.org/10.1016/j.msec.2014.04.043.
16. Prahsarn C, Klinsukhon W, Padee S, Suwannamek N, Roungpaisan N, Srisawat N. Hollow segmented-pie PLA/PBS and PLA/PP bicomponent fibers: An investigation on fiber properties and splittability. J Mater Sci [internet]. 2016;51:10910–16. Available from: https://doi.org/10.1007/s10853-016-0302-0.
17. Ghosal K, Agatemor C, Špitálsky Z, Sabu T, Kny E. Electrospinning tissue engineering and wound dressing scaffolds from polymer-titanium dioxide nanocomposites. Chem Eng J [internet]. 2019;358:1262-78. Available from: https://doi.org/10.1016/j.cej.2018.10.117.
18. Canales D, Moyano D, Alvarez F, Grande-Tovar CD, Valencia-Llano CH, Peponi L, et al. Preparation and characterization of novel poly (lactic acid)/calcium oxide nanocomposites by electrospinning as a potential bone tissue scaffold. Biomater Adv [internet]. 2023;153:213578. Available from: https://doi.org/10.1016/j.bioadv.2023.213578.
19. Selatile MK, Ojijo V, Sadiku R, Ray SS. Development of bacterial-resistant electrospun polylactide membrane for air filtration application: Effects of reduction methods and their loadings. Polym Degrad Stab [internet]. 2020;178:109205. Available from: https://doi.org/10.1016/j.polymdegradstab.2020.109205.
20. Naebe M, Lin T, Staiger MP, Dai L, Wang X. Electrospun single-walled carbon nanotube/polyvinyl alcohol composite nanofibers: Structure-property relationships. Nanotechnol [internet]. 2008;19:305702. Available from: https://doi.org/10.1088/0957-4484/19/30/305702.
21. Kaur N, Kumar V, Dhakate SR. Synthesis and characterization of multiwalled CNT–PAN based composite carbon nanofibers via electrospinning. SpringerPlus [internet]. 2016;5:483. Available from: https://doi.org/10.1186/s40064-016-2051-6.
22. Zadeh ZE, Solouk A, Shafieian M, Nazarpak MH, Electrospun polyurethane/carbon nanotube composites with different amounts of carbon nanotubes and almost the same fiber diameter for biomedical applications. Mater Sci Eng C [internet]. 2021;118:111403. Available from: https://doi.org/10.1016/j.msec.2020.111403.
23. Alruwaill BM, Saeed U, Ahmad I, Al-Turaif H, Aboalkhair H, Alsaiarl AO. Development of multiwalled carbon nanotube-reinforced biodegradable polylactic acid/polybutylene succinate blend membrane. Membr [internet]. 2021;11(10):760. Available from: https://doi.org/10.3390/membranes11100760.
24. Tian X, Huang Y, Lu Y, Li Z, Liu L, Wang L, et al. Fabrication of an amino-modified MWCNTs grafted with chlorosulfonated PMIA nanofibrous membrane via electrospinning for efficient high-temperature dust filtration. Sep Purif Technol [internet]. 2024;336:126193. Available from: https://doi.org/10.1016/j.seppur.2023.126193.
25. Namsaeng J, Punyodom W, Worajittiphon P. Synergistic effect of welding electrospun fibers and MWCNT reinforcement on strength enhancement of PAN-PVC non-woven mats for water filtration. Chem Eng Sci [internet]. 2019;193:230-42. Available from: https://doi.org/10.1016/j.ces.2018.09.019.
26. Madenli EC, Cakmakci O. Preparation and characterization of PAN/CNT nanocomposite fiber supports for membrane filtration. Desalination Water Treat [internet]. 2017;60:137-43. Available from: https://doi.org/10.5004/dwt.2017.0808.
27. Ghorabi S, Rajabi L, Madaeni SS, Zinadini S, Derakhshan AA. Effects of three surfactant types

DOI: 10.60101/jarst.2024.261054

of anionic, cationic and non-ionic on tensile properties and fracture surface morphology of epoxy/MWCNT nanocomposites. Iran Polym J [internet]. 2012;21:121–30. Available from: https://doi.org/10.1007/s13726-011-0013-y.

28. Elsharif AM, Bukhari OA. Carbon nanofilms blended with polyvinyl pyrrolidone and Triton X-100 for energy harvesting application. Orient J Chem [internet]. 2020;36(3). Available from: http://dx.doi.org/10.13005/ojc/360306.

29. Pathak R, Punetha VD, Bhatt S, Punetha M, Carbon nanotube-based biocompatible polymer nanocomposites as an emerging tool for biomedical applications. Eur Polym J [internet]. 2023;196:112257. Available from: https://doi.org/10.1016/j.eurpolymj.2023.112257.

30. Khan W, Sharma R, Saini P. Carbon nanotube-based polymer composites: Synthesis, properties and applications [Internet]. Carbon Nanotubes - Current Progress of their Polymer Composites. InTech [internet]. 2016. Available from: http://doi.org/10.5772/62497.

31. Lee JKY, Chen N, Peng S, L Li, Tian L, Thakor N, et al. Polymer-based composites by electrospinning: Preparation & functionalization with nanocarbons. Prog Polym Sci [internet]. 2018;86:40-84. Available from: https://doi.org/10.1016/j.progpolymsci.2018.07.002.

32. Mit-uppatham C, Nithitanakul M, Supaphol, P. Ultrafine electrospun polyamide-6 fibers: Effect of solution conditions on morphology and average fiber diameter. Macromol Chem Phys [internet]. 2004;205:2327-38. Available from: https://doi.org/10.1002/macp.200400225.

33. Xin BJ, Chen W. Morphology, structure and properties of electrospun multi-walled carbon nanotube/polysulfonamide composite nanofibers. J Eng Fibers Fabr [internet]. 2015;10(1). Available from: http://doi.org/10.1177/155892501501000105.

34. Chaiwutthinan P, Pimpan V, Chuayjuljit S, Leejarkpai T. Biodegradable plastics prepared from poly(lactic acid), poly(butylene succinate) and microcrystalline cellulose extracted from waste-cotton fabric with a chain extender. J Polym Environ [internet]. 2015;23:114-25. Available from: https://doi.org/10.1007/s10924-014-0689-0.

35. Nie P, Min C, Song HJ, Chen X, Zhang Z, Zhao K. Preparation and tribological properties of polyimide/carboxyl-functionalized multi-walled carbon nanotube nanocomposite films under seawater lubrication. Tribol Lett [internet]. 2015;58:7. Available from: https://doi.org/10.1007/s11249-015-0476-7.

36. Yuen SM, Ma CCM, Chiang CL, Teng CC, Morphology and properties of aminosilane grafted MWCNT/polyimide nanocomposites. J Nanomater [internet]. 2008;786405. Available from: https://doi.org/10.1155/2008/786405.

37. Chow WS, Lim YT. Antistatic and thermal properties of poly(lactic acid)/polypropylene/carbon nanotube nanocomposites. J Eng Sci [internet]. 2020;16(2):57-69. Available from: http://doi.org/10.21315/jes2020.16.2.3.

38. Ceregatti T, Pecharki P, Pachekoski WM, Becker D, Dalmolin C. Electrical and thermal properties of PLA/CNT composite films. Rev Mater [internet]. 2017;22(3). Available from: http://doi.org/10.1590/S1517-707620170003.0197.

39. Ghane N, Mazinani S, Gharehaghaji A. Comparing the performance of electrospun and cast nanocomposite film of polyamide-6 reinforced with multi-wall carbon nanotubes. J Plast Film Sheeting [internet]. 2019;35(1):45-64. Available from: https://doi.org/10.1177/8756087918794229.

40. Vorawongsagul S, Pratumpong P, Pechyen C. Preparation and foaming behavior of poly (lactic acid)/poly (butylene succinate)/cellulose fiber composite for hot cups packaging application. Food Packag Shelf Life [internet]. 2021;27:100608. Available from: https://doi.org/10.1016/j.fpsl.2020.100608.

41. Eun JH, Sung SM, Kim MS, Choi BK, Lee JS. Effect of MWCNT content on the mechanical and piezoelectric properties of PVDF nanofibers. Mater Des [internet]. 2021;206:109785. Available from: https://doi.org/10.1016/j.matdes.2021.109785.

42. Islam MS, Ashaduzzaman M, Masum SM, Yeum JH. Mechanical and electrical properties: Electrospun alginate/carbon nanotube composite nanofiber. Dhaka Univ J Biol Sci [internet]. 2012;60(1):125-28. Available from: https://doi.org/10.3329/dujs.v60i1.10350

43. Xiao Y, Sakib N, Yue Z, Wang Y, Cheng S, You J, Militky J, Venkataraman M, Zhu G. Study on the relationship between structure parameters and filtration performance of polypropylene meltblown nonwovens. AUTEX Res J [internet]. 2020;20(4):366-71. Available from: https://doi.org/10.2478/aut-2019-0029.

DOI: 10.60101/jarst.2024.261054

Received: March 19, 2025 | Revised: May 6, 2025 | Accepted: May 14, 2025

JOURNAL OF APPLIED RESEARCH ON SCIENCE AND TECHNOLOGY
JARST
INSTITUTE OF RESEARCH AND DEVELOPMENT
RAJAMANGALA UNIVERSITY OF TECHNOLOGY THANYABURI
ISSN ONLINE: 2773-9473
https://ph01.tci-thaijo.org/index.php/rmutt-journal

Prototype inspection cart for detecting track geometry irregularities

Apisit Muanmuang, Pipat Pramot, Terdkiat Limpeteeprakarn and Manusak Janthong*

Department of Mechanical Engineering, Faculty of Engineering, Rajamangala University of Technology Thanyaburi, Pathum Thani 12120, THAILAND

*Corresponding author: manusak.j@en.rmutt.ac.th

ABSTRACT

This article presents the design and construction of a ride-on geometry inspection vehicle that is controlled by a joystick to measure the width and cross-level height of a model railway track with a gauge of 459 millimeters. The vehicle utilizes a rotary encoder combined with springs, linear guides, and rolling wheels as a measurement tool for the rail width. An Inertial Measurement Unit (IMU) is used to measure the tilt angle between the railway tracks for calculating the cross-level height. To ensure measurement accuracy, the sensors were calibrated with instruments that have been calibrated in accordance with ISO/IEC 17025 standards. The rotary encoder has a measurement deviation of 0.1 millimeters, and the IMU has an angular deviation of 0.05 degrees. During testing, different speeds of 0.1, 0.3, and 0.5 meters per second were evaluated. The average width measurement deviations were found to be 0.10, 0.04, and 0.13 millimeters, while the average cross-level height deviations were 0.09, 0.56, and 0.44 millimeters, respectively. Subsequently, an analysis was conducted to compare the differences in the average error values of the width and cross-level height measurements of the railway tracks using Analysis of Variance (ANOVA). The measured rail gauge values showed no significant differences, while the measured cross-level heights indicated significant differences at the 0.05 statistical level. It was found that the average measurement error for the geometric cross-level height of the railway tracks at a speed of 0.1 meters per second was lower than that at speeds of 0.3 meters per second and 0.5 meters per second, with errors of 0.14 millimeters and 0.17 millimeters, respectively.

Keywords: Cross level, Gauge, Track geometry, Railway tracks

INTRODUCTION

Currently, railways have rapidly evolved and become widely popular. In Thailand, there are two main types of trains [1] 1. Intercity trains: These use a meter-gauge track, with a total distance of 4,044 kilometers divided into various train routes [2]. 2.Electric trains there are two track gauges in use - the meter gauge, covering a distance of 41 kilometers, and the standard gauge, with a distance of 210 kilometers [3]. Railways are a crucial component of the infrastructure for train operations. Over time, the condition of railway tracks tends to deteriorate due to various factors. To ensure safe train operations, regular railway inspections are necessary. The Office of Transport and Traffic Policy and Planning [4] has developed a manual to guide the inspection, evaluation, and maintenance of railway infrastructure in Thailand. The manual includes assessment criteria, specifications, and maintenance guidelines in compliance with the Safety Standard for Working in Urban Passenger Heavy Rail Track (UPHR) S-T001-256x and UIC standards.

For railway inspection techniques, there are several methods, such as Anuwat Bumrungkit et al. [5] developed a mobile hydraulic parallel gauge to measure the rail gauge. The method involves increasing the pressure in the hydraulic cylinder until the rollers contact the rail surface and compress the springs. The experimental results showed a deviation of 0.89 mm. Qijin Chen and et al. [6] used the Amberg GRP1000 and Trimble GEDO CE trolley systems to survey rail gauge and cross-level. For greater accuracy, these tools were integrated with GNSS/INS technology, processed in dynamic mode using the Positioning and Navigation Data Analyst (PANDA) software developed by Wuhan University. Experimental results indicated improved accuracy, with Amberg GRP1000 measuring a cross-level deviation of ±5 mm during movement, which was reduced to ±1 mm when combined with GNSS/INS. Angular deviations were less than 0.01 degrees. Waldemar Odziemczyk and Marek Woźniak [7] tested single-wheel trolleys for detecting rail irregularities and compared their performance with dual-wheel trolleys to assess measurement errors. Wei Chen et al. [8], supported by Xinyun Engineering Co., Ltd., under China Railway First Group Co., Ltd., developed equipment to measure rails and analyze the geometry of subway tunnels. This device includes a laser

DOI: 10.60101/jarst.2024.260837

scanner, measure distance, angle sensor, and width measurement sensor. Experimental results showed that the laser scanner produced curves with average, maximum, and minimum errors of 0.14 mm, 0.3 mm, and 0 mm, respectively. The distance gauge accuracy was 5 mm for 5 meters and 10 mm for 15 meters. Width measurements had an average error of 0.073 mm and a maximum error of 0.23 mm. José L. Escalona et al. [9] developed the Track Geometry Measurement System (TGMS), a mobile system using laser scanners to project light onto the rail head and video cameras to capture images. The positional and directional data from the light line were combined with acceleration and angular velocity data from an Inertial Measurement Unit (IMU) to analyze track geometry irregularities. These included track alignment, vertical profile, cross-level, gauge, and twist measurements using non-contact technology.

This article presents the design and construction of a ride-on railway geometry inspection vehicle. The system consists of four main components. First, an Inertial Measurement Unit (IMU) sensor is used to measure tilt angles caused by cross-level differences in the railway tracks. Second, encoder sensors are employed to measure the rail gauge and the distance traveled. Third, a joystick control system is integrated to manage the vehicle's movement. Finally, a display and data recording system captures and stores data for analyzing rail geometry irregularities, such as gauge and cross-level measurements.

MATERIALS AND METHODS

1. Design of the vehicle chassis.

The design of the geometry inspection vehicle is intended for testing on a model railway track with a rail gauge of 459 millimeters, as this is the track size available in the Department of Mechanical Engineering and is required for testing. The structure of the geometry inspection vehicle is constructed from aluminum profiles measuring 30 x 30 millimeters. The vehicle itself measures 600 x 900 millimeters. For propulsion, the vehicle uses a brushless DC motor as the power source, with power transmitted from the motor to the wheels via a timing belt, as shown in Figure 1. In selecting the motor size for this research, the workload that the inspection vehicle must handle is defined as follows. The inspection vehicle can accommodate one operator and equipment, with a total weight of 200 kilograms. The model railway track used for testing is a flat track (no inclines). The inspection vehicle can travel at a maximum speed of no more than 1 meter per second.

2. The selection or design of a measurement system

The design of the measurement system for railway abnormalities follows the principles of measuring track gauge and cross level. The gauge is measured from the top surface of the rail down to 14 millimeters as the measurement point. Then, the distance between the left rail and the right rail is measured, as shown in Figure 3. The cross level is determined by measuring the angle formed by the two sides of the rail, which are not equal. This is then calculated in conjunction with the gauge width to obtain the cross level, as shown in Figure 1.

Figure 1 Model of the structure and equipment of the geometry inspection vehicle.

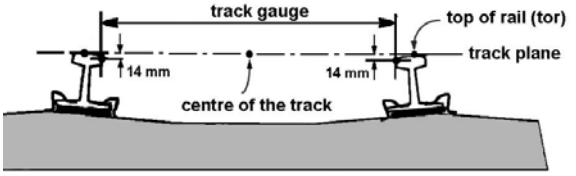

Figure 2 Measurement method of track gauge [10].

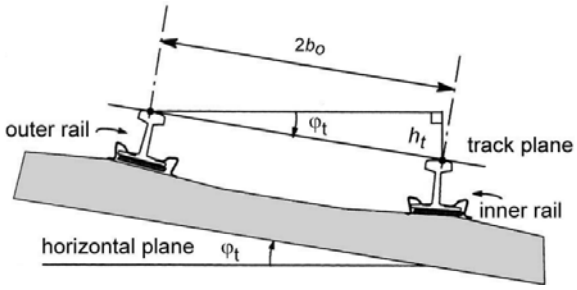

Figure 3 Measurement method of cross level [10].

3. The gauge (Gauge) of the model railway, which has a width between the rails of 459 millimeters, involves a measurement method for railway gauges. A gauge measuring device has been designed, consisting of a linear guide roller assembly that allows the rollers to move in one direction. A spring generates pressure to ensure that the rollers are always fully extended. On the sides of the roller assembly, there are mounts for the encoder's cable, as shown in Figure 4. This assembly is installed on both the left and right sides, with a spacing of 430 millimeters (the minimum

DOI: 10.60101/jarst.2024.260837

distance between the left and right gauge measuring devices) plus the extension distance of the gauge measuring devices on both sides, as shown in Figure 5.

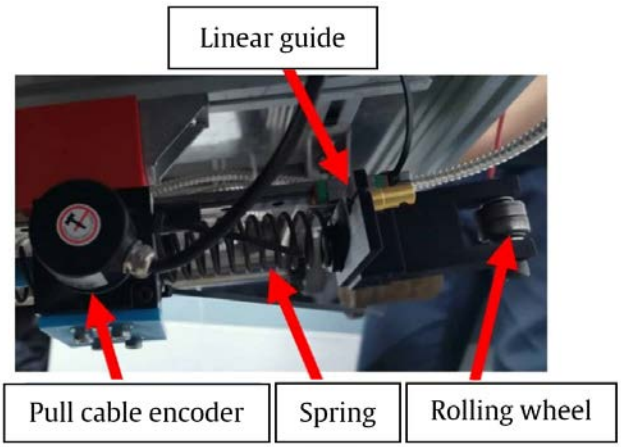

Figure 4 Railway Gauge Measuring Device.

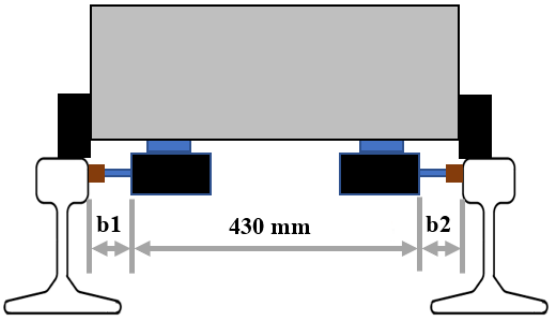

Figure 5 Measurement Method for Gauge of the Railway Geometry Inspection Vehicle.

$$b = (b_1 + b_2) + 430 \quad (1)$$

When
b is the width of the railway,
b_1 is the value measured by the encoder on the left,
b_2 is the value measured by the encoder on the right,
430 is the constant representing the minimum distance between the left and right gauge measurement tools.

To measure the width of the railway, it is essential for the measuring tool to be perpendicular to the rails. Therefore, guide rails are required both at the front and rear of the vehicle. These guide rails are equipped with springs that generate a pushing force to keep the other side of the vehicle close to the rails while measuring the irregularities of the railway. This is illustrated in Figure 6.

Cross level refers to the difference in height between the running surface adjacent to the rail, calculated from the angle between the running surface and a horizontal reference plane, as shown in Figure 7.

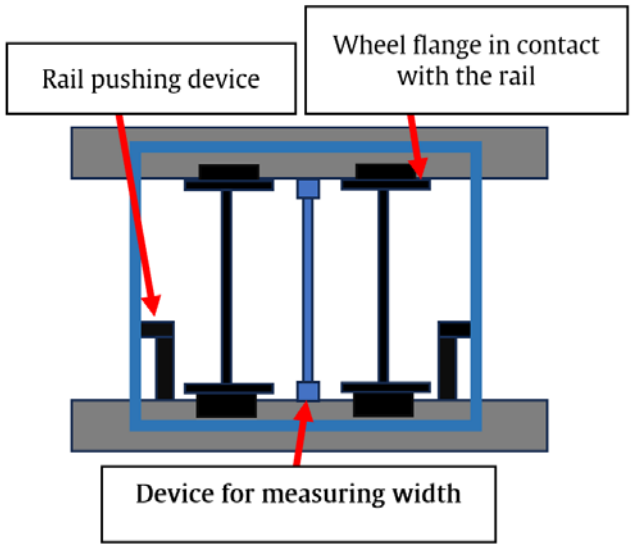

Figure 6 Equipment under the geometric irregularity measurement vehicle for the railway.

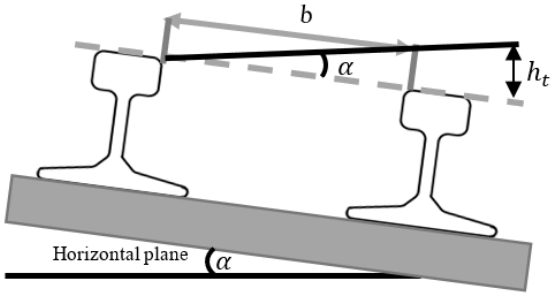

Figure 7 The cross level of the railway.

Considering the law of sines to calculate the cross-level value, we can derive the following equation 12.

$$h_t = b \cdot \sin(\alpha) \quad (2)$$

When
h_t is the cross-level height of the railway.
α is the tilt angle of the vehicle caused by the different elevations of the rails as measured by the width sensor of the inertial measurement unit.

4. The design of the control and data collection system.

The geometric irregularity measurement vehicle can support a weight of up to 80 kilograms for the operator. It is controlled to move forward or backward using a joystick, with a movement speed of 0.5 meters per second. The vehicle is equipped with the capability to measure the rail gauge of 459 millimeters and the inclination of the railway.

4.1 The drive system, as shown in Figure 8, consists of a joystick (1.2) that inputs signals to a computer (3). The computer converts these signals into speed commands sent to the NI myRIO (2). When the start button on the joystick is pressed, pushing

DOI: 10.60101/jarst.2024.260837

the lever forward moves the vehicle forward, while pulling the lever back causes the vehicle to reverse. An encoder (1.1) is attached to a rubber wheel positioned on the railhead. As the vehicle moves, the encoder generates electrical signals from its rotation, which are sent to the NI myRIO. The data is then transmitted to the computer to record the distance traveled.

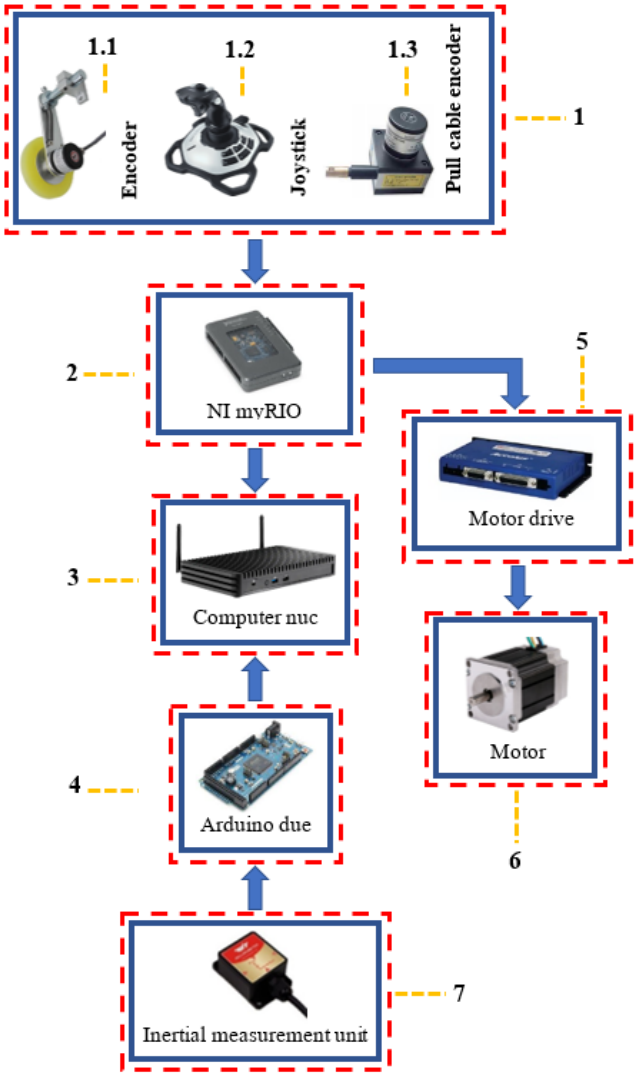

Figure 8 Details of the Equipment for the Geometric Irregularity Inspection Vehicle.

4.2 Data Collection is divided into three parts 1. Track Gauge Measurement. The track gauge is measured using the gauge measurement tool designed as shown in Figure 5. The equipment shown in Figure 8 includes a pull cable encoder (1.3) that transmits electrical signals to the NI myRIO (2). The data is analyzed using equation (11) and recorded on the computer (3). 2. Cross-Level Measurement. Cross-level measurement is performed using an Inertial Measurement Unit (IMU) (7), which detects the angles resulting from tilting across the transverse axis. These angle measurements, combined with the track gauge, are used to calculate cross-level values using equation (12) and then recorded on the computer. 3. Distance Measurement. The distance traveled during the inspection is measured using the encoder (1.1). It detects the movement of the vehicle, sends signals to the NI myRIO for analysis, converts the signals into distance data, and records the results on the computer.

5. Design of the measurement system.

Calibration of the Measurement System is divided into two parts. 1. Calibration of the Pull Cable Encoder Distance. The pull cable encoder is calibrated to ensure its measurements align with actual distances. This involves comparing the encoder's signal output with a known reference distance, adjusting for any discrepancies, and verifying repeatability to maintain accuracy. 2. Calibration of the Angle Measurement Device The angle measurement device, typically an Inertial Measurement Unit (IMU), is calibrated by comparing its angle readings with a precise reference standard. This process ensures that the IMU accurately detects and reports tilt angles, which are critical for cross-level calculations. Adjustments are made as necessary to align the device's output with the standard.

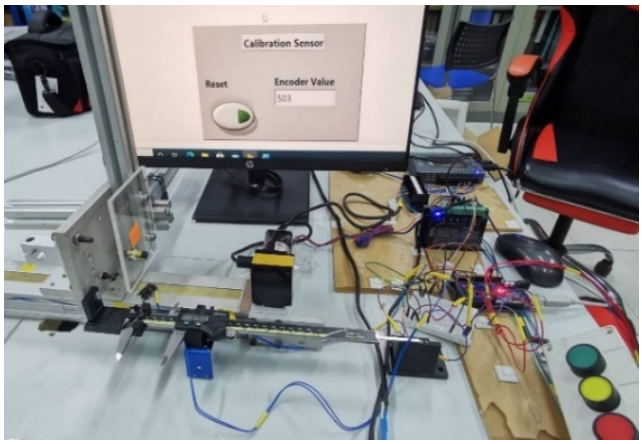

Figure 9 Testing the distance measurement of the pull cable encoder.

Table 1 Calibration results of the Pull Cable Encoder.

Actual compression distance. (mm)	The values measured by the pull cable encoder. (pulse)			
	Test 1	Test 2	Test 3	Average value
3	120	120	120	120
6	244	240	237	240
9	356	360	357	358
12	472	476	486	478
15	596	604	591	597

5.1 Calibration of the Pull Cable Encoder involves testing the accuracy of the pull cable encoder's distance measurement. The test is conducted to record

DOI: 10.60101/jarst.2024.260837

the precision of the pull cable encoder compared to a vernier caliper with an accuracy of ±0.01 millimeters, as illustrated in Figure 9, with the results presented in Table 1.

Based on Table 2, the calibration values for the Pull Cable Encoder indicate that the readings from the encoder have discrepancies from the actual collapse distance. Therefore, the obtained values are plotted on a graph, resulting in a linear equation as shown in Figure 10. This equation consists of the slope of the graph multiplied by the readings and added to a constant. The resulting linear equation is written as a function in the LabVIEW program, and the accuracy of the encoder is tested as shown in Table 2, revealing an average discrepancy of 0.05 millimeters.

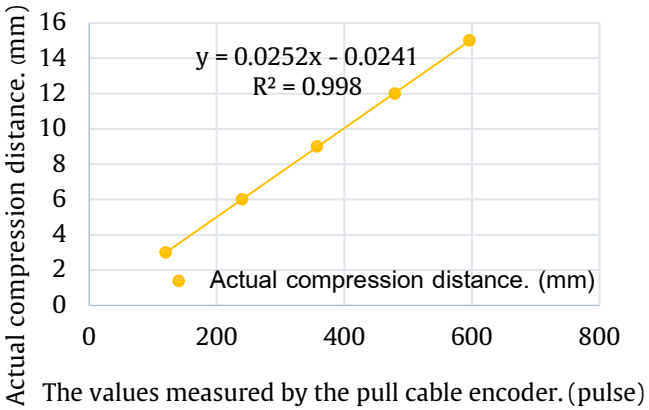

Figure 10 Calibration of the Pull Cable Encoder.

Table 2 Testing of Actual Collapse Distance Compared to Collapse Distance from Compensation Equation.

Vernier (mm)	Encoder value (mm)	Error value (mm)
4.87	4.83	0.04
7.39	7.34	0.05
9.86	9.83	0.03
12.37	12.34	0.03
14.9	14.85	0.05
17.4	17.34	0.06
19.92	19.84	0.08
22.42	22.35	0.07
24.87	24.92	0.05
Average Value		**0.05**

Plot the values from Table 1 in a graph, as shown in Figure 10.

Based on Table 2, the calibration values for the Pull Cable Encoder indicate that the readings from the encoder have discrepancies from the actual collapse distance. Therefore, the obtained values are plotted on a graph, resulting in a linear equation as shown in Figure 10. This equation consists of the slope of the graph multiplied by the readings and added to a constant. The resulting linear equation is written as a function in the LabVIEW program, and the accuracy of the encoder is tested as shown in Table 2, revealing an average discrepancy of 0.05 millimeters.

5.2 Calibration of the angle measurement instrument involves testing the accuracy of the tilt measurement. This process assesses the precision of the Inertial Measurement Unit (IMU) against a dual-axis digital angle protractor, which has an accuracy of ±0.01 degrees, as shown in Figure 11. The obtained values are presented in Table 3.

Plot the values from Table 3 to obtain the graph shown in Figure 12.

From Table 4, the calibration values of the Inertial Measurement Unit (IMU) indicate that the readings from the IMU have discrepancies compared to the actual incline. Therefore, the obtained values are plotted on a graph, as shown in Figure 12. A linear equation is derived, which consists of the slope of the graph multiplied by the recorded values, plus a constant. This linear equation is then implemented as a function in LabVIEW to test the accuracy of the IMU. It is observed that the average error is 0.01 degrees.

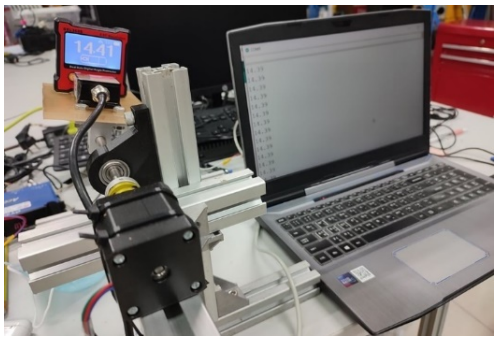

Figure 11 The calibration of the angle measurement instrument.

Table 3 presents the test results for measuring angles using the Inertial Measurement Unit (IMU).

Angle of Angle Gauges (degrees)	Angle of IMU (degrees)	Error value (degrees)
5.27	4.71	-0.56
3.08	2.5	-0.58
1.63	0.81	-0.82
-0.35	-1.24	-0.89
-2.19	-3.21	-1.02
-4.1	-5.19	-1.09
-6.06	-7.27	-1.21

DOI: 10.60101/jarst.2024.260837

JOURNAL OF APPLIED RESEARCH ON SCIENCE AND TECHNOLOGY

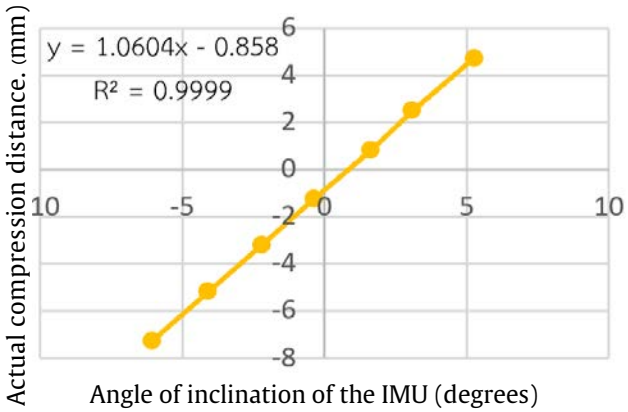

Figure 12 Calibration of the Inertial Measurement Unit (IMU).

Table 4 Testing Actual Incline Compared to Incline Distance from the Equation.

Angle of angle gauges (degrees)	Angle of IMU (degrees)	Error value (degrees)
10.5	10.51	0.01
8.31	8.30	0.01
6.3	6.29	0.01
0.11	0.10	0.01
-6.22	-6.20	0.02
-10.12	-10.13	0.01
-12.06	-12.05	0.01
Average Value		**0.01**

RESULTS AND DISCUSSION

In the testing of the geometric irregularity measurement vehicle, the vehicle is maneuvered to run on a straight track of 10 meters. The measurement vehicle will move at three different speeds: 0.1, 0.3, and 0.5 meters per second. Measurements of width, incline, and cross-level height of the railway will be taken every 0.5 meters. The tester has a mass of 70 kilograms, as shown in Figure 13.

The testing of width and cross-level height measurements of the railway over a distance of 10 meters, conducted at speeds of 0.1, 0.3, and 0.5 meters per second with a weight of approximately 70 kilograms, is compared with calibrated measuring instruments from a laboratory accredited under ISO/IEC 17025 standards, as shown in Figure 14.

Figure 13 The testing of measurements for the width, incline, and cross-level height of the railway.

Figure 14 The measuring instruments used to compare the measurements of gauge width and angle of inclination.

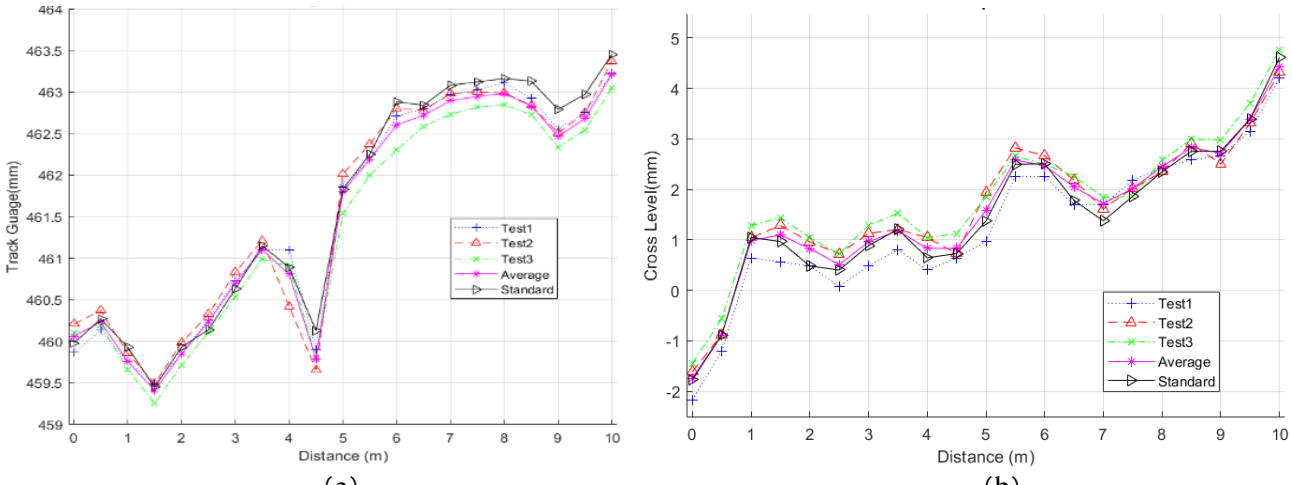

(a) (b)

Figure 15 The measurement of railway irregularities at a speed of 0.1 meters per second (a) the width measurement and (b) the height differential of the railway track.

DOI: 10.60101/jarst.2024.260837

JOURNAL OF APPLIED RESEARCH ON SCIENCE AND TECHNOLOGY

The testing of width and cross-level height measurements of the railway over a distance of 10 meters, conducted at speeds of 0.1, 0.3, and 0.5 meters per second with a weight of approximately 70 kilograms, is compared with calibrated measuring instruments from a laboratory accredited under ISO/IEC 17025 standards, as shown in Figure 14.

The experiment on measuring the geometric irregularities of railway tracks was conducted using measuring instruments (Figure 14). At a speed of 0.1 meters per second, the measurements showed that the width had a maximum error of 0.58 millimeters, a minimum error of 0.01 millimeters, and an average error of 0.11 millimeters, as illustrated in Figure 15(a). The height differential of the railway track recorded a maximum error of 0.56 millimeters, a minimum error of 0.01 millimeters, and an average error of 0.12 millimeters, shown in Figure 15(b).

When the measurement speed was increased to 0.3 meters per second, the width had a maximum error of 0.55 millimeters, a minimum error of 0.01 millimeters, and an average error of 0.12 millimeters, as seen in Figure 16(c). The height differential recorded a maximum error of 0.56 millimeters, a minimum error of 0.01 millimeters, and an average error of 0.56 millimeters, shown in Figure 16(d). Further increasing the measurement speed to 0.5 meters per second resulted in the width having a maximum error of 0.63 millimeters, a minimum error of 0.015 millimeters, and an average error of 0.13 millimeters, as depicted in Figure 16(e). The height differential had a maximum error of 0.18 millimeters, a minimum error of 0.02 millimeters, and an average error of 0.58 millimeters, shown in Figure 17(f). Finally, a comparison of the error levels was made.

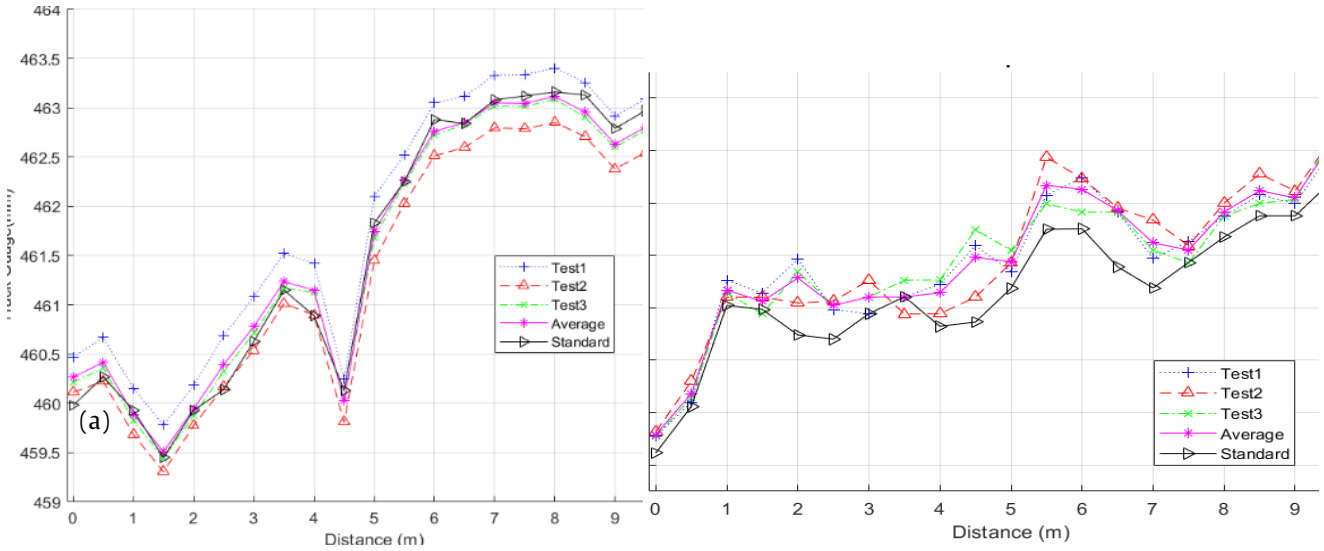

Figure 16 Illustrates the measurement of railway irregularities at a speed of 0.3 meters per second (a) track width and (b) track cross-level differential.

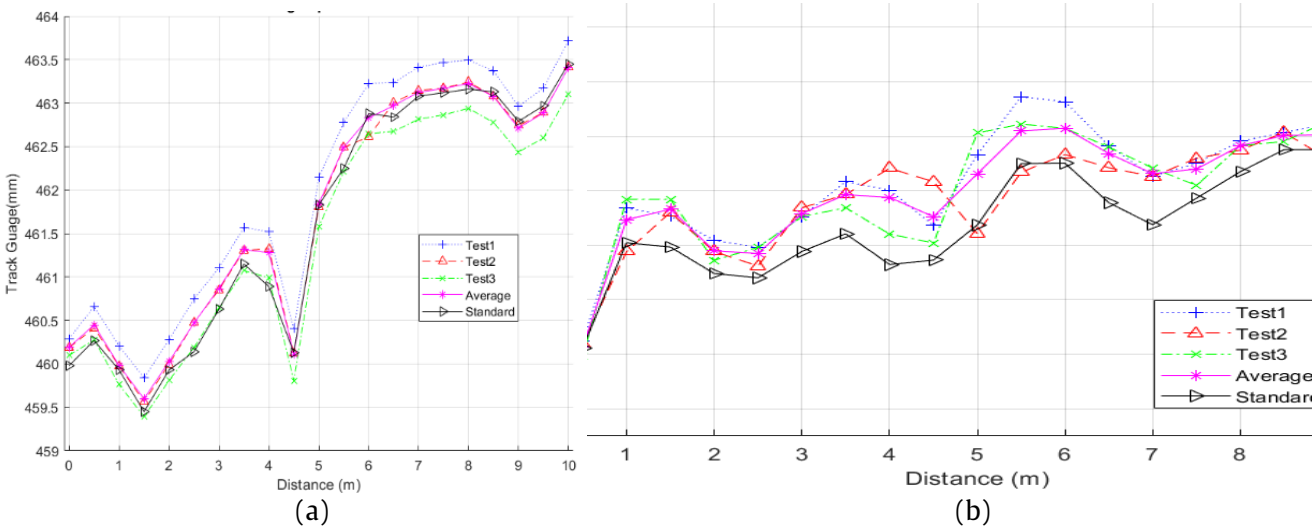

Figure 17 Illustrates the measurement of railway irregularities at a speed of 0.5 meters per second (a) track width and (b) track cross-level differential.

DOI: 10.60101/jarst.2024.260837

JOURNAL OF APPLIED RESEARCH ON SCIENCE AND TECHNOLOGY

For the comparison of the mean error levels in measuring railway track width and cross-level irregularities using Analysis of Variance (ANOVA) [11], it was found that track width measurement at speeds of 0.1 ($\bar{X}$ = 0.15), 0.3 ($\bar{X}$ = 0.12), and 0.5 ($\bar{X}$ = 0.13) meters per second, the data variability (F = 0.81) was low. The statistical probability (p-value = 0.45), being higher than the threshold of 0.05, indicates no statistically significant difference, as shown in Table 5. Cross-Level Measurement at speeds of 0.1 ($\bar{X}$ = 0.12), 0.3 ($\bar{X}$ = 0.56), and 0.5 ($\bar{X}$ = 0.55) meters per second, the data variability (F = 18.62) was high. The statistical probability (p-value = 0.00), being lower than the threshold of 0.05, indicates a statistically significant difference at the 0.05 level, as shown in Table 6.

When comparing the mean differences between two groups using Fisher's Least Significant Difference (LSD) method [12], it was found that the average error in cross-level measurement at a speed of 0.1 meters per second was significantly lower than the errors at speeds of 0.3 meters per second and 0.5 meters per second, as presented in Table 7.

Table 5 Comparison of Mean Error Levels in Railway Track Width Measurement by Speed Using Analysis of Variance (ANOVA) [11].

Factor	Compare differences					
	Speed	$\bar{X}$	S.D.	F	df	p-value
Mean error of railway track width measurement	0.1 m/s	0.15	0.11	0.81	60	0.45
	0.3 m/s	0.12	0.08			
	0.5 m/s	0.13	0.11			

Table 6 Comparison of differences in average cross-level height measurement error of the railway track categorized by speed using Analysis of Variance (ANOVA) [11].

Factor	Compare differences					
	Speed	$\bar{X}$	S.D.	F	df	p-value
Average error values in measuring the cross-level height of the railway track.	0.1 m/s	0.12	0.10	18.62	60	0.00*
	0.3 m/s	0.56	0.33			
	0.5 m/s	0.55	0.31			

*Statistically significant at the 0.05 level.

Table 7 Differences in the average error levels of railway elevation measurements classified by speed, obtained from testing using Fisher's least significant difference (LSD) method [12].

Speed	Mean Difference (I-J) refers to the difference in the average values between two groups (Group I and Group J).			
	Mean	0.1 m/s	0.3 m/s	0.5 m/s
0.1 m/s	0.12	-	-.44*	-.43*
0.3 m/s	0.56		-	.01
0.5 m/s	0.55			-

*Statistically significant at the 0.05 level.

CONCLUSIONS

This research has designed and developed a prototype vehicle for measuring geometric abnormalities, which can be further developed for use on railway tracks of 1 meter and 1.435 meters. These two sizes of tracks are commonly used in Thailand. An important aspect of the vehicle for measuring geometric abnormalities is the measuring instruments, including a width measurement tool and an angle measurement tool, which are designed to be easily attached to railway cars or inspection vehicles. The aim of this design is to ensure convenience in assembly, disassembly, and usage.

From the research findings, it can be concluded that the results of tests conducted at different speeds show that the measured width of the railway tracks using the measuring tools do not differ significantly. However, the measured height differences of the railway tracks using the measuring tools show a statistically significant difference at the level of 0.05, with values of 0.14 millimeters and 0.17 millimeters.

DOI: 10.60101/jarst.2024.260837

Considering the observed discrepancies, both tests can serve as a prototype for creating measurement tools for practical use.

ACKNOWLEDGEMENT

This research was Supported by The Science, Research and Innovation Promotion Fund (TSRI) (Grant no.FRB640013). This research block grants was managed under Rajamangala University of Technology Thanyaburi (FR645E0703C.4.)

REFERENCES

1. Inthara A, Rojanapunya P, Saiseng N. Thailand's railroad development and future high speed train development. Journal of Yala Rajabhat University. 2017;12(Special Issue):151-67.
2. State Railway of Thailand. Complete guide to SRT 4.0. Bangkok: State Railway of Thailand; 2019.
3. Bangkok Mass Transit System Public Company Limited. The BTS SkyTrain system [Internet]. 2022. [cited 2022 Apr 11]. Available from: https://www.bts.co.th/library/system-structuer.html.
4. Office of Transport and Traffic Policy and Planning. Railway structure maintenance manual. Bangkok: Office of Transport and Traffic Policy and Planning; 2018.
5. Bumrungkij A, Yamfang M, Janthong M. Development of a mobile measurement device prototype for parallelity measurement of rails. KMUTT Research and Development Journal. 2021;44(3):501-13.
6. Chen Q, Niu X, Zhang Q, Cheng Y. Railway Track Irregularity Measuring by GNSS/INS Integration: Chen et al.: Railway Track Irregularity by GNSS/INS. Navigation (Wash) [Internet]. 2015;62(1):83–93. Available from: http://dx.doi.org/10.1002/navi.78.
7. Odziemczyk W, Woźniak M. Analysis of railway track geometry measurement methods usability. Transportation Overview - Przeglad Komunikacyjny [Internet]. 2018;2018(8):40–50. Available from: http://dx.doi.org/10.35117/a_eng_18_08_05.
8. Chen W, Li D, Liu Y, Zhu Z, Huang Z, Yan J. Development and application of a multi-sensor integration detection and analysis device for metro gauge and track geometric state. AIP Adv [Internet]. 2021;11(6):065033. Available from: http://dx.doi.org/10.1063/5.0053474.
9. Escalona JL, Urda P, Muñoz S. A Track Geometry Measuring System based on multibody kinematics, inertial sensors and computer vision. Sensors (Basel) [Internet]. 2021;21(3):683. Available from: http://dx.doi.org/10.3390/s21030683.
10. Lindahl M. Track geometry for high speed railways: A literature survey & simulation of dynamic vehicle response, TRAIT-FKT Report 2001:54, ISSN 1103-470X.
11. Lomax RG, Hahs-Vaughm DL. Statistical concept a second course. 4 ed. United States of America: Taylo & Francis Group; 2012
12. Abdi H. The method of least squares [Internet]. 2010 [cited 2025 Mar 7]. Available from: https://personal.utdallas.edu/~herve/abdi-LSD2010-pretty.pdf.

DOI: 10.60101/jarst.2024.260837

Institute of Research and Development
Rajamangala University of Technology Thanyaburi

39 M.1 Klong 6, Thanyaburi, Pathumthani 12110, Thailand
Tel. (02) 549-4492 Fax. (02) 577-5038, (02) 549-4680

Website : https://ird.rmutt.ac.th